

University of Strathclyde
Department of Mechanical & Aerospace Engineering

**Computational investigation of
immersion quenching:
understanding of boiling conjugate heat
transfer**

Robin Kamenický

A thesis presented in fulfilment of the requirements
for the degree of Doctor of Philosophy

2021

Declaration of author's rights

This thesis is the result of the author's original research. It has been composed by the author and has not been previously submitted for examination which has led to the award of a degree.

The copyright of this thesis belongs to the author under the terms of the United Kingdom Copyright Acts as qualified by University of Strathclyde Regulation 3.50. Due acknowledgement must always be made of the use of any material contained in, or derived from, this thesis.

Robin Kamenický

December 2021

Abstract

Quenching is a metallurgical procedure used to alter material properties of metals and alloys. Although used extensively throughout human history, its design relies heavily on experience and often the trial and error method. Therefore, the availability of computational tools capable of describing the physics during quenching would help design facilities efficiently, lower costs, and even make the process more environmentally friendly.

This work aims to develop and validate a numerical procedure for immersion quenching using computational fluid dynamics. The methodology employs the partitioned approach. An energy equation and Eulerian two-fluid model describe the solid and fluid region, respectively. The heat transfer information is exchanged at the regions' interface.

In this thesis, various aspects of the methodology are discussed. Yet, the primary attention is given to the wall boiling and the conjugate heat transfer, which are crucial. Furthermore, during an attempt to formulate stability criteria, the numerical Biot number has been developed as a potential candidate accounting for all three phases, solid, liquid and vapour.

The code validation is split into three chapters. The first investigates conjugate heat transfer without boiling in a backward-facing step geometry. The next is concentrated on a hot thin horizontal plate submerged in water, and the last describes the quenching system behaviour during immersion quenching of a cylinder in a vertical orientation.

The numerical results proved excellent accuracy for conjugate heat transfer problem without boiling. A good agreement with validation data is also achieved when boiling occurs, yet complications are observed at locations where vapour movement is obstructed. Vapour volume fraction tends to be mesh sensitive, affecting the solid

temperature field in its proximity. Such behaviour can be often prevented using phase change within the inner fluid mesh. However, doing so, the user limits the solver capabilities as vapour obstruction is often desirable.

Acknowledgements

During my research at the University of Strathclyde, I was honoured to meet many exceptional people whom I am grateful for sharing their time, friendship, knowledge and wisdom with me. Now, I would like to take the opportunity to express my gratitude to a few of them.

First of all, I want to thank my supervisor Dr Konstantinos Ritos for his guidance, patience and positive attitude. I sincerely appreciate your eagerness to help and support in the moments of struggle. Our cooperation has always been fruitful and refreshing resulting in new ideas enriching the research project.

I am deeply grateful to Prof Dimitris Drikakis for making this research project possible, sharing his experience, mentoring and time. Thank you for providing me with the opportunity of being part of your team.

I would like to extend my sincere thanks to Dr Michael Frank for his insightful comments, suggestions and patience. Thank you for being my C++ mentor and cooperating on the separator project.

Special thanks also go to Dr Salaheddin Rahimi, Dr Ioannis Violatos, Dr Sebastien Nouveau and the Advanced Forming Research Centre for providing valuable insides and experimental data.

I thank Dr Ioannis Kokkinakis for his time, help and advice.

I also thank the Mechanical and Aerospace Engineering Department for all the support provided during the project.

I thank Deep Sanjay Bandivadekar, my fellow PhD student and friend, who I could share with my OpenFOAM experience. We have always had a great time together, full of exciting conversations and joy.

I further thank my friend Dr Mateusz Polnik for his advice, support, and time

together.

I thank my friends Audrey Berquand, Kevin Singh and Francesco Murdaca for sharing their journey with me and making it joyful.

Last but by no means least, I would like to express my heartfelt gratitude to my partner Liubov Subbotina, who agreed to move with me to the UK and continues to be my primary support and source of strength and love. Together with her, I want to thank my parents and grandma, who have always loved me, supported me in life and education, and I could rely on them. I dedicate this thesis to them.

Contents

Abstract	ii
Acknowledgements	iv
Contents	vi
List of figures	ix
List of tables	xvii
Nomenclature	xix
1 Introduction	1
1.1 Motivation	1
1.2 Project objectives	2
1.3 Thesis outline	3
1.4 Immersion quenching	4
1.4.1 Metalurgical view	4
1.4.2 Heat transfer	6
1.4.3 Factors affecting quenching	10
1.4.4 State of the art computational approaches	14
1.5 Key developments	16
1.6 Publications and Conferences	18
2 Methodology	19
2.1 Governing equations	20

2.1.1	Fluid region	20
2.1.2	Solid region	24
2.2	Interfacial terms	24
2.2.1	Momentum	26
2.2.2	Heat transfer	29
2.2.3	Interfacial phase change	30
2.3	Wall boiling	31
2.4	Solid-fluid interfacial temperature	38
2.5	Solution algorithm	41
2.6	Numerical solvers and schemes	44
2.7	ETF restriction for grid discretization	46
2.8	Summary	47
3	Backward-facing step conjugate heat transfer	48
3.1	Geometry, mesh, initial and boundary conditions	49
3.2	Validation variables and convergence criteria	52
3.3	Time and mesh convergence	54
3.4	Results, validation and discussion	62
3.5	Summary	70
4	Plate quenching	72
4.1	Experiment description and analysis	72
4.2	Geometry, mesh and boundary conditions	73
4.3	Results and discussion	76
4.4	Summary	88
5	Cylinder quenching	90
5.1	Experiment description and analysis	90
5.2	Geometry, mesh, initial and boundary conditions	98
5.3	Mesh sensitivity analysis	102
5.4	Results and discussion	113
5.5	Summary	127

6	Conclusions	129
6.1	Contributions	130
6.2	Limitations	131
6.3	Future Work	132
	References	135
	Appendices	146
A	Video of cylinder quenching experiment	146
B	Computational code and cases	147

List of figures

1.1	a) Simplified $Fe - Fe_3C$ phase diagram showing metastable equilibrium for plain steel [3]. b) Continuum Cooling Transformation diagram of SAE 1020 steel [3] <i>Au</i> - Austenite; <i>Fr</i> - Ferrite; <i>Pl</i> - Pearlite; Fe_3C - Cementite; <i>B</i> - Bainite; <i>M</i> - Martensite; <i>Eu</i> - Eutectoid; Subscripts <i>St</i> and <i>Fi</i> stand for Start and Finish of transformation.	5
1.2	A qualitative boiling curve showing heating, cooling and influence of controlled variable. Heat transfer regimes: FB - Film boiling, TB - Transition boiling, FDNB - Fully developed nucleate boiling, PDNB - Partially developed nucleate boiling, NCV - Natural convection. The various subscripts: SAT - Saturation, ONB - Onset of nucleate boiling, FDB - Fully developed boiling, LEID - Leidenfrost, DNB - Departure from nucleate boiling, CHF - Critical heat flux, MHF - Minimum heat flux. Subscript <i>w</i> stands for heated wall.	7
1.3	A qualitative boiling curve shows sudden temperature drop appearing during the transition from convective HTR to nucleate boiling HTR at heating conditions. Also, hysteresis is visualised during transition boiling, arising when the heated surface temperature is controlled and the process is transient.	10
1.4	Cooling curves of various quenchants, including oils, water and brine [3]	13
1.5	Cooling curves of various quenchants, including polymers at different concentrations with and without agitation [3]. The coolants temperature is between $38\text{ }^\circ\text{C}$ and $49\text{ }^\circ\text{C}$	14

2.1	25
2.2	Heat transfer regimes. FB - Film boiling, TB - Transition boiling, NB - Nucleate boiling, CV - convective heat transfer. The various subscripts meanings follow: LEID - Leidenfrost, DNB - departure from nucleate boiling, SAT - saturation, MHF - minimum heat flux, CHF - critical heat flux	31
2.3	a) Interface mesh view; b) Partitioned heat transfer into liquid and vapour; c) Heat transfer into fluid. R represents thermal insulance and is defined by Eq. (2.82)	39
2.4	Solution algorithm	42
3.1	Computational domain with dimensions, boundary conditions names and vortices locations.	50
3.2	Velocity streamlines visualising vortices in the fluid region at 500 s . The domain is not shown in full length. Computational mesh with element sizes a) 50.00 mm , b) 25.00 mm , c) 12.50 mm and d) 6.25 mm , respectively. Bottom left corner for computational mesh with element sizes e) 50.00 mm , f) 25.00 mm , g) 12.50 mm and h) 6.25 mm , respectively. . .	55
3.3	Velocity profiles of the a) streamwise and b) normal components at $x/b = 14$ and 500 s using various meshes.	56
3.4	Velocity profiles of the a) streamwise and b) normal components at $x/b = 30$ and 500 s using various meshes.	56
3.5	Velocity profiles of the a) streamwise and b) normal components at $x/b = 14$ at various times using the computational mesh with element size 12.50 mm	57
3.6	Velocity profiles of the a) streamwise and b) normal components at $x/b = 30$ at various times using the computational mesh with element size 12.50 mm	57
3.7	Non-dimensional temperature contours for various computational meshes at 1500 s and conductivity ratio $\kappa_{ra} = 1$. a) Computational mesh with element size 50.00 mm ; b) Computational mesh with element size 25.00 mm ; c) Computational mesh with element size 12.50 mm	59

3.8	Non-dimensionalised temperature profiles for various computational meshes at 1500 <i>s</i> and conductivity ratio $\kappa_{ra} = 1$. a) $x/b = 6$; b) $x/b = 14$; c) $x/b = 30$	60
3.9	Non-dimensionalised temperature profiles at $x/b = 6$ at various times using computational mesh with element size 12.50 <i>m</i> . a) $\kappa_{ra} = 1$; b) $\kappa_{ra} = 1000$	61
3.10	Non-dimensionalised temperature profiles at $x/b = 14$ at various times using computational mesh with element size 12.50 <i>m</i> . a) $\kappa_{ra} = 1$; b) $\kappa_{ra} = 1000$	61
3.11	Non-dimensionalised temperature profiles at $x/b = 30$ at various times using computational mesh with element size 12.50 <i>m</i> . a) $\kappa_{ra} = 1$; b) $\kappa_{ra} = 1000$	62
3.12	Comparison of non-dimensional temperature and Nusselt number profiles at the regions' interface with Ramšak VR [77] for $\kappa_{ra} = 1$ at 2500 <i>s</i> using a computational mesh with element size 25.00 <i>mm</i> . a) Non-dimensionalised temperature; b) Nusselt number	66
3.13	Comparison of non-dimensional temperature and Nusselt number profiles at the regions' interface with Ramšak VR [77] for $\kappa_{ra} = 10$ at 2000 <i>s</i> using a computational mesh with element size 25.00 <i>mm</i> . a) Non-dimensionalised temperature; b) Nusselt number	66
3.14	Comparison of non-dimensional temperature and Nusselt number profiles at the regions' interface with Ramšak VR [77] for $\kappa_{ra} = 100$ at 1500 <i>s</i> using a computational mesh with element size 25.00 <i>mm</i> . a) Non-dimensionalised temperature; b) Nusselt number	67
3.15	Comparison of non-dimensional temperature and Nusselt number profiles at the regions' interface with Ramšak VR [77] for $\kappa_{ra} = 1000$ at 1500 <i>s</i> using a computational mesh with element size 25.00 <i>mm</i> . a) Non-dimensionalised temperature; b) Nusselt number	67

3.16	Non-dimensional temperature contours for various conductivity ratios and times, acquired using the mesh with element size 25.00 mm. a) $\kappa_{ra} = 1$ at 2500 s; b) $\kappa_{ra} = 10$ at 2000 s; c) $\kappa_{ra} = 100$ at 1500 s; d) $\kappa_{ra} = 1000$ at 1500 s.	69
4.1	a) Numerical and experimental cooling curves obtained at the flat plate centre provided by [36]. b) Quenched specimen dimensions and thermocouple location (orange dot).	73
4.2	Computational domain with dimensions, boundary conditions names and investigated locations on the sample marked using orange dots. L1 - Above the plate centre at the solid-fluid interface; L2 - Plate centre; L3 - Beneath the plate centre at the solid-fluid interface.	74
4.3	Cooling curves acquired at the location <i>L2</i> in the solid region using various fluid meshes. The interfacial phase change is not activated. Numerical and experimental validation data are taken from Khalloufi et al. [36]. a) Global view with validation data; b) Focused view to a time range 17-19.8 s omitting results for $x_n = 15; 5; 0.375; 0.1875$, and the experimental results.	77
4.4	Vapour volume fraction using various fluid meshes. The interfacial phase change is not activated. a) Location <i>L1</i> ; b) Location <i>L3</i>	78
4.5	Vapour volume fraction and HTRs at the plate bottom for mesh $x_n = 3.1$ mm at 18.2s. The interfacial phase change is not activated.	80
4.6	Fluid Biot number according to Eq. (2.86) using various fluid meshes. The interfacial phase change is not activated. a) Location <i>L1</i> ; b) Location <i>L3</i> ; c) Location <i>L3</i> focused on $x_n \geq 1.5$ mm.	81
4.7	Fluid temperature in the boundary cell according to Eq. (2.85) at the location <i>L3</i> using various fluid meshes. a) IPC is not activated; b) IPC is activated.	82
4.8	Cooling curves acquired at the location <i>L2</i> using various fluid meshes. The interfacial phase change is allowed. Numerical and experimental validation data are taken from Khalloufi et al. [36].	82

4.9	Fluid Biot number according to Eq. (2.86) at the location $L3$ using various fluid meshes. The interfacial phase change is allowed. a) Global view b) Focused view on $x_n \geq 1.5 \text{ mm}$	83
4.10	Maximum of liquid-vapour interfacial temperature according to Eq. (2.5) from boundary cells centres using various fluid meshes. a) IPC is not activated; b) IPC is activated.	84
4.11	Spatial and time distribution of vapour volume fraction and solid temperature fields during the horizontally oriented plate quenching.	85
4.12	Spatial and time distribution of total velocity u_{tot} (Eq. 2.15) streamlines coloured by its magnitude and horizontally oriented plate temperature fields.	87
5.1	Photo of the quenched cylinder with two holders and thermocouples locations used for validation and data collection.	91
5.2	Photos from the cylinder quenching experiment with approximate time related to the thermocouples measurements (Fig. 5.3).	93
5.3	Experimental data acquired at various locations within the quenched cylindrical specimen (Table 5.1). a) Cooling curves up to 200 s; b) Cooling curves up to 60 s; c) Cooling rates up to 60 s.	94
5.4	Vapour developed at the top of the cylinder after immersion.	95
5.5	Schematic cylinder cross-section after the lift.	96
5.6	Analysis of heat transfer experimental results acquired at locations $J1$ and $J8$. a) Cooling curves at the period 0 to 100 s; b) Cooling rates at the period 0 to 100 s; c) Cooling curves at the period 0 to 33 s; d) Cooling rates at the period 0 to 33 s. <i>Fr.</i> - Furnace; <i>Op.</i> - Furnace opening and forklift positioning; <i>Tr.</i> - Specimen transport; <i>Im.</i> - Specimen immersion; <i>CHF</i> - Critical Heat Flux; <i>MHF</i> - Minimum Heat Flux. . .	97
5.7	Computational domain with dimensions and boundary conditions names.	99
5.8	Visualisation of the cylinder computational domain combining meshes with 31,140 fluid and 10,440 solid elements. Pictures are truncated and not in scale. a) Side view b) Top view.	101

5.9	Fluid mesh sensitivity study at various locations using solid mesh with 58,800 elements. Visualisation of temperature at a) <i>J1</i> , b) <i>J4</i> , c) <i>J8</i> and cooling rate at d) <i>J1</i> , e) <i>J4</i> , f) <i>J8</i>	104
5.10	Fluid mesh sensitivity study at various locations using solid mesh with 58,800 elements. Visualisation of vapour volume fraction at a) <i>J1</i> , b) <i>J4</i> , c) <i>J8</i> and fluid Biot number at d) <i>J1</i> , e) <i>J4</i> , f) <i>J8</i>	105
5.11	Solid mesh sensitivity study at various locations using fluid mesh with 31,140 elements. Visualisation of temperature at a) <i>J1</i> , b) <i>J4</i> , c) <i>J8</i> and cooling rate at d) <i>J1</i> , e) <i>J4</i> , f) <i>J8</i>	107
5.12	Solid mesh sensitivity study at various locations using fluid mesh with 31,140 elements. Visualisation of vapour volume fraction at a) <i>J1</i> , b) <i>J4</i> , c) <i>J8</i> and fluid Biot number at d) <i>J1</i> , e) <i>J4</i> , f) <i>J8</i>	108
5.13	Solid mesh sensitivity study at various locations using fluid mesh with 59,008 elements. Visualisation of temperature at a) <i>J1</i> , b) <i>J4</i> , c) <i>J8</i> and cooling rate at d) <i>J1</i> , e) <i>J4</i> , f) <i>J8</i>	109
5.14	Investigation of IPC effect using the solid mesh with 451,500 elements combined with fluid meshes of 31,140 and 59,008 elements. Visualisation of temperature at a) <i>J1</i> , b) <i>J4</i> , c) <i>J8</i> and cooling rate at d) <i>J1</i> , e) <i>J4</i> , f) <i>J8</i>	111
5.15	Investigation of IPC effect using the solid mesh with 451,500 elements combined with fluid meshes of 31,140 and 59,008 elements. Visualisation of vapour volume fraction at a) <i>J1</i> , b) <i>J4</i> , c) <i>J8</i> and fluid Biot number at d) <i>J1</i> , e) <i>J4</i> , f) <i>J8</i>	112
5.16	Comparison of experimental and numerical results acquired using meshes with 59,008 and 451,500 computational elements for fluid and solid, respectively. The cooling curves at the initial 200 <i>s</i> are visualised at locations a) <i>J1</i> , b) <i>J3</i> , c) <i>J4</i> , d) <i>J6</i> , e) <i>J8</i> , f) <i>J9</i>	115
5.17	Comparison of experimental and numerical results acquired using meshes with 59,008 and 451,500 computational elements for fluid and solid, respectively. The cooling curves at the initial 25 <i>s</i> are visualised at locations a) <i>J1</i> , b) <i>J2</i> , c) <i>J10</i>	116

5.18	Comparison of experimental and numerical results acquired using meshes with 59,008 and 451,500 computational elements for fluid and solid, respectively. The cooling rates at the initial 25 s are visualised at locations a) <i>J1</i> , b) <i>J2</i> , c) <i>J10</i>	117
5.19	Comparison of experimental and numerical results acquired using meshes with 59,008 and 451,500 computational elements for fluid and solid, respectively. The cooling rates as a function of temperature are visualised at locations a) <i>J1</i> , b) <i>J2</i> , c) <i>J10</i>	118
5.20	Comparison of experimental and numerical results acquired using meshes with 59,008 and 451,500 computational elements for fluid and solid, respectively. The cooling curves at the initial 25 s are visualised at locations a) <i>J6</i> , b) <i>J8</i> , c) <i>J7</i> , d) <i>J9</i>	119
5.21	Comparison of experimental and numerical results acquired using meshes with 59,008 and 451,500 computational elements for fluid and solid, respectively. The cooling rates as a function of time at the initial 25 s are visualised at locations a) <i>J6</i> , b) <i>J8</i> , c) <i>J7</i> , d) <i>J9</i>	120
5.22	Comparison of experimental and numerical results acquired using meshes with 59,008 and 451,500 computational elements for fluid and solid, respectively. The cooling rates as a function of temperature are visualised at locations a) <i>J6</i> , b) <i>J8</i> , c) <i>J7</i> , d) <i>J9</i>	121
5.23	Comparison of experimental and numerical results acquired using meshes with 59,008 and 451,500 computational elements for fluid and solid, respectively. The cooling curves at the initial 25 s are visualised at locations a) <i>J4</i> , b) <i>J5</i>	122
5.24	Comparison of experimental and numerical results acquired using meshes with 59,008 and 451,500 computational elements for fluid and solid, respectively. The cooling rates as a function of time at the initial 25 s are visualised at locations a) <i>J4</i> , b) <i>J5</i>	122

5.25	Comparison of experimental and numerical results acquired using meshes with 59,008 and 451,500 computational elements for fluid and solid, respectively. The cooling rates as a function of temperature are visualised at locations a) $J4$, b) $J5$	123
5.26	Spatial and time distribution of vapour volume fraction and solid temperature acquired using meshes with 59,008 and 451,500 computational elements for fluid and solid, respectively. The figures represent only a segment of the computational domain.	124
5.27	Spatial and time distribution of total velocity u_{tot} (Eq. 2.15) streamlines, coloured by its magnitude, and cylinder temperature acquired using meshes with 59,008 and 451,500 computational elements for fluid and solid, respectively. The figures represent only a segment of the computational domain.	126

List of tables

2.1	Momentum and heat transfer interfacial models.	30
2.2	Heat transfer regimes partitioning	32
2.3	Numerical solvers chosen for various variables and validation problems. .	45
2.4	Numerical schemes chosen for various terms and validation problems. Gauss theorem is used for values interpolation from cell centres to face centres.	46
3.1	Boundary conditions following the naming convention from Fig. 3.1 . . .	51
3.2	Meshes characteristics for backward-facing step problem	52
3.3	Comparison of backward-facing step vortices' detachment and reattach- ment points with Ramšak [77] using a computational mesh with element size 25.00 mm at 1500 s.	63
3.4	Comparison of interface thermodynamical variables with Ramšak [77] for $\kappa_{ra} = 1$ and mesh with element size 25.00 mm at 2500 s.	64
3.5	Comparison of interface thermodynamical variables with Ramšak [77] for $\kappa_{ra} = 10$ and mesh with element size 25.00 mm at 2000 s.	65
3.6	Comparison of interface thermodynamical variables with Ramšak [77] for $\kappa_{ra} = 100$ and mesh with element size 25.00 mm at 1500 s.	65
3.7	Comparison of interface thermodynamical variables with Ramšak [77] for $\kappa_{ra} = 1000$ and mesh with element size 25.00 mm at 1500 s.	65
4.1	Physical properties of water, vapour and the plate specimen.	74
4.2	Horizontal plate boundary conditions. $\phi_{mf,n,j}$ stands for mass flux through a boundary cell face.	75

4.3	Fluid and solid regions' meshes characteristics, mentioning the total number of elements, and boundary cells interface perpendicular dimension x_n identical at the specimen top and bottom.	76
5.1	Thermocouples locations used for validation and data collection.	91
5.2	Cylinder boundary conditions. $\phi_{mf,n,j}$ stands for mass flux through a boundary cell face.	100
5.3	Physical properties of water, vapour and the cylindrical specimen.	101
5.4	Fluid and solid regions' meshes characteristics, mentioning the total number of elements, and boundary cells interface perpendicular dimensions at the cylinder top, bottom, and side.	102

Nomenclature

Symbols

\mathbf{g}	Acceleration due to gravity vector [m/s ²]
Δx	Cell dimension in any direction [m]
\dot{m}	Mass flow rate per volume [kg/m ³ s]
$\hat{\mathbf{n}}$	Unit vector normal to a face [-]
$\hat{\mathbf{n}}_w$	Unit vector normal to a boundary [-]
$\bar{\mathbf{u}}_{in}$	Average inlet velocity [m/s]
\overline{Nu}	Average Nusselt number [-]
\bar{R}	Isentropic expansion factor for ideal gas, 8.31447 [J/(K mol)]
A	Area [m ²]
A_1	Convection heat transfer area fraction [-]
A_2	Quenching area fraction [-]
A_B	Boundary cell face area [m ²]
A_{2E}	Evaporation area fraction [-]
A_{ic}	Interfacial area concentration [m ⁻¹]
b	Backwards-facing step and inlet height [m]
Bi	Biot number [-]

C_1	Model constant for turbulence, 1.44 [-]
C_2	Model constant for turbulence, 1.92 [-]
C_3	Model constant for turbulence, 1.92 [-]
C_κ	Von Karman constant, 0.41 [-]
C_μ	Empirical model coefficient, 0.09 [-]
C_D	Drag coefficient (multiplied by Reynolds number) [-]
C_l	Lift force coefficient [-]
C_m	Model coefficient to calculate critical heat flux at saturation conditions. 0.131 [-]
C_n	Constant to calculate heat transfer coefficient during film boiling, 0.62 [-]
C_o	Model constant for nucleation site density, 1 [-]
c_p	Isobaric specific heat capacity [J/(kg K)]
C_s	Swarm coefficient, 1.0 [-]
$C_{D,Re,Elp}$	Drag coefficient for distorted particle regime [-]
$C_{D,Re}$	Drag coefficient for viscous regime or for Newton regime equal to 0.44 [-]
C_{t2}	Response coefficient [-]
C_{TD}	Turbulent dispersion force coefficient [kg/(s ² m)]
C_{VM}	Virtual mass force coefficient, 0.5 [-]
$C_{WL,1}$	Wall lubrication force coefficient, -0.01 [-]
$C_{WL,2}$	Wall lubrication force coefficient, 0.05 [-]
CFL	Courant number (Courant–Friedrichs–Lewy number) [-]

CFL_ϕ	Courant number defined using flux [-]
D	Particle diameter, bubble or droplet [m]
D_w	Bubble detachment diameter [m]
$D_{w,max}$	Minimum bubble detachment diameter, 0.0014 [m]
$D_{w,min}$	Maximum bubble detachment diameter, 1e-6 [m]
$D_{w,ref}$	Reference bubble detachment diameter, 6e-4 [m]
E	Thermal wall function model coefficient, 9.8 [-]
E_a	Aspect ratio of a particle [-]
Eu	Eötvös number [-]
Eu_H	Modified Eötvös number [-]
err	Error [%]
F	Force density [N/m ³]
f	Vapour fraction function to determine drag coefficient [-]
f_l	Polynomial function to determine lift coefficient [-]
f_w	Bubble detachment frequency [s ⁻¹]
Fo	Fourier number (Diffusion number) [-]
G	Turbulence production [m ² /s ³]
G_b	Turbulence production due to bubble presence [kg/(s ³ m)]
H	Product of interfacial area concentration and heat transfer coefficient [kg/(s ³ mK)]
h	Specific enthalpy [J/kg]
Ja	Jakob number [-]

k	Turbulent kinetic energy [m^2/s^2]
k_{burn}	Burn out coefficient, 0.5 [-]
k_{MHF}	Minimum heat flux coefficient, 5 [-]
L	Length of backward-facing step domain [m]
l	Cell characteristic dimension [m]
N	Nucleation site density [m^{-2}]
Nu	Nusselt number [-]
P	Functional Prandtl number [-]
p	Pressure [Pa]
Pe	Péclet number [-]
Pr	Prandtl number [-]
Pr_t	Turbulent Prandtl number, 0.85 [-]
q	Heat Flux [W/m^2]
q_e	Evaporation heat flux [W/m^2]
q_q	Quenching heat flux [W/m^2]
R	Thermal insulance [$\text{m}^2\text{K}/\text{W}$]
Re	Reynolds number [-]
Re_M	Modified particle Reynolds number [-]
Re_p	Particle Reynolds number [-]
Re_{BFS}	Reynolds number for backward-facing step based on average inlet velocity [-]
Sc	Schmidt number [-]

S_p	Source term [s^{-1}]
S_u	Source term [s^{-1}]
T	Temperature [$^{\circ}C$]
t	Time [s]
T^+	Dimensionless temperature at y^+ [-]
T^{+250}	Dimensionless temperature at $y^+ = 250$ [-]
T_{heat}	Temperature boundary condition value at the heater for Backward-facing Step [$^{\circ}C$]
T_{int}	Interpolated temperature using y^+ [$^{\circ}C$]
T_{in}	Temperature boundary condition value at the inlet for Backward-facing Step [$^{\circ}C$]
u	Velocity [m/s]
u_{τ}	Frictional velocity [m/s]
u_{dc}	Difference between velocity at the viscous sub-layer thickness and a boundary [m/s]
V_B	Boundary cell volume [m^3]
W	Molecular weight, 0.0180153 [kg/mol]
w	Weighting factor [-]
w_p	Wetting parameter, 1 [-]
X	Coefficient or force density at the liquid-vapour interface, unit varies
x_1	X-coordinate of a reattachment point of secondary bottom vortex [m]
x_2	X-coordinate of a reattachment point of primary bottom vortex [m]

x_3	X-coordinate of a separation point of top vortex [m]
x_4	X-coordinate of a reattachment point of top vortex [m]
x_n	Boundary cell size in the normal direction to the solid-fluid interface [m]
y^*	Dimensionless wall distance [-]
y^+	Dimensionless wall distance [-]
y_{vst}^+	Viscous sub-layer dimensionless thickness [-]
y_{wall}	Orthogonal distance from a boundary [m]
Z	Bubble area constant, 4 [-]
Greek	
α	Volume fraction [-]
α_{fc}	Minimum volume fraction for a phase to become fully continuous [-]
α_{pc}	Minimum volume fraction for a phase to become partially continuous [-]
χ	Hydrodynamic or thermodynamic variable to be converged, unit varies
δ	Distance between the boundary cell centre and the boundary face centre [m]
ϵ	Dissipation rate of turbulent kinetic energy [m^2/s^3]
η_k	Model constant for turbulence, 1.0 [-]
η_ϵ	Model constant for turbulence, 1.3 [-]
γ	Thermal diffusivity [$\text{kg}/(\text{m s})$]
κ	Thermal conductivity [$\text{W}/(\text{m K})$]

κ_{ra}	Thermal conductivity ratio, $\frac{\kappa_S}{\kappa_F}$ [-]
λ	Heat transfer coefficient [W/(m ² K)]
λ_q	Quenching heat transfer coefficient [W/(m ² K)]
μ	Dynamic viscosity [Pa s]
μ_{mix}	Mixture viscosity in dispersed flow [Pa s]
ν	Kinematic viscosity [m ² /s]
ω_{10}	Time residual accounting for a ten-second range [-]
Φ	Non-dimensionalised temperature [-]
$\phi_{mf,n}$	Mass flux through a boundary cell face [kg/s]
ϕ_{mf}	Mass flux [kg/s]
ϕ_{vf}	Volumetric flux [m ³ /s]
ψ	Latent heat [J/kg]
ρ	Density [kg/m ³]
σ	Surface tension coefficient, 0.07 [N/m]
θ	Interpolation factor for transition boiling [-]
ζ	Isentropic expansion factor for ideal gas, 5/3 [-]

Superscripts

C	Boundary cell value
I	Regions' interface value
i	Iteration label

Subscripts

c	Continuous phase
-----	------------------

<i>CD</i>	Conduction between solid and solid-fluid interface
<i>CV</i>	Convective heat transfer regime, allowing agitation
<i>CVB</i>	Convection between regions' interface and fluid phase, may include boiling effect
<i>d</i>	Dispersed phase
<i>Drag</i>	Drag force
<i>e</i>	Effective values to define densities within turbulence model
<i>eff</i>	Effective value, sum of molecular property and turbulent effect
<i>F</i>	Fluid, a combination of vapour and liquid
<i>f</i>	Liquid-vapour interface
<i>FB</i>	Film boiling heat transfer regime
<i>Fi</i>	Finish
<i>i</i>	Liquid-vapour interface at internal mesh
<i>j</i>	Represents liquid or vapour phase
<i>jk</i>	Effect of fluid phase "j" on fluid phase "k"
<i>k</i>	Represents liquid or vapour phase
<i>L</i>	Liquid phase
<i>Lift</i>	Lift force
<i>m</i>	Physical property (molecular value)
<i>max</i>	Maximum value
<i>min</i>	Minimum value
<i>mx</i>	Fluid phases' mixture

<i>NB</i>	Nucleate boiling heat transfer regime
<i>r</i>	Relative
<i>S</i>	Solid region
<i>SAT</i>	Saturation
<i>St</i>	Start
<i>TB</i>	Transition boiling heat transfer regime
<i>TD</i>	Turbulent dispersion force
<i>tot</i>	Total
<i>tr</i>	Effect of turbulence
<i>V</i>	Vapour phase
<i>VM</i>	Virtual mass force
<i>vr</i>	Validation results
<i>w</i>	Wall
<i>WL</i>	Wall lubrication force

Acronyms & Abbreviations

<i>AFRC</i>	Advanced Forming Research Centre
<i>Ag</i>	Agitation
<i>AMI</i>	Arbitrary Mesh Interface - interpolation procedure for non-conformal meshes
<i>Au</i>	Austenite
<i>B</i>	Bainite
<i>BC</i>	Boundary Condition

<i>BEM</i>	Boundary Element Method
<i>BFS</i>	Backward-facing Step
<i>CCT</i>	Continuum Cooling Transformation diagram
<i>CFD</i>	Computational Fluid Dynamics
<i>CHF</i>	Critical Heat Flux
<i>CoV</i>	Computational Volume
<i>CV</i>	Convective heat transfer regime, allowing agitation
<i>DIC</i>	Simplified Diagonal-based Incomplete Cholesky preconditioner
<i>DILU</i>	Simplified Diagonal-based Incomplete Lower-Upper preconditioner
<i>DNB</i>	Departure from Nucleate Boiling
<i>ETF</i>	Eulerian Two-Fluid method
<i>Eu</i>	Eutectoid
<i>FB</i>	Film Boiling
<i>FDB</i>	Fully Developed Boiling
<i>FDNB</i>	Fully Developed Nucleate Boiling
<i>Fe</i>	Iron
<i>Fe₃C</i>	Cementite (Iron carbide)
<i>Fr</i>	Ferrite
<i>Fr.</i>	Furnace
<i>GAMG</i>	Geometric Agglomerated algebraic MultiGrid (GAMG) numerical solver
<i>HTR</i>	Heat Transfer Regime

<i>IHCP</i>	Inverse Heat Conduction Problem
<i>Im.</i>	Specimen immersion
<i>IPC</i>	Interfacial Phase Change
<i>J1 – 10</i>	Locations used for validation of the cylinder quenching
<i>L1</i>	Location above the horizontal plate centre at solid-fluid interface
<i>L2</i>	Location at the horizontal plate centre
<i>L3</i>	Location beneath the horizontal plate centre at solid-fluid interface
<i>LDU</i>	Lower, Diagonal and Upper matrices
<i>LEID</i>	Leidenfrost
<i>M</i>	Martensite
<i>MHF</i>	Minimum Heat Flux
<i>MULES</i>	Multidimensional Universal Limiter for Explicit Solution
<i>NB</i>	Nucleate Boiling heat transfer regime
<i>NCV</i>	Natural convection
<i>OF</i>	OpenFOAM
<i>ONB</i>	Onside of Nucleate Boiling
<i>Op.</i>	Furnace opening and forklift positioning
<i>OpenFOAM</i>	Open-source Field Operation And Manipulation
<i>PBiCGStab</i>	Preconditioned Bi-Conjugate Gradient Stabilized numerical solver for asymmetric Lower, Diagonal and Upper matrices
<i>PCG</i>	Preconditioned Conjugate Gradient numerical solver for symmetric Lower, Diagonal and Upper matrices
<i>PDNB</i>	Partially Developed Nucleate Boiling

<i>Pl</i>	Pearlite
<i>RPI</i>	Rensselaer Polytechnic Institute
<i>S</i>	Still
<i>SAT</i>	Saturation
<i>TB</i>	Transition Boiling
<i>Tr.</i>	Specimen transport
<i>VR</i>	Validation Results

Chapter 1

Introduction

This chapter introduces the project motivation, defines its objectives and outlines the thesis structure. It continues by covering immersion quenching basics, including a literature review, describing key developments and finishes by indicating the work published to date which has originated from the thesis studies.

1.1 Motivation

Heat transfer between solids and fluids accompanies our everyday lives during various activities. Physicists and engineers name this phenomenon conjugate heat transfer. The least sophisticated occurrence is heat exchange between a solid surface and a single fluid, yet more fluids can be encountered. In certain circumstances, the heat might even be conjugated with a presence of a phase change. Such an example is immersion quenching: a metallurgical process that blacksmiths have utilised to alter metallic products properties. An early reference can be found in *The Odyssey* about 800 BC [1, 2]. Throughout history, much of the development continued across the Middle East, India, China and Japan [2]. Increased need for understanding came later with the Industrial Age [2]. Although people were able to acquire much knowledge about the process through millennia of practice, there is considerable room for improvement. Improper quenching can cause substantial secondary stresses, developed due to large temperature gradients, resulting in product damage [3]. Therefore, manufacturers would greatly benefit from a computational tool capable of predicting the mechanical properties of a

final product. The current status of computational methods for immersion quenching is discussed in detail in Section 1.4.4.

Quenching also happens under accidental conditions in nuclear reactors, superconductors and during chill-down of cryogenic liquid transfer systems [4]. In addition, boiling conjugate heat transfer is encountered during power generation [5–8], refrigeration and electronics cooling [9, 10].

1.2 Project objectives

The principal aim is to deliver a well functioning, efficient and accurate computational tool capable of predicting physics during the metallurgical manufacturing procedure called immersion quenching without accounting for material phase transformation within the quenched specimen. That leads to the following formulation of objectives:

- Conduct an in-depth literature review on computational approaches to immersion quenching. Determine state of the art in the field and identify the knowledge gap.
- Develop computational methodology capable of predicting temperature within a solid specimen during immersion quenching.
- Give a detailed description of the chosen computational methodology with a particular focus on conjugate heat transfer and boiling.
- Perform methodology validation against well-defined experimental problems. These should also serve other users as the computational setup examples.
- Avoid excessive needs for computational power while being able to perform simulations in a reasonable time for engineering applications. In other words, aim for the duration of hours to a couple of days using at maximum a few tens of up to date central processing units.
- Describe the methodology limitations and suggest future work.

1.3 Thesis outline

The thesis begins with an introduction to immersion quenching, including a brief discussion of metallurgy, various factors influencing the resulting solid specimen properties, and a detailed look at the heat transfer and computational approaches used in research. In this study, the dominant interest is in heat transfer and fluid dynamics rather than structural behaviour and phase transformation.

Chapter 2 provides an overview of the methodology with a more comprehensive view on the implementation of the wall boiling boundary condition and the calculation of the interface temperature deriving numerical Biot number governing the impact of all three phases, solid, liquid and vapour. Apart from these topics, the chapter addresses governing equations, including turbulence modelling and vapour volume fraction transport equation, interfacial terms, solution algorithm, numerics, and remarks on the Eulerian two-fluid model.

Chapter 3 discusses the first validation problem, which is laminar flow over a backward-facing step with conjugate heat transfer. The modelling approach is shown to be well suited for such a problem and proves to generate adequate results even for a one-phase flow problem. The chapter also indicates that one-phase flow problems can be used to validate two-phase flows methodologies.

The first validation problem with boiling appears in Chapter 4. The comparison is performed against experimental and numerical results acquired during quenching of a thin plate in its horizontal orientation. The dominant heat transfer regime, which is validated quantitatively, is film boiling. However, also other heat transfer regimes are encountered. Throughout this chapter, predominantly the numerical behaviour of the computational approach is discussed. Also, guidance for a successfully performed quenching simulation is formulated.

The most complex validation problem is a cylinder quenching in its vertical orientation (Chapter 5). The validation is more thorough as all the cylinder surfaces play an appreciable role and exhibit a particular behaviour. Moreover, temperature data from multiple locations are accessible for the whole range of the cooling process, and the role of submerging speed is also part of the investigation. Apart from the numerical behaviour, the physics is broadly discussed, and the experiment is analysed.

Finally, Chapter 6 concludes the project by the findings summary and the research questions discussion. The work is complemented by mentioning research contributions, limitations and suggestions for improvements.

1.4 Immersion quenching

Quenching is a heat treatment procedure used to process steel, alloy steel and non-ferrous alloy products to improve their properties [3]. Depending on the material and requirements, a metallic component is heated up to a specific temperature (465 - 1000 °C), followed by rapid cooling in a fluid, the quenchant.

This section further elaborates on metallurgy, heat transfer, factors affecting immersion quenching and state of the art in computational approaches to the subject.

1.4.1 Metallurgical view

This section provides a brief introduction to the metallurgy of quenching, a process aiming to exploit distinct properties of various steel microstructures. The study is later limited to fluid dynamics, not accounting for metallurgical changes within the quenched body. A reckoning with material phase transformation is doable yet outside the scope of this research. In addition, it would increase not only the computational complexity but also computational requirements.

Plain carbon steel is used as typical material requiring treatment by quenching. The $Fe - Fe_3C$ phase diagram (Fig. 1.1a) shows steel phase transformation for varying temperature and iron-carbon composition. Three phases, austenite (Au), ferrite (Fr) and cementite (Fe_3C), which eventually form microstructures such as pearlite (Pl) are recognised. During quenching, a workpiece is heated to an elevated temperature to form an austenitic phase. Then there are two general cooling scenarios. First, cooling is slow, and atoms have enough time to diffuse. Thus, the steel microstructure returns to its initial state. Second, the cooling rate is increased to such a level that no or limited atomic diffusion is allowed. That leads to microstructures not existing in the equilibrium state, martensite (M) and bainite (B). Understandably, that requires the employment of diagrams presenting the phase state as a function of time. An example would be the Continuum Cooling Transformation (CCT) diagram as depicted

in Fig. 1.1b. It shows four cooling rates and their influence on the microstructure, yet cooling rate is not the only factor affecting it. Initial workpiece temperature, chemical composition and grain size must also be considered together with shape and cross-section.

When the aim is to achieve steel with very high hardness, the austenite to martensite transformation is desirable. Optionally other microstructures such as bainite can be preferred. Martensite distinguishes itself with high hardness, however, increased brittleness also occurs.

Non-ferrous alloys are heated to solutionising temperature, temperature above solvus, to spread alloying elements in the primary metal. Afterwards, rapid cooling is performed. More information on metallurgy during immersion quenching can be read in the book by Liscis et al. [3]

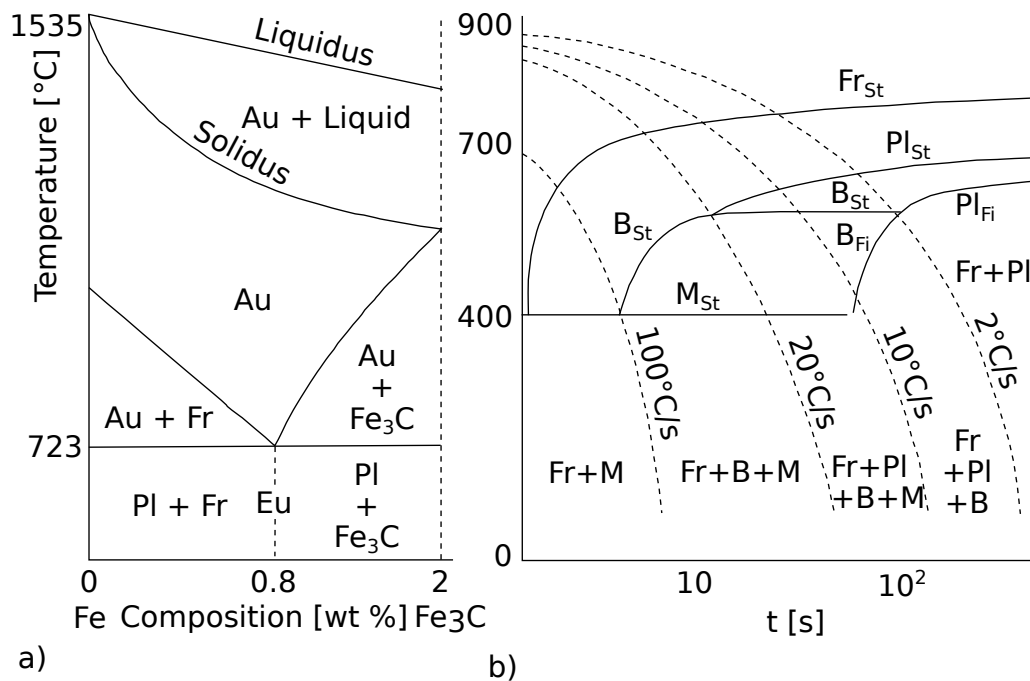


Figure 1.1: a) Simplified $Fe - Fe_3C$ phase diagram showing metastable equilibrium for plain steel [3]. b) Continuum Cooling Transformation diagram of SAE 1020 steel [3]. Au - Austenite; Fr - Ferrite; Pl - Pearlite; Fe_3C - Cementite; B - Bainite; M - Martensite; Eu - Eutectoid; Subscripts St and Fi stand for Start and Finish of transformation.

1.4.2 Heat transfer

A heat transfer at the interface between the sample and coolant dictates the cooling speed of a quenched sample. Its magnitude is controlled by solid material properties but also properties and hydrodynamics of quenchant. Considering still water, at atmospheric pressure, and extensive temperature range (substantially superheated sample), pool boiling is anticipated, and so is the appearance of various heat transfer regimes (HTRs). This behaviour was firstly exposed by Nukiyama [11] and can be viewed in Fig. 1.2. It shows the boiling curve commonly acquired from upward facing plate at pool boiling using the quasi-steady-state approach (solid line). Notice that HTRs are discussed from the right side, thus in the cooling direction, in contrast with the conventional approach, in the heating direction. Five different HTRs are discerned: film boiling (FB), transition boiling, also called partial film boiling (TB), fully developed nucleate boiling (FDNB), partially developed nucleate boiling (PDNB), and natural convection (NCV).

Two heat transfer controlled scenarios should be differentiated to understand Fig. 1.2. The transition boiling curve between critical and minimum heat fluxes can be reproduced if careful control of the heated surface temperature is practised (solid line). The other scenario is wall heat flux control, resulting in two distinct responses depending on the temperature rate, hence the direction of temperature change (dotted lines). Thus the latter results in the transition boiling omission and no existence of the Leidenfrost or burnout conditions as shown in the figure.

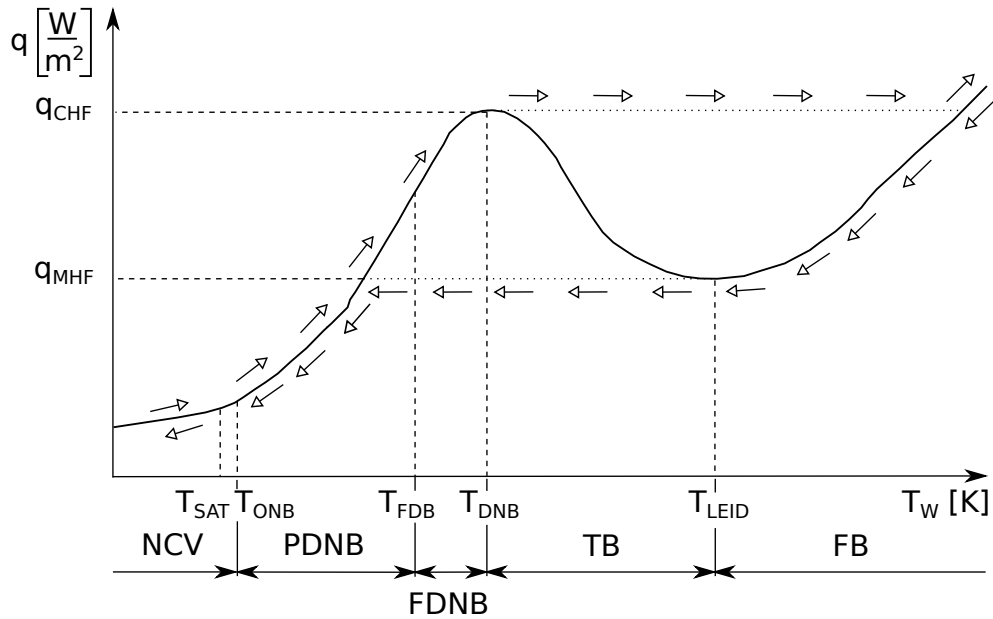


Figure 1.2: A qualitative boiling curve showing heating, cooling and influence of controlled variable. Heat transfer regimes: FB - Film boiling, TB - Transition boiling, FDNB - Fully developed nucleate boiling, PDNB - Partially developed nucleate boiling, NCV - Natural convection. The various subscripts: SAT - Saturation, ONB - Onset of nucleate boiling, FDB - Fully developed boiling, LEID - Leidenfrost, DNB - Departure from nucleate boiling, CHF - Critical heat flux, MHF - Minimum heat flux. Subscript w stands for heated wall.

Immersion quenching is sometimes employed to study the complete boiling curve as an alternative experimental procedure to an electrically heated specimen. Consequently, it is found that immersion quenching behaves similar to a controlled temperature condition. Nevertheless, quenching is a transient process. Therefore, it does not reproduce exact results from quasi-steady-state experimental work except for film boiling and natural convection. Research has revealed boiling curve hysteresis when transient experiments are performed (Fig. 1.3) [4].

Following the quenching logic, the HTRs are described from right to left as the metallic sample would be cooled. The boiling curve implementation for immersion quenching is discussed in Section 2.3.

Film boiling is generally delineated by a small heat transfer coefficient. A vapour layer obstructs the hot surface, leading to natural convection or conduction-like behaviour as a dominant heat transfer mechanism unless thermal radiation becomes significant [3]. Nonetheless, that is often disregarded because it plays a role only for largely overheated specimens with extensive film boiling [3, 12]. Even if radiation is considered

to be relevant, the conventional approach is to neglect its impact [13]. Radiation is dependent on the manufacturing setup (for instance, quenching tank), which makes it potentially computationally expensive if view factors are used, but also experimentally problematic for the determination of necessary properties [13]. Computationally cheaper, yet less general and accurate, is the usage of heat transfer correlations already including the radiation impact.

If the wall temperature is controlled and the Leidenfrost temperature T_{LEID} associated with minimum heat flux q_{MHF} is passed, the film boiling regime advances into the transition boiling regime. This regime is characterised by the influence of both nucleate boiling and film boiling. Their impact splits according to the contact between the surface and particular fluid phase. Given the different heat transfer coefficients of nucleate and film boiling, an uncontrolled variable, surface temperature or heat flux, tends to fluctuate.

The Leidenfrost temperature is often described as a phenomenon causing a prolonged droplet lifetime due to the development of a thin vapour cushion between the hot surface and liquid droplet. Naturally, for cooling, exactly the opposite behaviour is considered. Thus sudden decrease in the droplet lifetime due to insufficient vapour isolation. Several mechanisms have been investigated to describe the phenomenon and ascertain the conditions. However, despite the effort, models and correlations developed to determine the T_{LEID} and q_{MHF} remain a potential source of substantial inaccuracy [4].

As the surface is further cooled and heat flux increases, the wall temperature reaches the departure from nucleate boiling condition, T_{DNB} , sometimes called the burnout temperature. Beyond this point, fully developed nucleate boiling occurs. In many technologies employing boiling heat transfer and experiencing heating, only heat flux can be controlled. For these, the burnout point often marks a matter of safety as the elevated temperature can lead to boiling crises and equipment damage.

Once bubbles stop to coalesce and vapour structures such as columns and mushrooms disappear, fully developed nucleate boiling transitions into partially developed nucleate boiling. Observations show only isolated bubbles and further cooling accompanied by heat transfer coefficient decrease leading to the natural convection HTR. The

cooling rate substantially drops once the onset of nucleate boiling temperature T_{ONB} is passed. Surface cavities become deactivated, and latent heat with agitation resulting from bubbles dynamic are no longer exploited.

When heating takes place instead of cooling, the transition to partially developed nucleate boiling and so the development of bubbles can be delayed for certain liquids with good wetting properties. Cavities with trapped gases are activated later simultaneously, which is accompanied by an immediate surface temperature drop not witnessed during cooling (Fig. 1.3). This phenomenon is sometimes called a kickback [4].

During the last HTR, natural convection, only liquid is present at the solid-fluid region interface, and its movement is dictated by a density difference arising from the temperature gradient. As a result, it is characterised by a low heat transfer coefficient.

Boiling curve hysteresis emerges when comparing cooling and heating process employing transient experimental procedure where the controlled variable is wall temperature (Fig. 1.3). A similarity can be recognised recalling Fig. 1.2, where cooling and heating is distinguished when surface heat flux is the controlled variable. Fig. 1.3 shows significantly higher critical heat flux when the surface is heated, in contrast with surface cooling. It is thought that such behaviour results from contact angle hysteresis, thus the difference between advancing and receding contact angles. When a surface is heated, dry patches expand. Consequently, the contact angle approaches its minimum, receding contact angle. Effectively, a smaller contact angle leads to better wettability and increases q_{CHF} . On the other hand, dry patches reduce in extent when a surface is cooled, so the contact angle approaches its maximum, advancing angle. The phenomenon does not seem to occur for steady-state conditions, and as Ghiaasiaan [4] mentions, it is not fully understood.

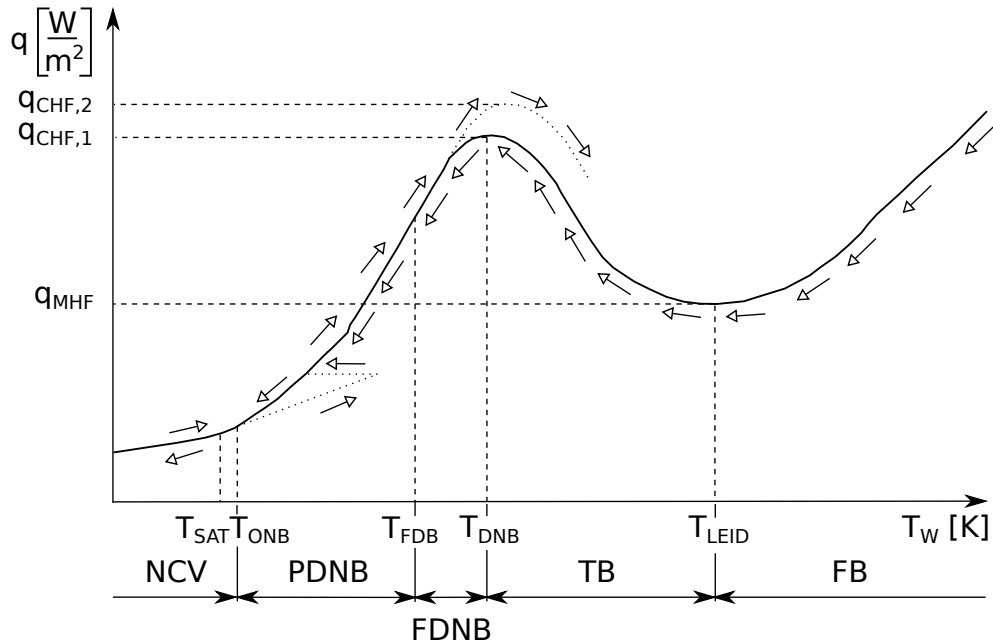


Figure 1.3: A qualitative boiling curve shows sudden temperature drop appearing during the transition from convective HTR to nucleate boiling HTR at heating conditions. Also, hysteresis is visualised during transition boiling, arising when the heated surface temperature is controlled and the process is transient.

1.4.3 Factors affecting quenching

Quenching is affected by several factors: quenchant temperature, velocity, type, and sample temperature, geometry, material, surface roughness [4], wettability [4], to name a few. This section attempts to give an overview of some of these factors and their effects.

Quenchant agitation

Section 1.4.2 looked into pool boiling, thus, cooling without any forced flow. Sometimes, however, usage of agitated coolant can be beneficial. It can help even the heat transfer coefficient distribution, hence to avoid temperature gradients and potential sample damage, and to increase the hardening depth [14]. These aims can prove challenging for complex geometries [15] and might be necessary for coolants with large ability of heat removal such as water and brine. Another use would be for aqueous polymers when resemblance to oil is desired [14]. An agitation has been shown to increase quenchant severity (Grossmann number, ability to remove heat from a workpiece) [3, 14], critical

heat flux [14, 16], reduce quenching time [17], disrupt polymer film and vapour blanket [14]. Nonetheless, it can also cause a mechanical degradation of polymers by breaking their chains [14] so decreasing polymer solution viscosity.

Some authors found research related to the effect of water velocity on film boiling inconclusive [18]. Nevertheless, it should be conceded that velocity impact varies profoundly depending on its vector, quenchant type, geometry and surface roughness. Computational Fluid Dynamics (CFD) can play a crucial role in predicting the coolant dynamics and assisting in the design of desired agitation patterns [19, 20].

Quenchant temperature

Quenchant temperature impact varies per its type. For example, considering water, decreased subcooling lowers the cooling rate and critical heat flux [4, 14], thickens vapour blanket, widens temperature range of film boiling [18], reduces the amount of evaporation energy, may enlarge bubble volume, decreases wetting front velocity because of smaller density difference [3] and can limit mechanical deformation due to more moderate heat transfer coefficient and more uniform cooling. Nevertheless, it does not influence minimum vapour film thickness [18].

Increased temperature of oils leads to decreased viscosity, resulting in raised cooling rates [3]. However, the change is not very apparent [21]. The temperature alternation is instead used to diminish thermal stress [14, 21] by temperature gradients reduction.

Sample orientation and geometry

Geometry complexity and its orientation is an essential aspect of quenching and must be taken into account considering agitation, gravitational acceleration and, in general, fluid dynamics induced by the presence of bubbles and density difference in the coolant. First, complex shapes might trap vapour in holes and pockets, leading to non-uniform heat transfer coefficient and sample destruction. In other words, geometry plays a vital role in fluid dynamics, the development of wetting fronts and local turbulence. Second, sample thickness can cause thermal stresses due to different cooling rates at various depths.

A noticeable example is a hot flat surface facing upwards, where bubbles are free to

detach, facing sideward, bubbles slide and coalesce before detachment, and finally facing downwards, where vapour becomes trapped and might form large vapour structures released chaotically. Furthermore, experiments have demonstrated that heat transfer coefficient rises for partially developed nucleate boiling, with an increased inclination angle of a horizontal plate initially facing upwards. Notwithstanding, fully developed nucleate boiling does not seem to be influenced [4].

It is well known that the Nusselt number, hence also the heat transfer coefficient, is a function of a characteristic length. In fact, the heat transfer coefficient around a sphere of bigger diameter becomes higher during film boiling, similarly with a flat plate at parallel flow configuration and its expanding length [18]. Moreover, a sphere and plate appeared to be wetted first at the lower side under velocity directed from the bottom [18]. Kopun et al. [22] performed an experiment by quenching a stepped plate in still water. They concluded that the thicker side of the plate should be submerged first. This approach leads to a smaller temperature gradient. Several other authors also investigated geometry orientation [23–26].

Quenchant type

Many quenchants, including water, brine, oils, polymer solutions, melted metals and gases, are utilised. However, their behaviour varies substantially even within its group type. For instance, there is a large distinction in heat removal between various polymer solutions [27], polymer concentrations [28] and oils [3].

Paramount is their ability to remove heat, thus fulfilling cooling requirements leading to martensitic and bainitic transformation. Other factors, however, must also be considered: reactivity, flammability, toxicity, cooling rate at specific temperature windows, removability of their residues and cost [3]. Fig. 1.4 shows cooling curves for various typical quenchants. Oils exhibit lower cooling rates and unequivocal film boiling in comparison with water or brine. Nevertheless, the latter might be a consequence of significantly lower subcooling.

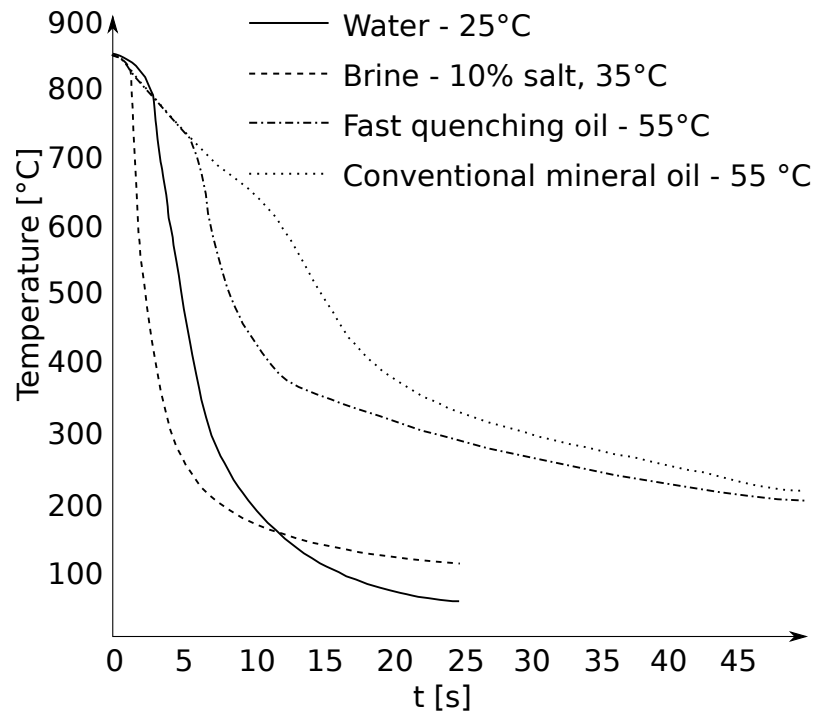


Figure 1.4: Cooling curves of various quenchants, including oils, water and brine [3]

The impact of polyalkylene glycol and its concentration in an aqueous solution is evident in Fig. 1.5. It shows that still water generates the highest cooling rates, but the polymer effect can be adjusted via its concentration and agitation to replicate a broad range of cooling curves. That is advantageous because it gives the potential to replace oils that are often hazardous for the environment and workers [3].

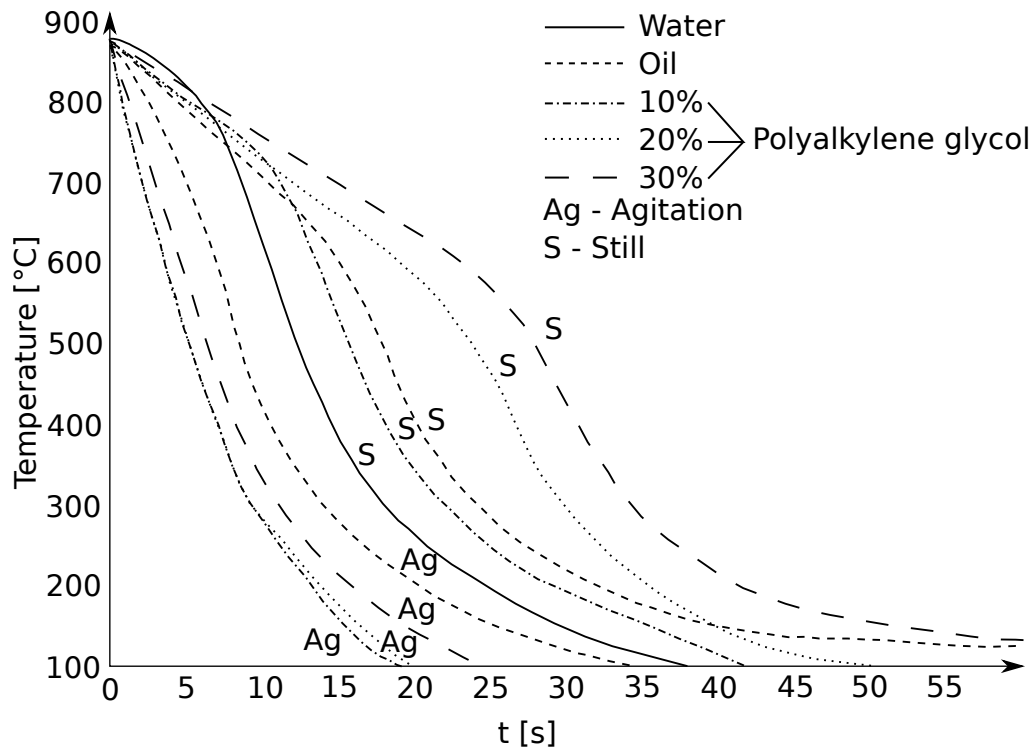


Figure 1.5: Cooling curves of various quenchant materials, including polymers at different concentrations with and without agitation [3]. The coolant temperature is between $38\text{ }^{\circ}\text{C}$ and $49\text{ }^{\circ}\text{C}$.

1.4.4 State of the art computational approaches

This section details state of the art in immersion quenching research using computational techniques. It aims at coolant behaviour and temperature field within the solid region. Phase/microstructure transformations and structural mechanics are not in the scope of this thesis.

There have been several research papers dedicated to computational techniques for immersion quenching [12, 22, 24–26, 29–36]. The majority of them have used AVL FIRE, a commercial simulation software specialised in internal combustion and components for electrified power trains. Wang et al. [29, 30] introduced the immersion quenching computational methodology within the software. They solved a conjugate heat transfer problem between solid and fluid regions by assessing the interface temperature and heat transfer coefficient. An energy equation governed the solid region. Meanwhile, the Eulerian two-fluid model (*ETF*) described the fluid behaviour using a separate set of continuity and momentum equations for each phase completed with a mixture energy equation. In addition, the authors assumed gas-phase, lumping vapour

and air together, which decreased computational needs. Finally, HTRs taken into account were film and nucleate boiling. Nevertheless, the nucleate boiling mass source was estimated based on a simplistic assumption when the film boiling mass source was multiplied by 100.

Subsequent studies heavily relied on and extended the AVL FIRE papers. Srinivasan et al. [25, 31] introduced a new approach for modelling the solid-fluid interface, implemented transition boiling HTR, modified the drag force definition and did not consider nucleate boiling HTR. They validated their results against a trapezoidal block sample and an aluminium alloy engine cylinder. Greif et al. [24] continued the work and combined the procedure with structural mechanics analysis in ABAQUS. The quenching of an engine cylinder head was also performed in subsequent work by Jan et al. [26]. Later on, variable Leidenfrost temperature, lift and wall lubrication interfacial momentum forces were taken into account by Kopun et al. [22, 32].

Further work with AVL FIRE considered separate energy equations for gas and liquid [33]. Nonetheless, the thermal homogeneous assumption was applied. Thus the interfacial phase heat transfer coefficient was set to a very high value which homogenised the equations. The last two research papers using AVL FIRE discussed the influence and calibration of various coefficients and values within the heat transfer framework, which usually need to be chosen and tuned to get valid results [34, 35].

Excluding the work done on AVL FIRE, there have been two other attempts to simulate the metallurgical process numerically. The first used the mixture model and bubble crowding in Fluent, allowing vaporisation and recondensation [12]. The second utilised the Finite Element - Galerkin method with monolithic coupling, tracking the liquid-vapour interface using the Level Set method and anisotropic mesh adaptation [36]. Compared with the *ETF* methodology, the latter approach uses only one set of Navier-Stokes equations but requires mixing laws. A lower number of governing equations offsets the necessity to resolve the liquid-vapour interface and the repetitive mesh generation. A monolithic approach prevents stability issues at the solid-fluid interface and proves to be often more efficient, yet it aggravates the governing equation implementation because the solid and fluid regions need to be described as a single system [37]. Khalloufi's approach [36] also required a liquid-vapour interface for the phase

change to occur. Thus, there was only one type of boiling, omitting the wall boiling used in the *ETF* approach. Due to the temperature range and well-presented data, the experimental and numerical results provided by Khalloufi [36] serve as validation data for the computational methodology in Chapter 4.

Immersion quenching is a complex process, and even though the computational research in the area is quite extensive, the success varies. Furthermore, computational results are often difficult or even impossible to reproduce due to lack of experimental and computational data, for instance, workpieces geometries, thermocouple locations, Leidenfrost temperature and bubble diameter.

1.5 Key developments

All work has been done in the framework of the open-source computational library OpenFOAM. Various versions have been used along the research journey, including releases from The OpenFOAM Foundation Ltd and Open CFD Ltd. Initially, within OpenFOAM 5.0, `chtMultiRegionFoam` was altered so the fluid region would be computed by `reactingTwoPhaseEulerFoam`. Apart from the solver logic, the work included the development of interface temperature and thermal turbulent diffusivity boundary conditions. Nevertheless, a suitable solver, which became the basis for further work, was released in OpenFOAM v1906 during the development period. Some code updates were made following subsequent releases if code patches were considered crucial. A list of significant modelling changes compared to the previous quenching research available in the literature are:

- Wall boiling boundary condition allowing to deal with complete boiling curve implemented via thermal turbulence diffusivity following Peltola et al. [38] and adapted to enable natural convection according to Jayatilleke [39] for two-phase flow, nucleate boiling using the Rensselaer Polytechnic Institute (RPI) mechanistic model [40], transition boiling following Srinivasan et al. [25] and film boiling employing the Bromley correlation [41].
- Separate energy equations for both fluid phases with heat and mass exchange employing Nusselt number correlations.

- Usage of multiple interfacial forces: drag, lift, wall lubrication, virtual mass, turbulent dispersion.
- Interfacial terms allowing phase inversion.

The main contributions of this work are the following:

- Validation of the solution approach on backward-facing step heat transfer problem.
- Validation against immersion quenching of a flat plate.
- Validation against a vertically quenched cylinder.
- Assessment of interfacial phase change effect.
- Derivation of local computational fluid Biot number and fluid temperature covering the effect of both fluid phases and wall boiling. The findings also apply to conjugate heat transfer between the solid phase and two other fluids without mass exchange.
- Formulating a procedure to assess simulation results of boiling conjugate heat transfer problem with various heat transfer regimes.
- Validation against quenching of high-temperature samples (about 960°C). The previous numerical simulations were usually carried out from the initial temperature of about 527 °C except for Krause et al. [12] whose research is limited to values about 727 °C.
- Bug, features and fix reports (Open CFD Ltd releases): #1592, #1606, #1694, #1789, #1860, #1909, #2312

Note also that multiple, predominantly post-processing features, measuring and debugging tools were developed within the OpenFOAM framework during the research. Only those relevant to the study are mentioned if found beneficial. Also, simulation examples and necessary source code to run them are available via GitHub (B)

1.6 Publications and Conferences

The work from this thesis has contributed to the following research papers:

1. Robin Kamenicky, Michael Frank, Dimitris Drikakis, Konstantinos Ritos. Film Boiling Conjugate Heat Transfer during Immersion Quenching. *Energies*, 15, 4258, 10.3390/en15124258, 2022
2. Robin Kamenicky, Michael Frank, Dimitris Drikakis, Konstantinos Ritos. Study of Nucleate Boiling Conjugate Heat Transfer, *Advances in Heat Transfer and Thermal Engineering*, 10.1007/978-981-33-4765-6_37, 2021.

Best student paper at the 16th UK Heat Transfer Conference, Nottingham.

The author also presented at the following conferences:

1. R. Kamenicky, M. Frank, D. Drikakis, K. Ritos. On Immersion Quenching Using an Euler-Euler Method. ECCOMAS Congress 2020 & 14th WCCM, 11-15 January 2021
2. Robin Kamenicky, Michael Frank, Dimitris Drikakis, Konstantinos Ritos. Study of Nucleate Boiling Conjugate Heat Transfer. 16th UK Heat Transfer Conference, Nottingham, 8-10 September 2019
3. Robin Kamenicky, Michael Frank, Dimitris Drikakis, Konstantinos Ritos. Heat Transfer Partitioning Models for Nucleate Boiling. ECCOMAS Thematic Conference CM4P, Porto, 15-17 July 2019

Chapter 2

Methodology

This chapter is dedicated to the methodology description, which includes governing equations, interfacial terms, modelling of boiling, derivation of fluid temperature and Biot number, regions' coupling procedure, solution algorithm, numerical solvers and schemes, and grid discretisation limitation posed by methodology.

Immersion quenching is a multiphysics and multiphase problem. Therefore it is decided to adopt a partitioned approach and split the computational domain into regions. It benefits from an option to dedicate a particular solver for each region. However, its drawback is a higher likelihood of instability [37, 42, 43]. The other option would be to employ the monolithic approach where fluid and solid regions are solved as one system. It profits from unconditional stability and computational efficiency, yet combining two very distinct solvers might prove challenging. It also decreases modularity because a new specific solver must be developed instead of using the already developed state of the art solvers for each region [37]. Furthermore, the monolithic approach might exhibit slower convergence because both regions are solved at each time step. Yet, in reality, heat transfer in the fluid region has a significantly smaller time scale than solid and converges quickly to steady-state. Therefore, in the partitioned approach, regions might be decoupled with different time steps and interface boundary condition updates only after a predefined number of time steps [37]. That being said, the advantage of the different time steps is not utilised within this research.

2.1 Governing equations

Immersion quenching as a three-phase problem is attempted to be solved employing a heat equation for the non-deformable solid region and the *ETF* method (Eulerian-Eulerian method), with two complete sets of Navier-Stokes equations and a turbulence model describing the two-phase fluid. Realistically air as a distinct gas phase could be taken into account. Nevertheless, identical properties with vapour are considered, as have been done in many previous studies without a lack of generality or accuracy [22, 24–26, 29–35]. In addition, necessary information is exchanged at the regions' interface via appropriate boundary condition.

2.1.1 Fluid region

The ETF solution methodology implies that each computational volume (CoV) holds both liquid and vapour at any time and location. Thus fluid phases penetrate each other, and their impact is controlled by volume fractions resulting from their transport equations. Also, the implication is that no interface is determined in comparison with interface capturing and tracking techniques. That makes it necessary to model their interaction at all levels, continuity, momentum, energy, and eventually turbulence. Theoretical analysis and governing equations derivation were given by Drew & Passman [44]. Certain aspects were also analysed by Michaelides et al. [45]

Hence, six volume averaged transport equations are solved: phase intensive conservation of mass, momentum and energy; together with turbulence equations and phase continuity equation to close the system. The expression *phase intensive* symbolises the fact that each fluid phase is represented by its own dedicated governing equations and variables.

The mass conservation is given by

$$\frac{\partial \alpha_j \rho_j}{\partial t} + \nabla \cdot (\alpha_j \rho_j \mathbf{u}_j) = \dot{m}_{jk}, \quad (2.1)$$

where α , ρ , t and \mathbf{u} are volume fraction, density, time, and velocity, respectively, and the subscripts j and k stand either for L – *liquid* or V – *vapour*, but $j \neq k$. Moreover,

\dot{m} is the mass source/sink accounting for the phase change

$$\dot{m}_{jk} = \dot{m}_{w,jk} + \dot{m}_{i,jk}, \quad (2.2)$$

where phase change at the wall \dot{m}_w (Section 2.3) and at a liquid-vapour interface \dot{m}_i (Section 2.2.3) are recognised.

Similarly, the conservation of momentum is given by

$$\begin{aligned} \frac{\partial \alpha_j \rho_j \mathbf{u}_j}{\partial t} + \nabla \cdot (\alpha_j \rho_j \mathbf{u}_j \mathbf{u}_j) &= -\alpha_j \nabla p + \Delta(\alpha_j \nu_{eff,j} \mathbf{u}_j) \\ + \alpha_j \rho_j \mathbf{g} - \alpha_k (\rho_j - \rho_k) \mathbf{g} &+ (\dot{m}_{jk} \mathbf{u}_k - \dot{m}_{kj} \mathbf{u}_j) + F_{jk}, \end{aligned} \quad (2.3)$$

where p denotes the pressure field, which is common for both fluid phases. \mathbf{g} stands for the acceleration due to gravity, and ν_{eff} is the effective viscosity $\nu_{eff,j} = \nu_{m,j} + \nu_{tr,j}$, where ν_m is the kinematic viscosity, and ν_{tr} is the turbulent viscosity. Describing the equation from the left-hand side, temporal, convective, pressure and diffusive terms are recognised. These are followed by source terms due to gravity, buoyancy resulting from the phases density difference, momentum change emerging from boiling and condensation and interfacial forces F_{jk} dictated by the fluid phases momentum interaction (Section 2.2.1).

Following on, the conservation of energy in the form of specific enthalpy can be written as

$$\begin{aligned} \frac{\partial \alpha_j \rho_j h_j}{\partial t} + \nabla \cdot (\alpha_j \rho_j h_j \mathbf{u}_j) + \frac{\partial \alpha_j \rho_j K_j}{\partial t} + \nabla \cdot (\alpha_j \rho_j K_j \mathbf{u}_j) - \Delta(\alpha_j \gamma_{eff,j} h_j) &= \\ \alpha_j \rho_j (\mathbf{u}_j \cdot \mathbf{g}) + H_j (T_f - T_j) + (\dot{m}_{jk} h_k - \dot{m}_{kj} h_j) + (\dot{m}_{jk} K_k - \dot{m}_{kj} K_j), \end{aligned} \quad (2.4)$$

where h represents specific enthalpy; $K_j = \frac{1}{2} |\mathbf{u}_j|^2$, and $\gamma_{eff,j} = \gamma_{m,j} + \gamma_{tr,j}$ is the effective thermal diffusivity with γ_m, γ_{tr} standing for molecular thermal diffusivity and turbulent thermal diffusivity, respectively. H is the sensible interfacial heat transfer coefficient evaluated as a product of the interfacial area concentration ($A_{ic} = \frac{6\alpha_d}{D_d}$) and the heat transfer coefficient calculated following correlations estimating the Nusselt number (Section 2.2.2). Subscripts d and c denote dispersed and continuous phase, respectively, while D is the particle diameter of a phase. The equation terms represent

temporal change and convection for kinetic energy and specific enthalpy followed by diffusion, change due to gravity, energy exchange with the liquid-vapour interface and specific enthalpy and kinetic energy sources due to boiling and condensation. Finally, T_f is the liquid-vapour interface temperature

$$T_f = \frac{H_L}{H_L + H_V} T_L + \frac{H_V}{H_L + H_V} T_V + \frac{\dot{m}_i \psi}{H_L + H_V}, \quad (2.5)$$

where ψ is latent heat. The third term on the RHS disappears for no interfacial phase change (IPC).

Turbulence is taken into account through the use of the fluid phases mixture $k - \epsilon$ model by Behzadi et al.[46] A difference is the consideration of turbulence generation due to the presence of bubbles [47] and usage of an effective density for averaging.

Firstly, the mixture turbulent kinetic energy k_{mx} transport equation is introduced:

$$\frac{\partial k_{mx}}{\partial t} + \nabla \cdot (\mathbf{u}_{mx} k_{mx}) - \Delta \left(\frac{\nu_{tr,mx}}{\eta_k} k_{mx} \right) = G_{mx} - \frac{2}{3} k_{mx} \nabla \cdot \mathbf{u}_{mx} - \epsilon_{mx} + G_b \frac{1}{\rho_{mx}}, \quad (2.6)$$

where subscript mx stands for a mixture of the fluid phases, G_{mx} is the mixture turbulence production, and G_b is the generation of turbulence due to bubble presence.

The transport equation for the dissipation rate of the turbulent kinetic energy mixture ϵ_{mx} follows

$$\begin{aligned} \frac{\partial \epsilon_{mx}}{\partial t} + \nabla \cdot (\mathbf{u}_{mx} \epsilon_{mx}) - \Delta \left(\frac{\nu_{tr,mx}}{\eta_\epsilon} \epsilon_{mx} \right) = \\ C_1 G_{mx} \frac{\epsilon_{mx}}{k_{mx}} - \frac{2}{3} C_1 \epsilon_{mx} \nabla \cdot \mathbf{u}_{mx} - C_2 \frac{\epsilon_{mx}^2}{k_{mx}} + C_3 G_b \frac{\epsilon_{mx}}{\rho_{mx} k_{mx}}. \end{aligned} \quad (2.7)$$

The model constants are $\eta_\epsilon = 1.3$, $\eta_k = 1$, $C_1 = 1.44$, $C_2 = C_3 = 1.92$ [48].

The mixture of the turbulent kinetic energy k_{mx} and the mixture dissipation rate ϵ_{mx} are:

$$k_{mx} = \frac{\alpha_L \rho_{e,L} k_L + \alpha_V \rho_{e,V} k_V}{\rho_{mx}} \quad (2.8)$$

and

$$\epsilon_{mx} = \frac{\alpha_L \rho_{e,L} \epsilon_L + \alpha_V \rho_{e,V} \epsilon_V}{\rho_{mx}}, \quad (2.9)$$

where $\rho_{e,L} = \rho_L$, and $\rho_{e,V} = \rho_V + C_{VM} \rho_L$, C_{VM} is virtual mass coefficient defined in Section 2.2.1.

Mixture velocity \mathbf{u}_{mx} :

$$\mathbf{u}_{mx} = \frac{\alpha_L \rho_{e,L} \mathbf{u}_L + \alpha_V \rho_{e,V} \mathbf{u}_V C_{t2}}{\alpha_L \rho_{e,L} + \alpha_V \rho_{e,V} C_{t2}}. \quad (2.10)$$

Turbulence production of the mixture G_{mx} :

$$G_{mx} = \frac{\alpha_L \rho_{e,L} G_L + \alpha_V \rho_{e,V} G_V}{\rho_{mx}}, \quad (2.11)$$

where G_L and G_V are turbulence productions related to each fluid phase.

Mixture density:

$$\rho_{mx} = \alpha_L \rho_{e,L} + \alpha_V \rho_{e,V}. \quad (2.12)$$

Lastly, the turbulent viscosity of the mixture:

$$\nu_{tr,mx} = \frac{\alpha_L \rho_{e,L} \nu_{tr,L} + \alpha_V \rho_{e,V} \nu_{tr,V} C_{t2}}{\alpha_L \rho_{e,L} + \alpha_V \rho_{e,V} C_{t2}}, \quad (2.13)$$

where C_{t2} is a response coefficient.

Finally, the phase continuity equation obeying $\alpha_L + \alpha_V = 1$ is derived from a form developed by Weller [49] following the need for a conservative and bounded equation

$$\frac{\partial \alpha_V}{\partial t} + \nabla \cdot (\mathbf{u}_{tot} \alpha_V) + \nabla \cdot (\mathbf{u}_r \alpha_V (1 - \alpha_V)) = \alpha_V Sp + Su \quad (2.14)$$

where \mathbf{u}_{tot} and \mathbf{u}_r are the total and relative velocities of the fluid phases

$$\mathbf{u}_{tot} = \alpha_j \mathbf{u}_j + \alpha_k \mathbf{u}_k, \quad (2.15)$$

$$\mathbf{u}_r = \alpha_j \mathbf{u}_j - \alpha_k \mathbf{u}_k. \quad (2.16)$$

While Sp and Su are source terms related to dilatation rates accounting for the pressure equation's compressible part and mass transfer between the fluid phases. Eq. (2.14) is further utilised in a form developed by Rusche [50] to account for turbulent dispersion,

which is proportional to $\nabla\alpha_V$. This term, however, can result in a checker-boarding issue when coupling momentum and phase fraction continuity equations. Therefore a similar approach to Rhie & Chow [51] is adopted [50].

2.1.2 Solid region

The sole equation to solve in the solid region is energy conservation. No metallurgical or mechanical fields are taken into account. In reality, the system is more complex, and phase transformation, as well as the possible plastic deformation, generate heat [3]. Nonetheless, this work is concentrated mainly on conjugate heat transfer and fluid dynamics as the primary research areas.

The solid energy equation is presented in the form of specific enthalpy as a more general form than a temperature equation for the user convenience and code compliance:

$$\frac{\partial \rho_S h_S}{\partial t} - \Delta(\gamma_S h_S) = 0, \quad (2.17)$$

where subscript S stands for the solid region. γ is thermal diffusivity defined as $\gamma_S = \frac{\kappa_S}{c_{p,S}}$, which results in the equation with units of the energy rate per cubic meter following the time and space discretisation. κ represents thermal conductivity and c_p isobaric specific heat capacity.

2.2 Interfacial terms

Due to the usage of the *ETF* method, the fluid phases interactions must be modelled. That applies to all governing equations, thus continuity, momentum and energy.

Both fluid phases can occur in various two-phase flow regimes. Nevertheless, only dispersed and continuous states are considered not accounting for segregated flow. Regardless of the actual phase flow regime, interfacial models for both continuous and dispersed flows are utilised for each phase at every cell and time step of the simulation and results are blended using a weighting function.

$$X_k = w_{c,k} X_{c,k} + w_{d,k} X_{d,k}, \quad (2.18)$$

where X stands for various coefficients/forces depending on the interfacial term of interest and w is the weighting value following piecewise linear approximation (Fig. 2.1):

$$\begin{aligned} w_{c,k} &= \min \left(\max \left(\frac{\alpha_k - \alpha_{pc,k}}{\alpha_{fc,k} - \alpha_{pc,k}}, 0 \right), 1 \right), \\ w_{d,k} &= \min \left(\max \left(\frac{\alpha_j - \alpha_{pc,j}}{\alpha_{fc,j} - \alpha_{pc,j}}, 0 \right), 1 \right), \end{aligned} \quad (2.19)$$

where α_{pc} represents the minimum volume fraction to become partially continuous under which $w_{c,k} = 0$ and α_{fc} represents minimum volume fraction to become fully continuous, above which $w_{c,k} = 1$. If $\alpha_{pc,j} = \alpha_{pc,k}$, $\alpha_{fc,j} = \alpha_{fc,k}$ and $\alpha_{pc,k} + \alpha_{fc,k} = 1$ then Eq. (2.18) simplifies because $w_{c,k} = 1 - w_{d,k}$, which is the case for all following simulations. Values α_{pc} and α_{fc} can differ for momentum and heat transfer interfacial terms depending on the flow regimes governing models, their applicability and user considerations.

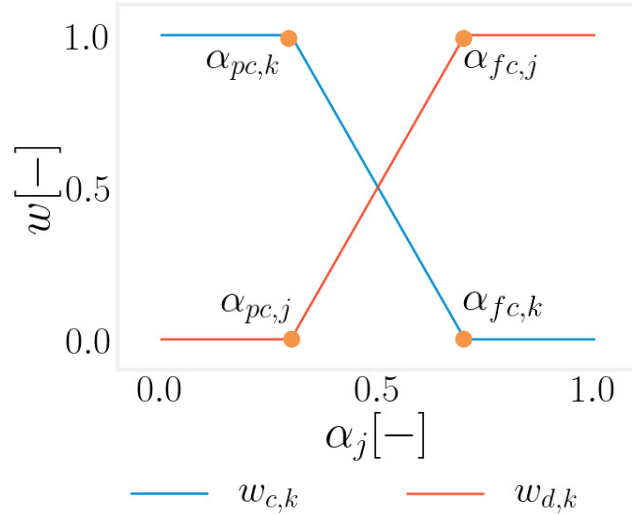


Figure 2.1
Piecewise linear weighting functions.

To calculate the interfacial terms, the bubble/droplet Sauter mean diameter is also needed. Here the bubble diameter is assumed to be 3 mm at atmospheric pressure, subjected to pressure changes but no thermal expansion, coalescence, breakup or bubble crowding. In contrast, the droplet diameter is constant at 0.45 mm. The author is aware that bubble dynamics may play a significant role. An alternative would be to use correlations [52] or a more complex approach like Interfacial Area Transport Equation

[53] or Population Balance [54]. Nevertheless, particular bubble dynamics approaches were developed/tested for specific conditions such as subcooling, pressure, heat transfer regime and forced flow. Moreover, the validation problems, in this project, include considerable boiling on the horizontal surfaces, potentially leading to large bubbles if the *IPC* is not allowed, and to violation of the *ETF* fundamental assumption. Dispersed particle Sauter mean diameter should not exceed the smallest dimension of a CoV it is present in (more in Section 2.7). That can result in numerical instability or a need to coarsen the mesh beyond the level needed to resolve the flow dynamics. Due to these complexities, the influence of particle diameter is considered out of the research scope. Their values were chosen to comply with the experimental temperature results, thus used rather as a solution parameter.

2.2.1 Momentum

Multiple forces can arise as a result of phase interaction. This work considers drag \mathbf{F}_{Drag} , lift \mathbf{F}_{Lift} , wall lubrication \mathbf{F}_{WL} , virtual mass \mathbf{F}_{VM} and turbulent dispersion \mathbf{F}_{TD} forces.

The drag force is estimated using the following equation

$$\mathbf{F}_{Drag,c} = -\mathbf{F}_{Drag,d} = 0.75\alpha_d C_D C_S \frac{\rho_c \nu_{m,c}}{D_d^2} (\mathbf{u}_d - \mathbf{u}_c). \quad (2.20)$$

Swarm coefficient C_S is assumed to be equal to 1. C_D is a drag coefficient multiplied by Reynolds number and estimated using the Ishii & Zuber correlation [55] accounting for various flow regimes (viscous, Newton, distorted, churn turbulent flow):

$$C_D = \begin{cases} \min(C_{D,Re,Elp}, 2.66667 Re_p \alpha_c^2) & C_{D,Re} \leq C_{D,Re,Elp} \\ C_{D,Re} & C_{D,Re} > C_{D,Re,Elp}, \end{cases} \quad (2.21)$$

where the drag coefficient $C_{D,Re,Elp}$ stands for distorted particle regime

$$C_{D,Re,Elp} = 0.6666 \frac{1 + 17.67 f^{0.8571428}}{18.67 f} \sqrt{Eo Re_p}, \quad (2.22)$$

$$f = \min\left(\frac{\mu_c}{\mu_{mix}}\sqrt{\alpha_c}, 0.001\right), \quad (2.23)$$

and drag coefficient $C_{D,Re}$ for viscous regime or constant 0.44 for Newton regime depending on modified Reynolds number Re_M

$$C_{D,Re} = \begin{cases} 24(1 + 0.1Re_M^{0.75}) & Re_M \leq 1000 \\ 0.44Re_M & Re_M > 1000, \end{cases} \quad (2.24)$$

$$Re_M = Re_p \frac{\mu_c}{\mu_{mix}}, \quad (2.25)$$

$$\mu_{mix} = \mu_c(\max(\alpha_c, 0.001))^{-2.5\frac{\mu_d+0.4\mu_c}{\mu_d+\mu_c}}. \quad (2.26)$$

The Eötvös number Eo is estimated accordingly

$$Eo = |\rho_d - \rho_c| \frac{|\mathbf{g}|D_d^2}{\sigma}, \quad (2.27)$$

where $\sigma = 0.07 \text{ N/m}$ stands for surface tension coefficient. μ is dynamic viscosity and Re_p represents the particle Reynolds number of a continuous phase calculated using the relative velocity and diameter of bubble/droplet:

$$Re_p = \frac{|\mathbf{u}_d - \mathbf{u}_c|D_d}{\nu_{m,c}}. \quad (2.28)$$

The lift force is meant to model a lateral force acting on bubbles due to velocity gradient and is governed by the following equation

$$\mathbf{F}_{Lift,c} = -\mathbf{F}_{Lift,d} = \alpha_d C_l \rho_c (\mathbf{u}_d - \mathbf{u}_c) \times (\nabla \times \mathbf{u}_c), \quad (2.29)$$

where C_l is the lift coefficient estimated according to Tomiyama et al. [56], yet altered

to maintain the model continuous over the whole range of Eo_H :

$$C_l = \begin{cases} \min(0.288 \tanh(0.121 Re_p), f_l) & Eo_H < 4 \\ f_l & 4 \leq Eo_H < 10.7 \\ -0.288 & 10.7 \geq Eo_H, \end{cases} \quad (2.30)$$

where Eo_H is the modified Eötvös number calculated using the aspect ratio $E_a = 1$, thus spherical particle

$$Eo_H = |\rho_d - \rho_c| \frac{|g| \left(\frac{D_d}{\sqrt[3]{E_a}} \right)^2}{\sigma}. \quad (2.31)$$

f_l is a polynomial function of Eo_H

$$f_l = 0.0010422 Eo_H^3 - 0.0159 Eo_H^2 - 0.0204 Eo_H + 0.474. \quad (2.32)$$

The third force to be modelled is the wall lubrication force representing lateral force due to the wall proximity and its impact on velocity distribution around a bubble. It prevents bubbles from staying at the wall, which might result from surface tension. That is modelled as proposed by Antal et al. [57]

$$\mathbf{F}_{WL,c} = -\mathbf{F}_{WL,d} = -\alpha_d \left(\frac{C_{WL,1}}{D_d} + \frac{C_{WL,2}}{y_{wall}} \right) \rho_c |((\mathbf{u}_d - \mathbf{u}_c) - ((\mathbf{u}_d - \mathbf{u}_c) \cdot \hat{\mathbf{n}}_w) \hat{\mathbf{n}}_w)|^2 (-\hat{\mathbf{n}}_w). \quad (2.33)$$

The constants $C_{WL,1} = -0.01$, $C_{WL,2} = 0.05$ [54]; y_{wall} is the orthogonal distance from the wall, and $\hat{\mathbf{n}}_w$ is the boundary face normal unit vector.

The virtual mass force arises because the liquid must accelerate simultaneously with the bubble:

$$\mathbf{F}_{VM,c} = -\mathbf{F}_{VM,d} = \alpha_d C_{VM} \rho_c \left(\frac{D\mathbf{u}_d}{Dt} - \frac{D\mathbf{u}_c}{Dt} \right), \quad (2.34)$$

where $\frac{D}{Dt}$ is the material derivative, C_{VM} is a constant equal to 0.5 [54].

The last force taken into account is the turbulent dispersion

$$\mathbf{F}_{TD,c} = -\mathbf{F}_{TD,d} = C_{TD}\nabla\alpha_d, \quad (2.35)$$

where C_{TD} stands for turbulent dispersion coefficient defined according to Burns [58] as implemented by Otromke[59]

$$C_{TD} = 0.75C_D\rho_c\alpha_d\frac{\nu_{m,c}\nu_{tr,c}}{ScD_d^2}\left(\frac{1}{\alpha_d} + \frac{1}{\alpha_c}\right), \quad (2.36)$$

where turbulent bubble Schmidt number $Sc = 0.7$.

For simplicity, the forces modelling are summarised in Table 2.1. It can be seen that when vapour is continuous, lift, wall lubrication and turbulent dispersion forces are not modelled. Thus, due to the blending Eq. (2.18), these forces become suppressed as the volume fraction rises. Also, due to Newton's third law, \mathbf{X}_k is calculated only for one fluid phase. The force on the other phase is its reaction. The blending function constants α_{pc} and α_{fc} are equal to 0.3 and 0.7, respectively.

Finally, employing the Eq. (2.18) and summing over all forces effects

$$\sum \mathbf{F}_{jk} = \mathbf{F}_{Lift,jk} + \mathbf{F}_{WL,jk} + \mathbf{F}_{Drag,jk} + \mathbf{F}_{VM,jk} + \mathbf{F}_{TD,jk} = -\sum \mathbf{F}_{kj}, \quad (2.37)$$

the interfacial force density source term in Eq. (2.3) is evaluated.

2.2.2 Heat transfer

The fluid phases' interaction is not only present at the level of momentum but also in heat transfer. That requires defining Nusselt number Nu correlations for each fluid phase, as referenced in Table 2.1. Nu of the continuous phase is correlated by Ranz and Marshall [60]

$$Nu = 2 + 0.6Re_p^{1/2}Pr^{1/3}, \quad (2.38)$$

where the Prandtl number is defined as follows

$$Pr = \frac{\nu_{m,c}c_p c \rho_c}{\kappa_c}. \quad (2.39)$$

Nu for dispersed phase is equal to 10, and as the model name "spherical" suggests (Table 2.1), it corresponds to an analytical solution of heat transfer from the sphere surface to the internal fluid [61].

Once Nusselt numbers are estimated, the heat transfer coefficients are evaluated and used in Eqs. (2.4, 2.5, 2.40). Finally, both fluid phases are considered to be always partially continuous, hence $\alpha_{pc} = 0$ and $\alpha_{fc} = 1$.

	Dispersed vapour	Continuous vapour
Drag	Ishii & Zuber [55]	Ishii & Zuber [55]
Lift	Tomiyama [56]	-
Wall Lubrication	Antal [57]	-
Virtual Mass	Constant	Constant
Turbulent Disp.	Burns [58], Otromke [59]	-
Nu (vapour side)	Spherical	Ranz & Marshall [60]
Nu (liquid side)	Ranz & Marshall [60]	Spherical

Table 2.1: Momentum and heat transfer interfacial models.

2.2.3 Interfacial phase change

IPC is employed to account for condensation and boiling at the liquid-vapour interface, not at the heated wall. The primary assumption is that the interface is at the saturation point. Then the following equation can be written

$$\dot{m}_i = \frac{H_L(T_{SAT} - T_L) + H_V(T_{SAT} - T_V)}{\psi}, \quad (2.40)$$

where T_{SAT} stands for saturation temperature.

Substituting Eq. (2.40) into Eq. (2.5), it is seen that $T_f = T_{SAT}$. Further, analysing Eq. (2.40), it can be perceived that the heat fluxes in the numerator depend on the volume fraction of the dispersed phase because H is defined using interfacial area concentration (Section 2.1.1). Correctly, it results in no condensation or boiling when a dispersed phase is not present. Nonetheless, recalling the assumption that we treat

the air as vapour, we experience condensation where liquid and air face each other. In many cases, this is not problematic, for instance, in quenching applications where the liquid-air interface is far from the area of interest. However, the user should be aware of it and examine its impact on different applications.

2.3 Wall boiling

This section describes the logic needed to cope with various *HTRs*. Wall boiling modelling is a vital part of the solution methodology to satisfy the energy conservation at the fluid-solid interface and to influence the numerical stability. The work by Srinivasan et al. [25], Peltola et al. [38], Kurul & Podowski [40], and Jayatilleke [39] is followed. These approaches have not been previously combined in the literature.

Taking Fig. 1.2, assuming quenching, and nucleate boiling (*NB*) *HTR* covering *FDNB* and *PDNB*, the problem can be simplified to Fig. 2.2. Also, natural convection *HTR* is assumed to allow agitation, thus the regime is labelled with *CV* for convective heat transfer.

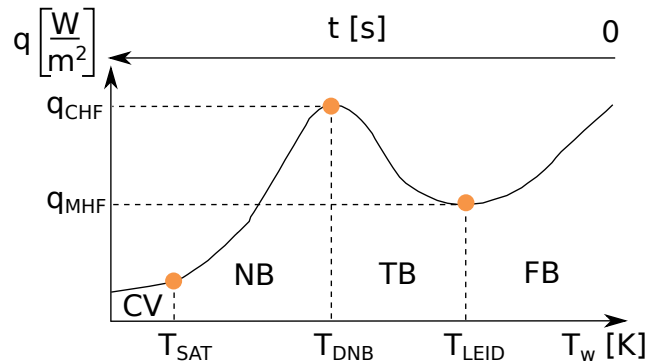


Figure 2.2: Heat transfer regimes. FB - Film boiling, TB - Transition boiling, NB - Nucleate boiling, CV - convective heat transfer. The various subscripts meanings follow: LEID - Leidenfrost, DNB - departure from nucleate boiling, SAT - saturation, MHF - minimum heat flux, CHF - critical heat flux

The curve in Fig. 2.2 is only qualitative and serves as a generic curve showing the heat transfer from the solid region. In fact, heat is partitioned into each fluid phase according to volume fractions (see Eq. 2.41). Moreover, Table 2.2 shows that regimes *TB*, *NB* assume convective heat transfer for the vapour phase, whereas, for liquid, various definitions depending on the particular *HTR* are considered. Calculations re-

lated to the boiling curve, hence heat transfer coefficients, use the turbulent thermal diffusivity $\gamma_{tr,j}$ boundary condition (*BC*). That allows the information to propagate into the energy conservation equations via the diffusion coefficients.

	$T_w < T_{SAT}$	$T_{SAT} \leq T_w < T_{DNB}$	$T_{DNB} \leq T_w < T_{LEID}$	$T_{LEID} \leq T_w$
Vapour	Convective h. t.	Convective h. t.	Convective h. t.	Film b.
Liquid	Convective h. t.	Nucleate b.	Transition b.	Film b.

Table 2.2: Heat transfer regimes partitioning

The total heat flux from the solid-fluid interface to the fluid

$$q_{tot} = \alpha_L q_L + \alpha_V q_V, \quad (2.41)$$

where q_L can be substituted with $q_{FB,L}$, q_{TB} , q_{NB} or $q_{CV,L}$. Subscripts *FB*, *TB*, *NB* and *CV* represent film boiling, transition boiling, nucleate boiling and convective HTR, respectively. q_V stands for $q_{FB,V}$ or $q_{CV,V}$.

Following the suggestion by Končar et al. [62], temperature $T_{int,L}$ is used instead of boundary cell temperature, where appropriate throughout the boundary condition. It is estimated by interpolating the logarithmic thermal boundary layer profile in the vicinity to the solid-fluid interface using the boundary cell dimensionless T^+ and T^{+250} at $y^+ = 250$.

T^{+250} at $y^+ = 250$ is estimated from

$$T^{+250} = Pr_t \left(\frac{\ln(E250)}{C_\kappa} + P \right), \quad (2.42)$$

and by analogy, the T^+ at the y^+ of the boundary cell

$$T^+ = Pr_t \left(\frac{\ln(Ey^+)}{C_\kappa} + P \right), \quad (2.43)$$

where Pr_t is the turbulent Prandtl number equal to 0.85 [63]. E is a model coefficient equal to 9.8, and C_κ is the Von Karman constant equal to 0.41 [63]. P is defined by

Jayatilleke [39] as follows

$$P = 9.24 \left(\left(\frac{Pr}{Pr_t} \right)^{0.75} - 1 \right) \left(1 + 0.28 e^{-0.007 Pr / Pr_t} \right), \quad (2.44)$$

and y^+

$$y^+ = \frac{u_\tau y}{\mu / \rho}, \quad (2.45)$$

where the friction velocity is based on the definition using turbulent kinetic energy

$$u_\tau = C_\mu^{0.25} \sqrt{k}, \quad (2.46)$$

which allows avoiding iteration between shear stress and y^+ , and issues with stagnation and separation flows. Thus, mentioning the conventional nomenclature Eq. (2.45) calculates y^* , but the OpenFOAM documentation is followed, and variable y^+ is used instead [48, 63]. An empirical model coefficient $C_\mu = 0.09$ [48].

Finally, the temperature $T_{int,L}$ at T^{+250} is evaluated using linear interpolation

$$T_{int,L} = \max \left(T^C - 40, T^I - \frac{T^{+250}}{T^+} (T^I - T^C) \right), \quad (2.47)$$

and is limited, to prevent excessive subcooling. Superscripts C and I represent boundary cells and the solid-fluid interface values.

Determination of the highlighted values from Fig. 2.2 might be complicated and a source of substantial error. That is because they are a function of many parameters: liquid subcooling, solid superheat, surface roughness, agitation, geometry (direction of submersion), fluid and solid properties [3], to list a few. The following paragraphs shortly introduce the choices to their evaluation using methods that combine accuracy with computational efficiency.

Due to the dependency of T_{LEID} on many parameters, models and correlations exhibit substantial uncertainty and can prove to be often inaccurate [4]. Therefore, the T_{LEID} is defined as a constant value equal to 277 °C in Chapter 4, based on the validation experiment [36], and 986.85 °C in Chapter 5. The value is increased following the particular experiment and the observation that film boiling cannot be forced on the BC. It can be only replicated via vapour volume fraction. The chosen value is above

the solid initial temperature.

T_{DNB} in Chapter 4 is estimated according to Schroeder's work [64]

$$T_{DNB} = \frac{T_{SAT}}{1 - \frac{\ln(2\zeta+1)\bar{R}T_{SAT}}{W\psi}}, \quad (2.48)$$

where ζ is the isentropic expansion factor for ideal gas equal to 5/3. Although no negative impact of using this value has been observed, users should consider a more appropriate quenching fluid value (for water vapour as triatomic gas 8/6). \bar{R} is the ideal gas constant equal to 8.31447 J/(K mol) and W stands for molecular weight equal to 0.0180153 kg/mol. Chapter 5 defines $T_{DNB} = 226.85$ °C.

Having this information, an explanation of the heat transfer evaluations during each HTR can proceed. In the film boiling HTR, the heat transfer coefficient λ_{FB} is estimated using the correlation by Bromley [41] neglecting heat transfer by radiation, as has been discussed earlier in the introduction Chapter 1

$$\lambda_{FB} = C_n \left(\frac{\kappa_V^3 \rho_V (\rho_L - \rho_V) |\mathbf{g}| (\psi + 0.4 c_{p,V} (T^I - T_{SAT}))}{D_V \mu_V (T^I - T_{SAT})} \right)^{0.25}, \quad (2.49)$$

where C_n is a constant equal of 0.62.

Then the vapour mass source term due to film boiling follows

$$\dot{m}_{FB,V} = \alpha_L \frac{\lambda_{FB} (T^I - T_{SAT}) A_B}{\psi V_B}, \quad (2.50)$$

where A_B/V_B stands for boundary cell face area over the boundary cell volume. The last calculated variable within film boiling HTR is the thermal turbulent diffusivity for each phase

$$\gamma_{tr,FB,j} = \frac{\lambda_{FB} (T^I - T_{SAT})}{\nabla_{\hat{\mathbf{n}}} h_j} - \gamma_{m,j}. \quad (2.51)$$

During the transition boiling HTR, the heat transfer q_{TB} is estimated using minimum heat flux q_{MHF} as correlated by Jeschar et al. [3]

$$q_{MHF} = 0.09 \rho_V \psi \left(\frac{\sigma}{|\mathbf{g}| (\rho_L - \rho_V)} \right)^{0.25} \left(\frac{|\mathbf{g}| (\rho_L - \rho_V)}{\rho_L + \rho_V} \right)^{0.5}. \quad (2.52)$$

Total critical heat flux $q_{CHF,t}$ is evaluated from the critical heat flux at saturation temperature $q_{CHF,SAT}$ by Zuber et al. [65] considering the water subcooling following Hua & Xu [66]

$$q_{CHF,SAT} = C_m \rho_V \psi \left(\sigma |\mathbf{g}| \frac{\rho_L - \rho_V}{\rho_V^2} \right)^{0.25}, \quad (2.53)$$

$$q_{CHF,t} = \left(1 + 0.345 \frac{Ja}{Pe^{0.25}} \right) q_{CHF,SAT}, \quad (2.54)$$

where $C_m = 0.131$ is the model coefficient. Ja and Pe stand for Jakob number and Péclet numbers

$$Ja = \rho_L c_{p,L} \frac{T_{SAT} - T_{int,L}}{\rho_V \psi}, \quad (2.55)$$

$$Pe = \frac{\sigma^{0.75}}{\gamma_{m,L} [g(\rho_L - \rho_V)]^{0.25} \rho_V^{0.5}}. \quad (2.56)$$

Heat flux during the transient boiling HTR is then

$$q_{TB} = k_{burn} q_{CHF,t} (1 - \theta) + k_{MHF} q_{MHF} \theta, \quad (2.57)$$

where k_{MHF} and k_{burn} are the minimum heat flux and the burnout factors equal to 5 and 0.5, respectively. The factors are used due to the lack of the correlations generality and need to be tuned to experiment [31]. θ represents an interpolation factor bounded by 0 and 1, found by employing the predefined temperatures T_{LEID} and T_{DNB} through

$$\theta = w_p \frac{T^I - T_{DNB}}{T_{LEID} - T_{DNB}}, \quad (2.58)$$

where $w_p = 1$ is a wetting parameter serving the same purpose as k_{MHF} and k_{burn} [31].

Having q_{TB} , vapour mass source and thermal turbulent diffusivity can be estimated

$$\dot{m}_{TB,V} = \alpha_L \frac{q_{TB}}{\psi} \frac{A_B}{V_B}, \quad (2.59)$$

$$\gamma_{tr,TB} = \frac{q_{TB}}{\nabla_{\hat{\mathbf{n}}} h_L}. \quad (2.60)$$

The third HTR to address is the nucleate boiling regime following the well-known

Kurul & Podowski model [40]

$$q_{NB} = q_{CV,L} + q_q + q_e, \quad (2.61)$$

where q_q and q_e are quenching and evaporation heat fluxes. At this stage, the quenching area fraction, which is necessary to partition the heat fluxes, is estimated by

$$A_2 = \min\left(\alpha_L \pi D_w^2 N \frac{Z}{4}, 1\right), \quad (2.62)$$

where $Z = 4$ and D_w stand for bubble area constant and bubble detachment diameter, respectively, with the latter calculated according to Tolubinsky and Kostanchuk [67]

$$D_w = \max(\min(D_{w,ref} e^{-(T_{SAT} - T_{int,L})/45}, D_{w,max}), D_{w,min}). \quad (2.63)$$

It is not related to the bubble diameter used for fluid phases' interfacial terms. Subscripts *ref*, *min* and *max* stand for reference, minimum and maximum wall detachment diameter of a bubble, respectively. $D_{w,ref} = 6e^{-4} m$, $D_{w,min} = 1e^{-6} m$ and $D_{w,max} = 0.0014 m$.

The nucleation site density N is estimated using the Lemmert and Chawla model [68] implemented by Egorov and Menter [69]

$$N = 992200 C_o \left(\frac{T^I - T_{SAT}}{10}\right)^{1.805}, \quad (2.64)$$

where $C_o = 1$.

The area fraction for convective heat transfer is defined as $A_1 = 1 - A_2$, and finally, the area fraction for evaporation utilizes a model proposed by Bowring [70]

$$A_{2E} = \min(\alpha_L \pi D_w^2 N, 5). \quad (2.65)$$

Now, the nucleate boiling mass source term can be evaluated

$$\dot{m}_{NB,V} = \frac{1}{6} A_{2E} D_w \rho_V f_w \frac{A_B}{V_B}, \quad (2.66)$$

where f_w is bubble detachment frequency estimated according to Cole [71]

$$f_w = \left(\frac{4|\mathbf{g}|(\rho_L - \rho_v)}{3D_w\rho_L} \right)^{1/2}. \quad (2.67)$$

Then, the evaporation heat flux follows a formula

$$q_e = \dot{m}_{NB,V}\psi \frac{1}{\alpha_L \frac{A_B}{V_B}}. \quad (2.68)$$

The quenching heat transfer coefficient is evaluated in the following manner

$$\lambda_q = 2\gamma_{m,L}c_{p,L}f_w \left(\frac{0.8}{f_w} \frac{\rho_L}{\pi\gamma_{m,L}} \right)^{1/2}, \quad (2.69)$$

while quenching heat flux according to the next relation

$$q_q = \frac{A_2}{\alpha_L} \lambda_q (T_I - T_{int,L}). \quad (2.70)$$

That finally leads to the calculation of the thermal turbulent diffusivity due to nucleate boiling

$$\gamma_{tr,NB} = A_1\gamma_{tr,CV,L} + \frac{q_q + q_e}{\nabla_{\hat{\mathbf{n}}} h_L}, \quad (2.71)$$

where $\gamma_{tr,CV,L}$ is the thermal turbulent diffusivity due to convective heat transfer into liquid [39]. The same variable is also used when only natural heat convection takes place.

To calculate convective heat transfer, firstly, the thickness of the viscous sub-layer $y_{vst,j}^+$, hence intersection of inertial sub-layer Eq. (2.43) and the viscous sub-layer equation

$$T_j^+ = Pr_j y_j^+, \quad (2.72)$$

is found employing the Newton-Raphson algorithm. After which equations based on

the boundary cell y^+ are applied

$$\gamma_{cv,eff,j}^i = \begin{cases} \frac{q_{CV,j}^{i-1} \rho_j u_{\tau,j} y}{q_j Pr_j y_j^+ + Pr_j 0.5 \rho_j u_{\tau,j} |\mathbf{u}_j^C - \mathbf{u}_j^I|^2} & y_j^+ < y_{vst,j}^+ \\ \frac{q_{CV,j}^{i-1} \rho_j u_{\tau,j} y}{q_j Pr_t (1/C_\kappa \ln(Ey_j^+) + P_j) + 0.5 \rho_j u_{\tau,j} (Pr_t |\mathbf{u}_j^C - \mathbf{u}_j^I|^2 + (Pr_j - Pr_t) u_{dc,j}^2)} & y_j^+ \geq y_{vst,j}^+ \end{cases} \quad (2.73)$$

where convective heat flux from previous iteration (superscript $i - 1$) is calculated using effective thermal turbulent diffusivity due to convection, yet using current specific enthalpy:

$$q_{CV,j}^{i-1} = \gamma_{CV,eff,j}^{i-1} \nabla_{\hat{\mathbf{n}}} h_j. \quad (2.74)$$

Difference between velocities at the viscous sub-layer thickness and the boundary is then found

$$u_{dc,j} = \frac{u_{\tau,j}}{C_\kappa} \ln(Ey_{vst,j}^+) - |\mathbf{u}_j^I|. \quad (2.75)$$

Finally, the thermal turbulent diffusivity due to convection is

$$\gamma_{tr,CV,j} = \gamma_{eff,j}^i - \gamma_{m,j} \quad (2.76)$$

Notice that Eqs. (2.43, 2.44, 2.45, 2.46) are not subscripted with j to improve readability. Nevertheless, to calculate thermal turbulence diffusivity due to convection, it is necessary to use the subscript, hence distinguish between the fluid phases.

2.4 Solid-fluid interfacial temperature

The current section describes the computation of the regions' interfacial temperature and the derivation of fluid temperature and Biot number, both later used to investigate computational results.

Perfect thermal contact and contact of all three phases, vapour, liquid and solid, is assumed at the solid-fluid interface. The contact area of fluid splits between vapour and liquid according to their volume fractions. With this in mind, the following two

rules are formulated

$$T^I = T_S^I = T_F^I = T_j^I = T_k^I, \quad (2.77)$$

$$q_S^I = -q_F^I, \quad (2.78)$$

where subscript F stands for fluid, a combination of vapour and liquid.

Assuming 1D heat transfer, Fourier's law, Newton's law of cooling and finally, the latent heat (wall boiling) impact included in the heat transfer coefficient λ , Eq. (2.78) is rewritten as

$$\kappa_S \frac{dT_S}{dx} = -\alpha_j \lambda_j dT_j - \alpha_k \lambda_k dT_k. \quad (2.79)$$

The heat transfer coefficient is defined as $\lambda_j = \frac{\kappa_{eff,j}}{\delta_j}$, where $\kappa_{eff,j}$ is the effective thermal conductivity formulated as $\kappa_{eff,j} = (\gamma_{tr,j} + \gamma_{m,j})c_{p,j}$, which complies with the definition of thermal diffusivity in prior sections. δ_j represents a distance between the boundary cell centre and the boundary face centre due to space discretisation (see Fig. 2.3). Besides, Eq. (2.77) is employed which leads to

$$\kappa_S \frac{1}{\delta_S} (T_S^C - T^I) = \alpha_j \kappa_{eff,j} \frac{1}{\delta_F} (T^I - T_j^C) + \alpha_k \kappa_{eff,k} \frac{1}{\delta_F} (T^I - T_k^C). \quad (2.80)$$

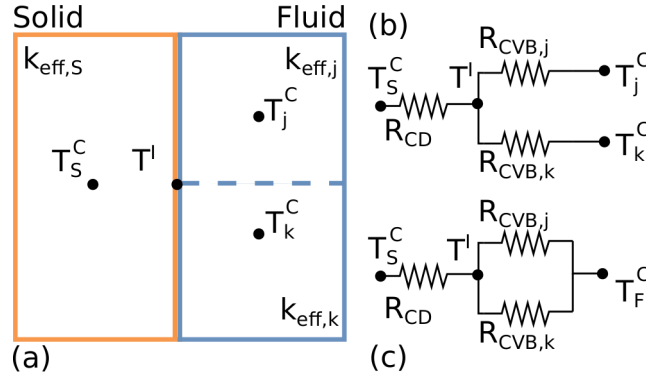


Figure 2.3: a) Interface mesh view; b) Partitioned heat transfer into liquid and vapour; c) Heat transfer into fluid. R represents thermal insulation and is defined by Eq. (2.82)

Further division by $\kappa_S \frac{1}{\delta_S}$ and simple manipulation reveals a formula for solid-fluid interface temperature as a function of the phase intensive Biot number Bi_j

$$T^I = \frac{T_S^C + Bi_j T_j^C + Bi_k T_k^C}{1 + Bi_j + Bi_k}, \quad (2.81)$$

where

$$Bi_j = \frac{\alpha_j \kappa_{eff,j} \delta_S}{\kappa_S \delta_F} = \frac{T_S^C - T^I}{T^I - T_j^C} - Bi_k \frac{T^I - T_k^C}{T^I - T_j^C} = \frac{R_{CD}}{R_{CVB,j}}, \quad (2.82)$$

and R stands for thermal insulance $R_{CD} = \delta_S/\kappa_S$ and $R_{CVB,j} = \delta_F/\alpha_j \kappa_{eff,j}$. The subscript CD represents conduction between solid-fluid interface and solid, and subscript CVB stands for convection between the interface and related fluid phase, though it also includes wall boiling heat transfer if present.

Once the phase intensive Biot number is derived, it is proposed to lump both fluid phases into a sole phase called fluid. To attain this aim, a situation, where the heat transfer from the solid-fluid interface to the fluid phases exhibits behaviour modelled by parallel heat transfer (conduction like) and the existence of fluid temperature T_F , is assumed (Fig. 2.3c). That can be compared with the previously analyzed case Fig. 2.3b, where two distinct temperatures T_j and T_k were considered. Writing equality of heat fluxes for both problems as follows

$$\frac{1}{R_{CD}}(T_S^C - T^I) = \frac{1}{R_{CVB,j}}(T^I - T_j^C) + \frac{1}{R_{CVB,k}}(T^I - T_k^C), \quad (2.83)$$

$$\frac{1}{R_{CD}}(T_S^C - T^I) = \frac{R_{CVB,j} + R_{CVB,k}}{R_{CVB,j} R_{CVB,k}}(T^I - T_F^C) \quad (2.84)$$

leads to the derivation of the fluid temperature T_F^C via substitution of Eq. (2.83) into Eq. (2.84), manipulation and utilization of Eq. (2.82)

$$T_F^C = \frac{Bi_j T_j^C + Bi_k T_k^C}{Bi_j + Bi_k} \quad (2.85)$$

Finally, rearranging of Eq. (2.84) allows expressing Bi_F

$$Bi_F = Bi_j + Bi_k = \frac{\kappa_{eff,F} \delta_S}{\kappa_S \delta_F} = \frac{T_S^C - T^I}{T^I - T_F^C} = \frac{R_{CD}}{R_{CVB,F}}, \quad (2.86)$$

where $\kappa_{eff,F} = \alpha_j \kappa_{eff,j} + \alpha_k \kappa_{eff,k}$

The above analysis can find practical implementations and be utilised in various ways, beyond boiling flows, depending on the circumstances. For example, one option is to use the fluid Biot number for deciding on numerical simulation stability limits

[37]. Throughout this research, the analysis outcomes are used to investigate the computational results and to reason their validity.

2.5 Solution algorithm

This section briefly describes the solution procedure, including the time step definition and coupling logic. Fig. 2.4 shows crucial steps of the solution algorithm. Within each time step (black colour), the regions' coupling loop is employed (magenta colour). That aims to converge results of each region solver and includes fluid solution loop (blue colour), solid solution loop (orange colour) and energy coupling loop (red colour). The fluid region is solved by the fluid solution loop, employing `reactingTwoPhaseEulerFoam`. In the first step, the vapour volume fraction transport equation (Eq. 2.14) is solved, and the liquid volume fraction is calculated. Then the construction of momentum matrices is followed by a fluid energy loop which solves the energy equations (Eq. 2.4). However, before that, the wall boiling is calculated (Section 2.3) to acquire thermal turbulent diffusivity and vapour mass source. Then, estimation of the solid-fluid interfacial temperature (Section 2.4) continues. Some codes perform an iteration procedure between the two last steps since the solid-fluid interfacial temperature is a function of thermal turbulent diffusivity and vice versa [54]. Nonetheless, that does not apply to the current code. Instead, the number of regions' coupling loops is increased to converge also the vapour volume fraction. Once the prescribed number of iterations for the fluid energy loop is fulfilled, the pressure matrix is constructed and solved, after which velocity is corrected using the newly calculated pressure. Finally, the turbulence (Eqs. 2.6, 2.7) is calculated, which evokes the wall boiling again. Notice that the author added the option to set up a number of fluid solution loops to have the possibility to converge only that region. It is not available in the original OpenFOAM code.

The solid solution loop is much simpler. Only the energy equation (Eq. 2.17) needs to be solved, which is preceded by calculating the solid-fluid interfacial temperature.

After finishing the solid solution loop, the algorithm proceeds to the energy coupling loop, which consists of fluid energy and solid energy loops. These are identical to the energy loops discussed before. That concludes the regions' coupling, and after a prescribed number of loops, the algorithm proceeds to the next time step if required.

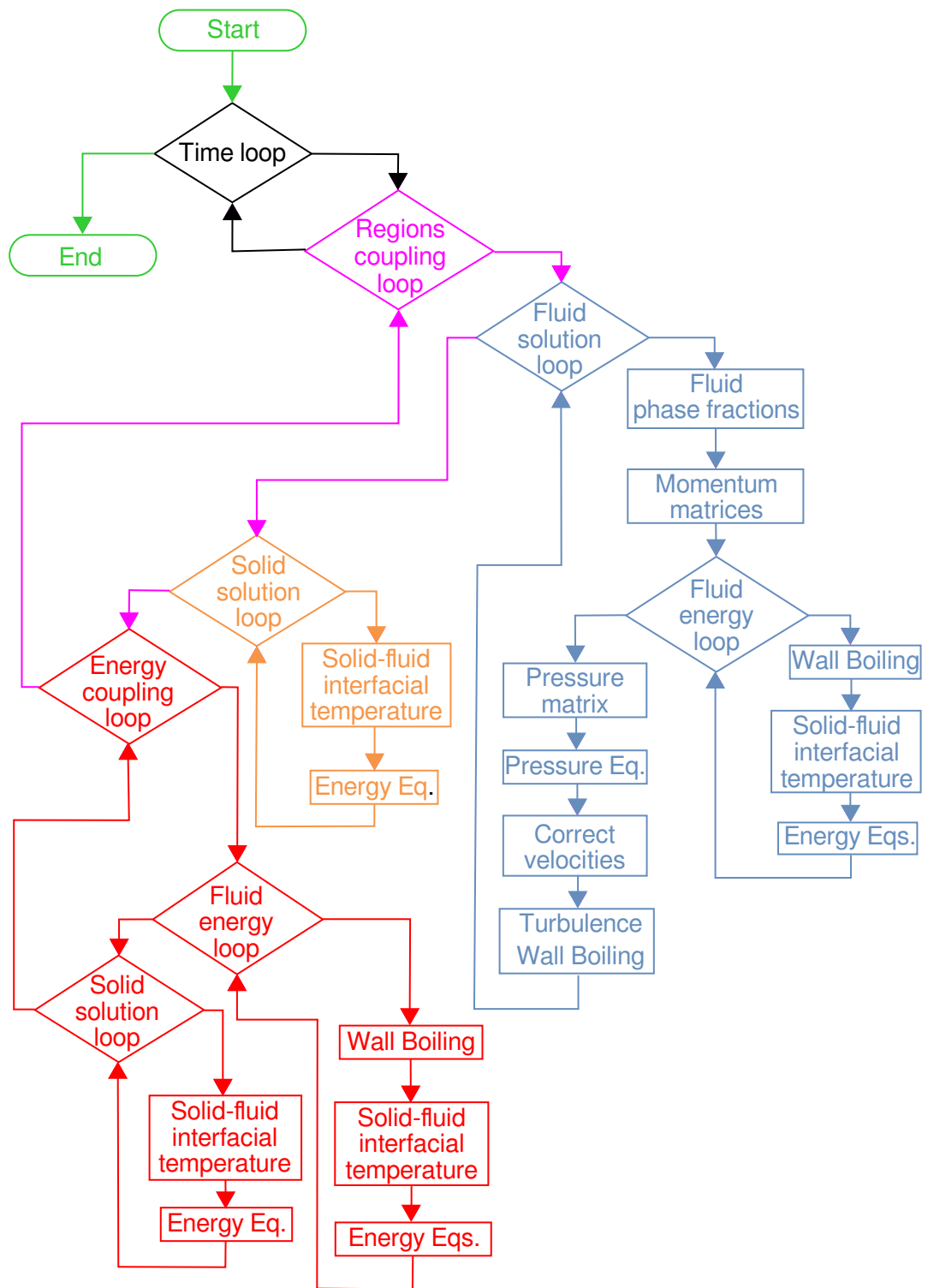


Figure 2.4: Solution algorithm

Another specific of the two region approach is the time step. In this case, the regions are not allowed to differ; hence, a common time step is determined using the following requirements. The time step is kept below 0.001 s, and the maximum Courant number CFL equals 0.5. The fluid region usually dictates the time step because it needs a significantly lower value than the solid. Nevertheless, a restriction arising from the solid Fourier number Fo is also accounted for. Therefore, its maximum value is limited to 0.5.

The general CFL number definition has the following formulation

$$CFL = \frac{\mathbf{u}\Delta t}{l}, \quad (2.87)$$

where l represents the cell size, but the current problem must account for two phases, liquid and vapour. Therefore, four different CFL numbers are formulated. The one restricting the time step the most is then used. The phase intensive CFL_j accounts for each phase separately

$$CFL_j = \frac{\alpha_j \mathbf{u}_j \Delta t}{l}. \quad (2.88)$$

The CFL_{tot} represents the total velocity

$$CFL_{tot} = \frac{(\alpha_L \mathbf{u}_L + \alpha_V \mathbf{u}_V) \Delta t}{l}, \quad (2.89)$$

and finally, CFL_r considers fluid phases relative velocity

$$CFL_r = \frac{(\alpha_L \mathbf{u}_L - \alpha_V \mathbf{u}_V) \Delta t}{l}. \quad (2.90)$$

The implementation of the CFL numbers in the OpenFOAM follows these definitions but using volumetric fluxes ϕ_{vf} over the faces of a particular cell. As an example, the phase intensive CFL_j can be seen

$$CFL_{\phi,j} = \frac{1}{2} \frac{\sum_f |\alpha_{j,f} \phi_{vf,j,f}| \Delta t}{V}, \quad (2.91)$$

where V is cell volume. The value 1/2 is present because the sum of fluxes magnitudes

is calculated over all cell faces. This way, double counting of the fluxes is avoided.

Finally, the Fourier number Fo (diffusion number) is defined by

$$Fo = \frac{\kappa_S}{c_{p,S}\rho_S l_S^2} \Delta t. \quad (2.92)$$

Notice that during this research, equation and field under-relaxations are avoided to decrease the number of variables potentially affecting the results. The only exceptions are simulations in Chapter 5 when IPC is allowed.

2.6 Numerical solvers and schemes

This section provides a brief overview of numerical solvers and schemes used during this research to complete the simulation setup.

Firstly, the numerical solvers are introduced (Table. 2.3). The solid region's enthalpy equation is solved using a Preconditioned Conjugate Gradient (*PCG*) solver for symmetric Lower, Diagonal and Upper (*LDU*) matrices using Simplified Diagonal-based Incomplete Cholesky preconditioner (*DIC*). On the other hand, fluid region enthalpy, momentum, and if solved turbulent kinetic energy and its dissipation rate, are solved with Preconditioned Bi-Conjugate Gradient Stabilized (*PBiCGStab*) solver for asymmetric LDU matrices with Simplified Diagonal-based Incomplete LU (*DILU*) preconditioner. Next, pressure is solved utilising the Geometric Agglomerated algebraic MultiGrid (*GAMG*) solver with a *DIC* or Gauss-Seidel smoother. Finally, a Multidimensional Universal Limiter for Explicit Solution (*MULES*) is employed to solve vapour volume fraction.

	Variable	BFS (Chap. 3)	Plate (Chap. 4)	Cylinder (Chap. 5)
Solid	h	PCG, DIC	PCG, DIC	PCG, DIC
	h, \mathbf{u}	PBiCGStab, DILU	PBiCGStab, DILU	PBiCGStab, DILU
Fluid	$k \epsilon$		PBiCGStab, DILU	PBiCGStab, DILU
	$p - \rho gh$	GAMG, DIC	GAMG, GaussSiedel	GAMG, GaussSiedel
	α	MULES	MULES	MULES

Table 2.3: Numerical solvers chosen for various variables and validation problems.

The description continues with numerical schemes (Table 2.4). Notice that the Gauss theorem is used for interpolation values from cell to face centres. Time is always discretised using Euler first-order implicit bounded scheme. Gradients are evaluated employing a central-differencing second-order interpolation scheme as well as the laplacian terms, yet these are eventually corrected for the mesh non-orthogonality. Finally, the convective terms estimation vary. Volume fraction always uses the vanLeer differencing scheme [72]. The rest uses either upwind or central-differencing schemes. The limitedLinear is a central-differencing scheme that limits to upwind where strong gradients appear. Limiting value one means the strongest limitation.

	Term	BFS (Chap. 3)	Plate (Chap. 4)	Cylinder (Chap. 5)
Solid	ddt	Euler	Euler	Euler
	grad	linear	linear	linear
	div			
	laplacian	linear orthogonal	linear corrected	linear corrected
Fluid	ddt	Euler	Euler	Euler
	grad	linear	linear	linear
	div α	vanLeer	vanLeer	vanLeer
	div \mathbf{u}	linear	upwind	upwind
	div h	limitedLinear 0	upwind	upwind
	div k, ϵ	upwind	upwind	upwind
	div K	limitedLinear 1	upwind	upwind
	laplacian	linear orthogonal	linear corrected	linear corrected

Table 2.4: Numerical schemes chosen for various terms and validation problems. Gauss theorem is used for values interpolation from cell centres to face centres.

2.7 ETF restriction for grid discretization

The topic of this section is an implication of the ETF method for mesh discretisation. Both fluid phases, vapour and liquid, can be viewed as dispersed and continuous phases. Nonetheless, the governing equations (Section 2.1) assume both phases to be continuous. Michaelides et al.[45] name the assumption for the dispersed phase the particle-phase continuum assumption. It follows that the particle (bubble/droplet) diameter must be smaller than the smallest dimension of a CoV the particle is present within, hence restricting the cell size:

$$D < \Delta x \tag{2.93}$$

This requirement is also apparent, recalling the point force approach's usage to account for the phase interaction. Fluid disturbances due to individual particles are

not resolved. Instead, their impact is modelled and applied within each CoV. The apparent conclusion is that there is a limit arising from particle size and CoV size ratio. The limit places restrictions on resolving the computational domain's geometrical features where the CoVs would have to be smaller than the existing particle. The matter, however, seems to be rarely discussed or followed in the literature [22, 24–26, 29–35, 54]. The reason might be the limit's forgiving behaviour and relation to the phase volume fraction. Violation of these restrictions does not necessarily lead to unphysical results. Also, numerical stability issues might not occur unless the breach is significant. Moreover, considering an error stemming from the usage of various interfacial correlations (models), the error due to the violation of this assumption can be negligible.

Comparing the bubble diameter of 3 *mm* with the plate thickness of 1.5 *mm* (Chapter 4) shows that the geometrical feature is smaller than the diameter. Nonetheless, it is essential to have at least one CoV across the plate thickness in the fluid region. It is to be noticed that no adverse effects of using this strategy were observed.

Finally, the application of the limit Eq. (2.93) must be judged by experience. Hence, a sufficient grid refinement must be allowed to describe the fluid dynamics while avoiding any stability issues due to not complying with the restriction.

2.8 Summary

This chapter gave the methodology overview, which covered governing equations including turbulence, fluid interfacial terms, wall boiling, description of solid-fluid interfacial temperature calculation, derivation of fluid temperature and Biot number, solution algorithm, ETF impact on the computational grid and numerical solvers and schemes. The content will help to explain the solver's behaviour and outline further development options.

Chapter 3

Backward-facing step conjugate heat transfer

Using a backward-facing step (BFS) problem with conjugate heat transfer into single-phase fluid without phase change, this chapter discusses the current methodology and is an initial validation of the proposed computational approach. More specifically, the accuracy of the fluid dynamics solver as well as of the conjugate heat transfer are examined. The same approach was used to validate an alternative solver developed by the author within OpenFOAM-5.0 and presented in [73]. Nevertheless, the wall boiling boundary condition was still under development during that time. Thus the code was ready for the validation against the BFS problem with conjugate heat transfer, yet not for transition and film boiling, which are examined in the following chapters. Meanwhile, OpenCFD released a more refined solver capable of describing physics during immersion quenching. After a careful comparison of the codes developed by the author in OF-5.0 and the one by OpenCFD, the research work migrated to the official release to take advantage of the new capabilities and have access to a broader audience of users and developers. Therefore the results in Kamenicky et al. [73] have to be recalculated with the new solver. In this chapter, the latest results are shown and compared against the work presented in the following articles [74–77].

BFS is a well-studied problem [78], and numerous papers have been dedicated to experimental, theoretical, and numerical investigation of the hydrodynamics characteristics [78]. They analysed a wide range of Reynolds numbers, expansion ratios between

the inlet channel and the channel downstream of the step together with other geometrical features, particles, etc [74–76, 78–89] and, also effects of heat transfer came under consideration [77, 78, 90–96]. Here the work performed by Ramšak [77] investigating conjugate heat transfer is used to validate the current computational approach, and more specifically, the parts of the solver concerning the fluid dynamics and conjugate heat transfer. Research by Kanna & Das [91] is not used. Teruel & Fogliatto [94] and Ramšak [77] found considerable discrepancies in Nusselt number and temperature at the regions' interface compared to Kanna & Das [91]. That is, however, in contrast with Seddig et al. [95], who obtained a good agreement with them for another set of conditions while validating their solver employing the lattice-Boltzmann method. Professor Kanna finally stated, in communication with Ramšak [77], that their results might be faulty. The results presented in this research agree with Ramšak [77]. The Teruel & Fogliatto [94] article is not used for validation because different Reynolds and Prandtl numbers as well as solid height are used. Also, the provided data are few compared to the chosen article for validation [77].

3.1 Geometry, mesh, initial and boundary conditions

The BFS problem is described using Fig. 3.1. The computational domain is two-dimensional and divided into two regions, fluid at the top and solid at the bottom. The bottom of the solid is heated, and the fluid inlet is directly above the step. The inlet and the step span over half of the fluid channel height, and the domain length is 30 times the channel's height. The solid height is four times the inlet.

The flow enters at the left top over the backward-facing step at $Re_{BFS} = 800$ and $Pr = 0.71$. The Reynolds number is defined by

$$Re_{BFS} = \frac{\rho \bar{\mathbf{u}}_{in} 2b}{\mu}, \quad (3.1)$$

where $\bar{\mathbf{u}}_{in}$ is an average of the inlet velocity \mathbf{u}_{in} defined in Table 3.1, and $2b$ is the channel height equal to 1 m . Prandtl number follows the usual definition Eq. (2.39), only neglecting the c subscript. The flow is laminar with a parabolic velocity profile at the inlet (Table 3.1). No gravity is applied; hence no buoyance forces are considered.

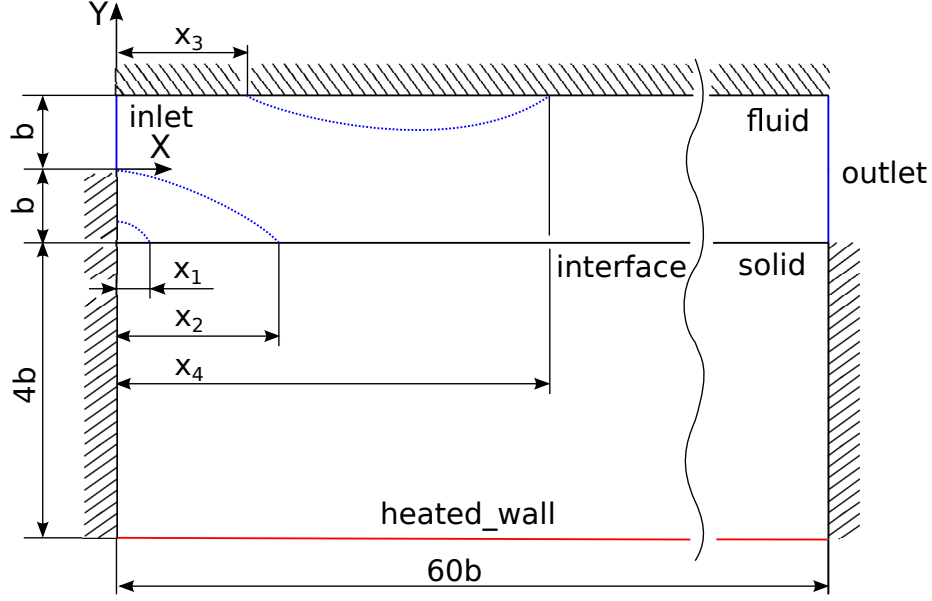


Figure 3.1: Computational domain with dimensions, boundary conditions names and vortices locations.

Due to these fluid governing conditions, three vortices develop. Firstly, the secondary vortex at the bottom corner, just after the step. Its reattachment point is labelled by x_1 . Secondly, the primary bottom vortex of which the reattachment point is located using x_2 . Finally, the top vortex occurs inversely at the top of the fluid domain. Measuring in the x -direction, the flow separates slightly before the end of the primary bottom vortex.

Notice that in the previous research [74–77, 91, 94, 95], the fluid is always one-phase. Nonetheless, in this work, two sets of Navier-Stokes equations to describe two-phase fluid are employed (Section 2.1.1). To replicate the original problem, both fluid phases are assumed to be identical. Hence their physical properties, boundary conditions and initial conditions are the same. Moreover, the volume fractions are prescribed equal to 0.5, and fluid phases' interactions (Section 2.2) are neglected. In this manner, the same results should be acquired. Further on, in this chapter, the terminology will not differentiate between the fluid phases.

Boundary conditions are summarised in Table 3.1. Φ is a non-dimensionalised temperature according to

$$\Phi = \frac{T - T_{in}}{T_{heat} - T_{in}}, \quad (3.2)$$

where T is the actual temperature at a particular location in either region and T_{in} is the fluid temperature at the inlet, thus the lowest temperature in the domain. T_{heat} is the temperature of the heated wall, the highest temperature in the domain. Inlet velocity boundary profile is parabolic, and its temperature Φ is constant and equal 0. Outlet velocity BC is defined using zero normal gradients for both velocity and temperature Φ . Except for the heated wall, all walls are defined as a no-slip BC and adiabatic. The heated wall is described using constant temperature $\Phi = 1$ and also no-slip. The regions' interface employs the conjugate heat transfer BC defined in Section 2.4. The initial temperatures are 0 and 1 for fluid and solid, respectively. Further, the terms temperature and non-dimensionalised temperature Φ are interchangeable in this chapter.

	Velocity	Temperature
Inlet	$u_x = -24y^2 + 12y$ $u_y = 0$	$\Phi = 0$
Outlet	$\nabla_{\hat{n}} \mathbf{u} = 0$	$\nabla_{\hat{n}} \Phi = 0$
Wall	no slip	$\nabla_{\hat{n}} \Phi = 0$
Heated wall	no slip	$\Phi = 1$
Interface	no slip	Section 2.4

Table 3.1: Boundary conditions following the naming convention from Fig. 3.1

The domain is discretised in space using hexahedra with identical side lengths. Even though it is a 2D problem, the third direction is necessary for OpenFOAM, so the elements have thickness. Also, the mesh elements have identical dimensions in both regions. Thus meshes at the interface are conformal, boundary cells' centres are at the same distance from the interface and grow ratio is not applied. Four cubic meshes with an increasing number of elements are employed, where each element consists of 8 mesh points with a constant side length as shown in Table 3.2. Each side of an element is

split by two in the subsequent refinement, leading to a strict mesh convergence study.

Mesh element side length [mm]	Total number of elements
50.00	36,000
25.00	144,000
12.50	576,000
6.25	2,304,000

Table 3.2: Meshes characteristics for backward-facing step problem

3.2 Validation variables and convergence criteria

In order to present the code capabilities, it has been decided to validate hydrodynamic and thermodynamic indicators for multiple cases varying the regional conductivity ratio:

$$\kappa_{ra} = \frac{\kappa_S}{\kappa_F}, \quad (3.3)$$

which evaluates to 1, 10, 100 and 1000, to configure four different circumstances.

The research is concentrated on the validation investigating vortices separation and reattachment points, velocity and temperature profiles at various channel cross-sections and temperature and Nusselt number (Nu) at the regions' interface. The space coordinate values are non-dimensionalised, dividing the particular coordinate by the inlet height b .

The local Nu is calculated using the following formula:

$$Nu = -\nabla_{\hat{n}} \Phi_F|_{interface}. \quad (3.4)$$

The average Nusselt number \overline{Nu} is evaluated as an integral of the local Nu at the interface divided by its length L :

$$\overline{Nu} = \frac{1}{L} \int_0^L Nu dx. \quad (3.5)$$

The separation and reattachment points are determined by finding termination points of zero surface contours at the wall retrieved from the fluid streamwise velocity component [97].

Even-though, the BFS problem has a steady-state solution [75, 77, 91, 94], governing equations with temporal terms have been used (Section 2.1) to solve the problem. That implies the necessity to define a time step. Therefore maximum Courant and solid Fourier numbers (Eq. 2.87, 2.92) are prescribed in the current investigation. Notice, however, that if the time step should be the same for all conductivity ratios, other properties/variables must be altered together with the region conductivity. Otherwise, the Fourier number changes and the time step may be affected. Consequently, solid region conductivity along with solid thermal heat capacity is altered.

The time convergence for all tracked variables is monitored, computing time residual ω at the ten-second range:

$$\omega_{10} = \frac{|\chi_{t+10} - \chi_t|}{\chi_t}, \quad (3.6)$$

where any hydrodynamic or thermodynamic variable substitutes χ .

Finally, error values *err* are calculated using Ramšak computational results [77], acquired using previously validated BEM in-house code [77, 98, 99]. They performed hydrodynamic validation using backward-facing step and flow passing a cylinder [98], heat diffusion in the intricate fractal geometry of the Koch snowflake [99] and conjugate heat transfer with Couette flow against its analytical solution [77]. The validation results (VR) used for the current project computational approach are calculated using Richardson extrapolation to zero mesh size and are verified against the third party code CFX [77]. The following equation is the utilised formula

$$err = 100 \frac{|\chi_t - \chi_{t, vr}|}{\chi_{t, vr}}, \quad (3.7)$$

where subscript *vr* stands for the validation results [77]. The computed errors slightly differ from Ramšak [77] even for his own results. That is because the errors are calculated using numbers with decimal places shown, in comparison with Ramšak, who rounded values after computation of the errors solely for visualisation.

3.3 Time and mesh convergence

To validate the computational steady-state results, convergence must be reached in time as well as space [74–77, 91]. That is not assessed only according to Eq. (3.6) but also qualitatively using velocity and temperature profiles at various locations.

Fig. 3.2 depicts hydrodynamic results in the initial part of the backward-facing step channel. Moreover, the red lines show zero contours of the streamwise velocity component, which are used to determine the separation and reattachment points [97]. The black dashed lines visualise two locations where the profiles are obtained to judge the convergence. The third location is not shown, but it is further downstream at $x/b = 30$. The data are converged in time as it will be seen later (Fig. 3.5, 3.6). Fig. 3.2a, b, c, d show velocity streamlines for all meshes. Based on the first observation, it is concluded that all the meshes predict the primary bottom vortex and top vortex qualitatively well. Nevertheless, a detailed examination (Fig. 3.2e, f, g, h) reveals that the coarsest mesh does not capture the secondary bottom vortex expected immediately behind the step. Thus, this qualitative hydrodynamic comparison already disqualifies the coarsest mesh. Also, the shapes of the zero velocity contours change with refinement, yet this is minimal.

Continuing with the hydrodynamic mesh convergence, plotting velocity profiles (Fig. 3.3) demonstrate excellent convergence for the streamwise velocity component and very good convergence for the normal component. Once again, the coarsest mesh can be disqualified. Its flow direction in the y -axis is opposite to the rest. It results from an improper prediction of vortices length. The coarse mesh predicts the end of the bottom primary and top vortices shifted nearer to the inlet compared to finer meshes (Fig. 3.2). Thus the flow already starts to develop a channel velocity profile. The other three meshes (with elements size 25.00 mm , 12.50 mm and 6.25 mm) demonstrate a perfect convergence. The velocity profiles are also investigated at the location $x/b = 30$ (Fig. 3.4). Again, the streamwise component is converged perfectly, and the normal component likewise demonstrate a clear convergence trend.

The time convergence of the velocity profiles is presented in Fig. 3.5 and 3.6. The convergence is sufficient, yet more time is required for the normal velocity compared to the streamwise one closer to the inlet. Satisfactory results are reached at about

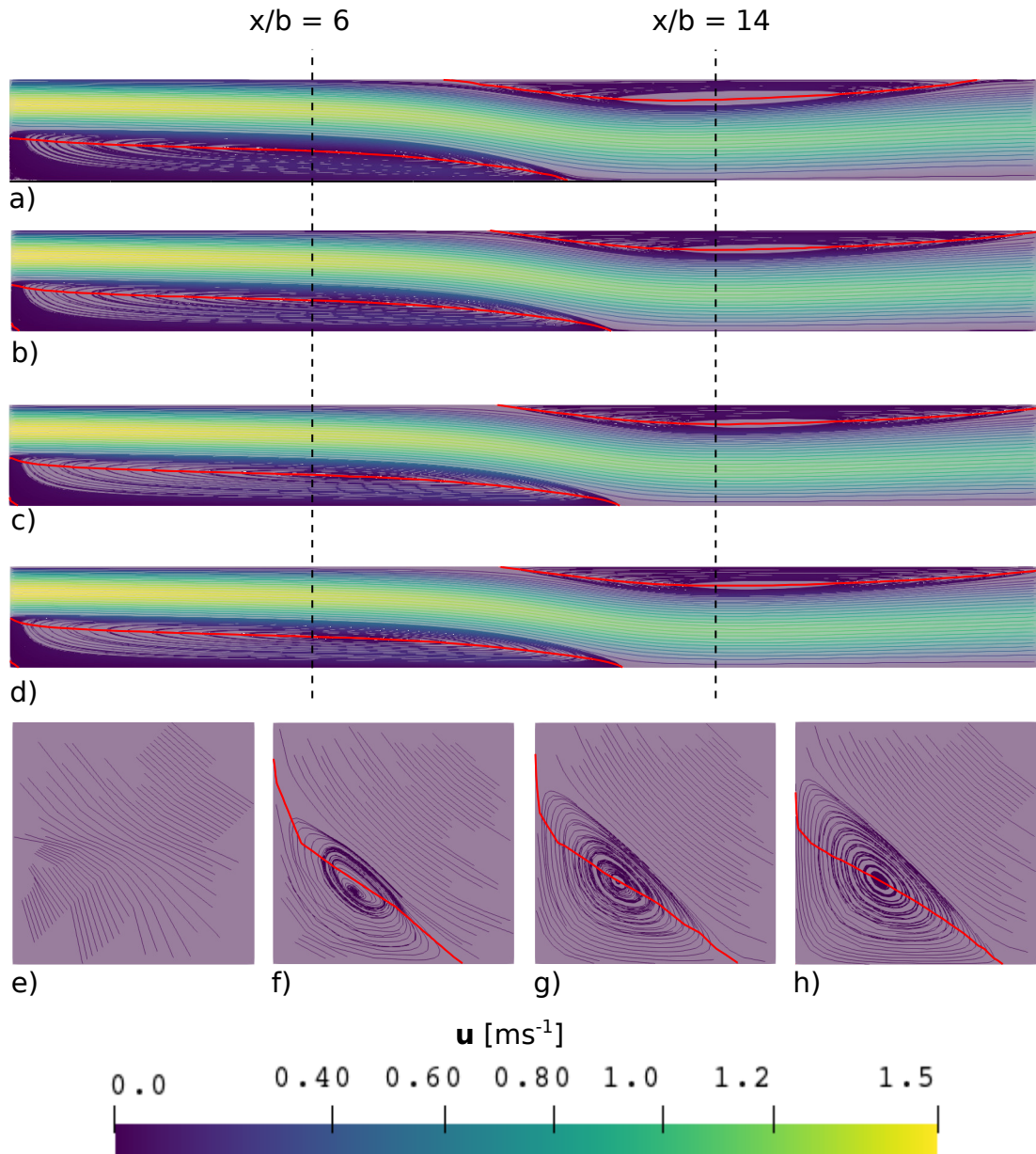


Figure 3.2: Velocity streamlines visualising vortices in the fluid region at 500 s. The domain is not shown in full length. Computational mesh with element sizes a) 50.00 mm, b) 25.00 mm, c) 12.50 mm and d) 6.25 mm, respectively. Bottom left corner for computational mesh with element sizes e) 50.00 mm, f) 25.00 mm, g) 12.50 mm and h) 6.25 mm, respectively.

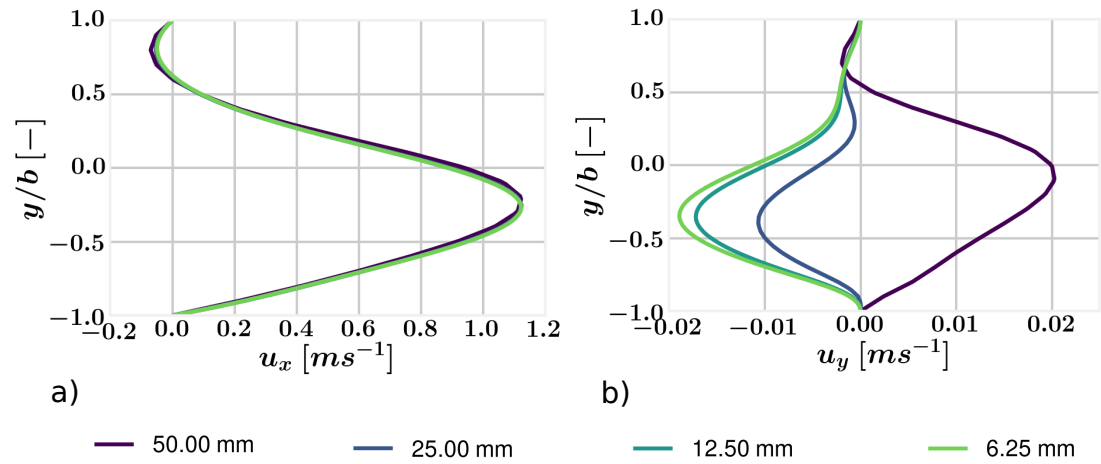


Figure 3.3: Velocity profiles of the a) streamwise and b) normal components at $x/b = 14$ and $500 s$ using various meshes.

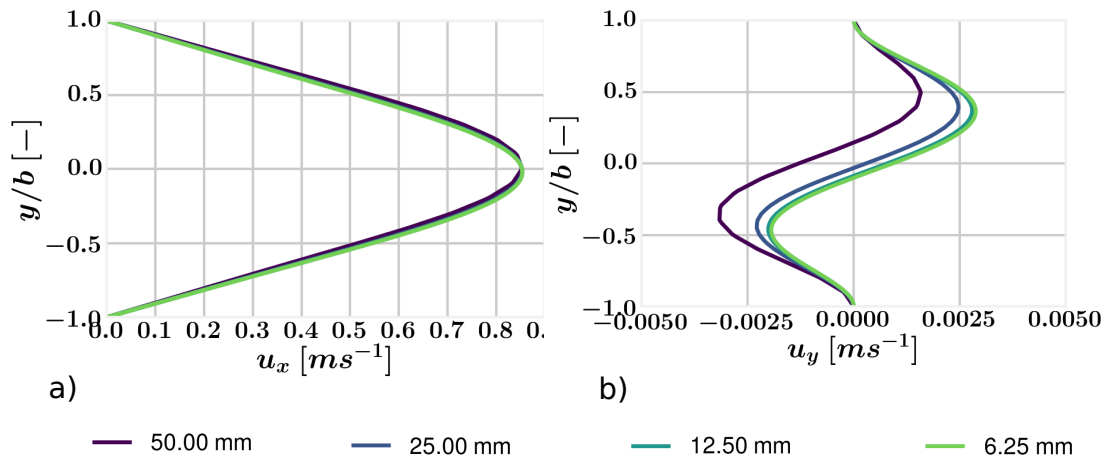


Figure 3.4: Velocity profiles of the a) streamwise and b) normal components at $x/b = 30$ and $500 s$ using various meshes.

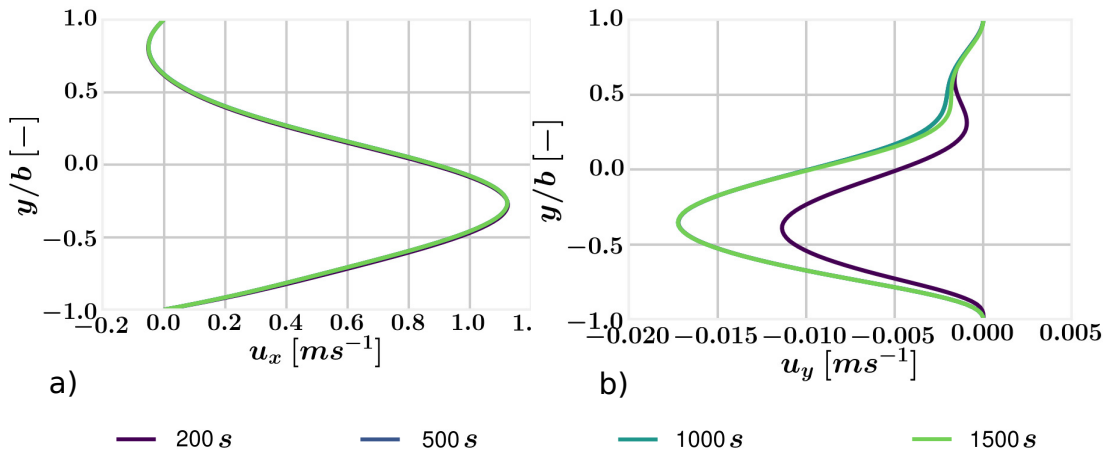


Figure 3.5: Velocity profiles of the a) streamwise and b) normal components at $x/b = 14$ at various times using the computational mesh with element size 12.50 mm.

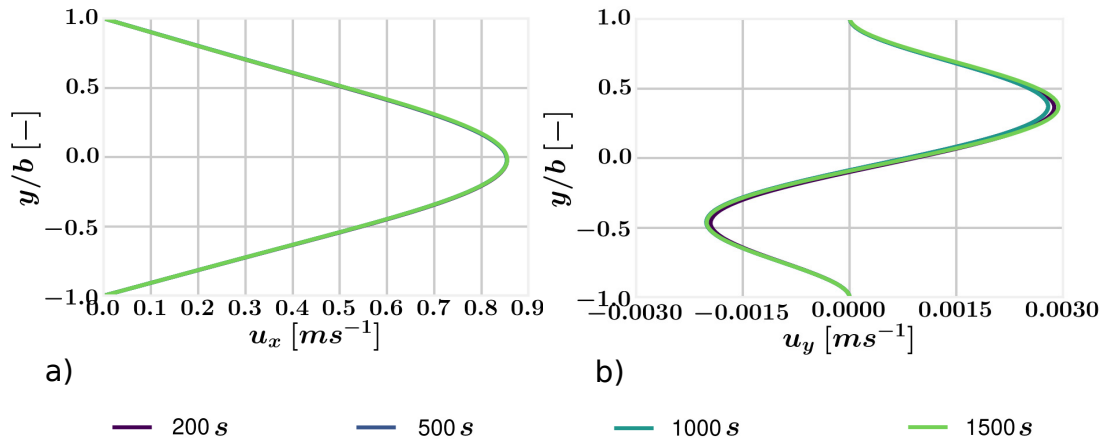


Figure 3.6: Velocity profiles of the a) streamwise and b) normal components at $x/b = 30$ at various times using the computational mesh with element size 12.50 mm.

500 s. Thus, the observed hydrodynamic characteristics are considered converged for a computational mesh with element size of 12.50 mm or smaller beyond 500 s.

Once the hydrodynamic characteristics have been discussed, it is time to focus on thermodynamics. Firstly, the temperature contours for $\kappa_{ra} = 1$ are presented in Fig. 3.7. Notice that the data are plotted both for fluid and solid regions, where fluid ranges between $y/b = -1$ and $y/b = 1$. That allows visualising one of the key convergence indicators, the continuity of the white contours across the regions' interface ($y/b = -1$). Proceeding from the coarsest mesh to more refined, from Fig. 3.7a to c, the contours approach each other and eventually starts to match. It is also evident that the contours tend to be more continuous near the channel beginning. The finest

mesh with the element size 6.25 mm is not used because it is very time-demanding and hydrodynamic convergence has been achieved with the 12.50 mm element size mesh. As will be seen later, thermodynamic time convergence might require substantially longer computations than hydrodynamic characteristics (Fig. 3.9, 3.10, 3.11).

Further attention is given to the mesh convergence of the temperature profiles at $x/b = 6$, $x/b = 14$ and $x/b = 30$ (Fig. 3.8). These results are displayed for the conductivity ratio κ_{ra} equal to 1 at 1500 s . It is apparent that they are not influenced by mesh refinement. Thus, it is concluded that the mesh convergence is very good. The temperature contours and profiles vary depending on the conductivity ratio, and the least trivial configuration is displayed here. The differences caused by the conductivity ratio will be discussed later in this chapter.

Finally, the time convergence of the temperature profiles at various locations (Fig. 3.9, 3.10, 3.11) is brought to the attention. The temperature field tends to converge significantly faster for a larger conductivity ratio ($\kappa_{ra} = 1000$). In such a case, the convergence time of the solid approaches to that of fluid. Moreover, the solid temperature can be considered uniform compared to the fluid region where a substantial gradient exists. Qualitative convergence is then reached even at 200 s as opposed to $\kappa_{ra} = 1$, which converges to steady-state much later.

To understand the temperature profiles more in-depth, it is beneficial to mention the relation between κ_{ra} and Bi defined by Eq. (2.86), which reduces to $\frac{1}{\kappa_{ra}}$, when $\delta_F = \delta_S$, $\alpha_j = \alpha_k$ and $\gamma_{tr,j} = \gamma_{tr,k} = 0$ (laminar flow). This observation concludes that the lower the conductivity ratio, the higher the Biot fluid number. Therefore a different setup may lead to different computational stiffness, potentially resulting in numerical instabilities at the regions' interface [37, 42, 43]. Also, a lower Biot number means higher importance of the fluid temperature gradient compared with solid and so the option to neglect the impact of the solid region, suggesting the potential use of the so-called lumped-capacitance method [100].

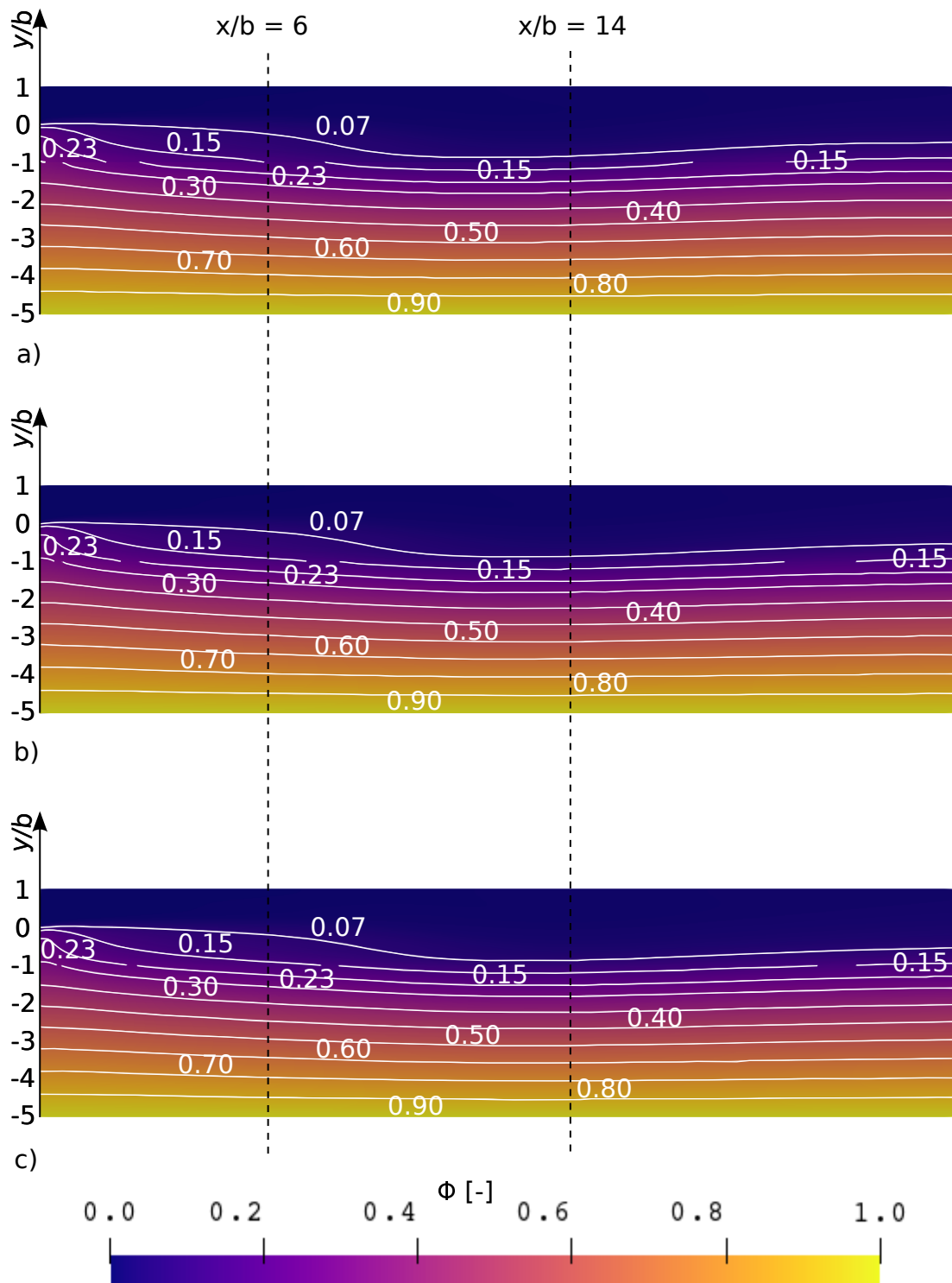


Figure 3.7: Non-dimensional temperature contours for various computational meshes at 1500 s and conductivity ratio $\kappa_{ra} = 1$. a) Computational mesh with element size 50.00 mm; b) Computational mesh with element size 25.00 mm; c) Computational mesh with element size 12.50 mm.

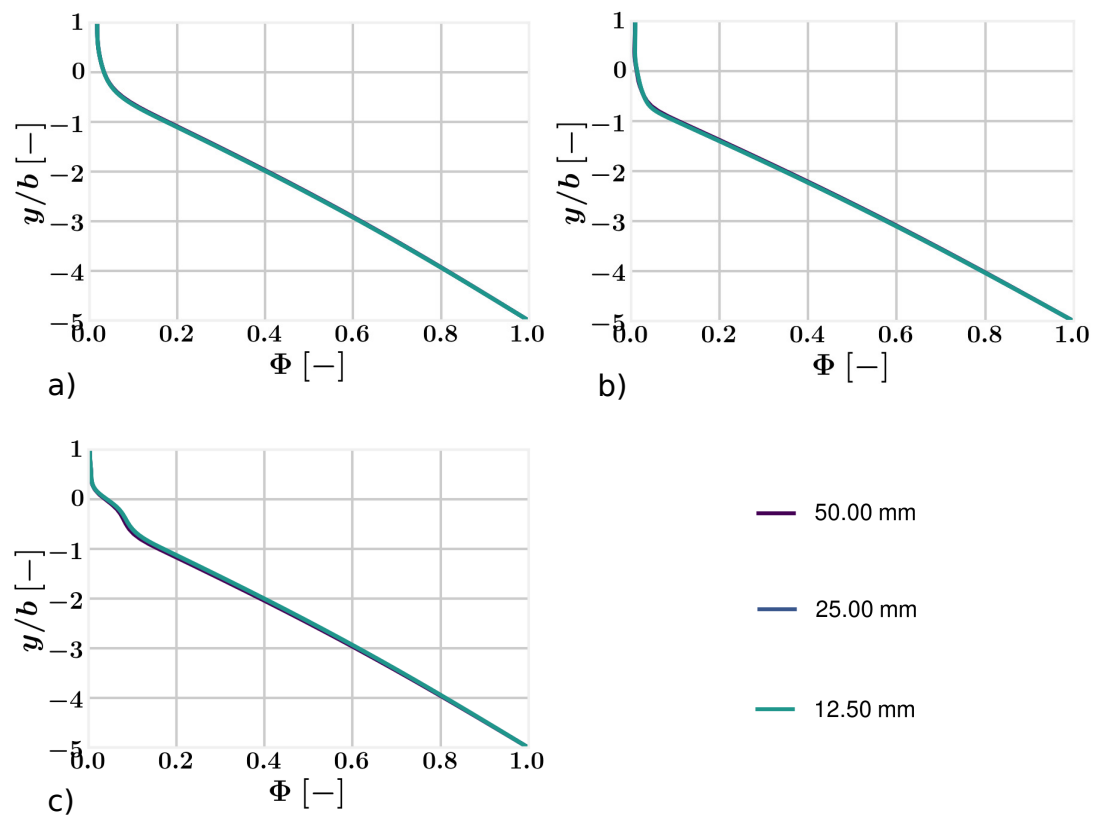


Figure 3.8: Non-dimensionalised temperature profiles for various computational meshes at 1500 s and conductivity ratio $\kappa_{ra} = 1$. a) $x/b = 6$; b) $x/b = 14$; c) $x/b = 30$.

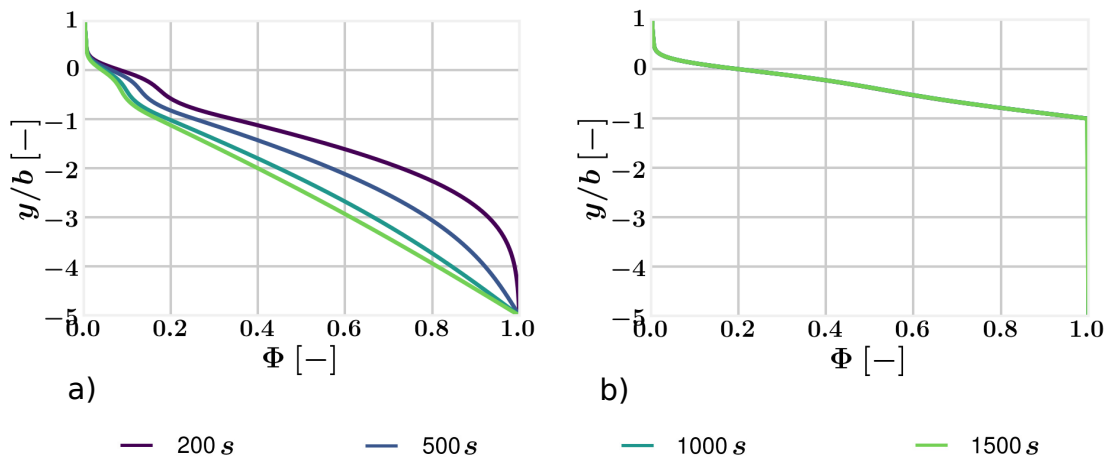


Figure 3.9: Non-dimensionalised temperature profiles at $x/b = 6$ at various times using computational mesh with element size $12.50 m$. a) $\kappa_{ra} = 1$; b) $\kappa_{ra} = 1000$.

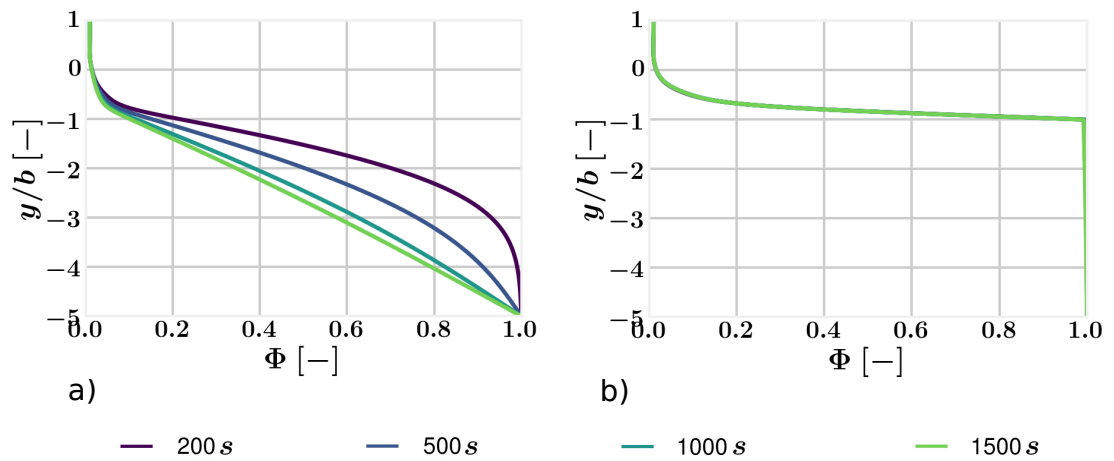


Figure 3.10: Non-dimensionalised temperature profiles at $x/b = 14$ at various times using computational mesh with element size $12.50 m$. a) $\kappa_{ra} = 1$; b) $\kappa_{ra} = 1000$.

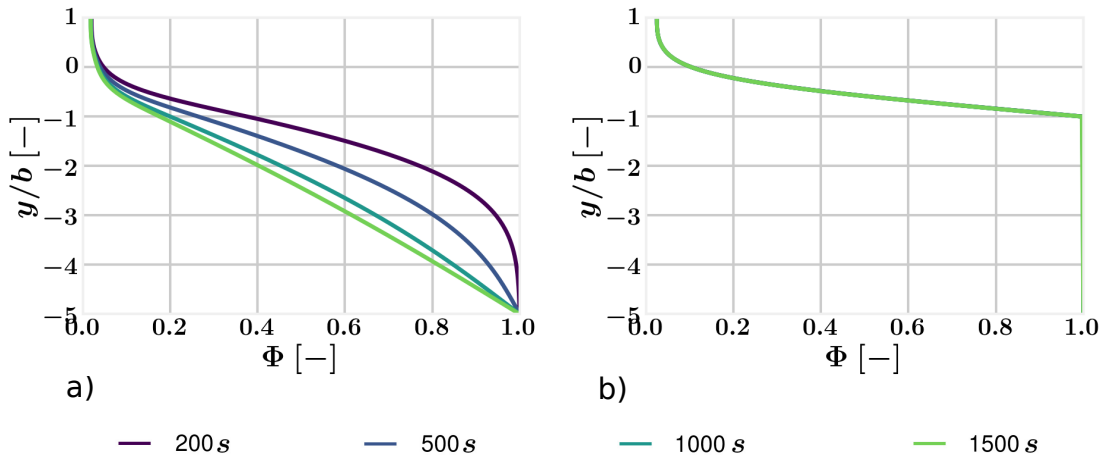


Figure 3.11: Non-dimensionalised temperature profiles at $x/b = 30$ at various times using computational mesh with element size 12.50 m . a) $\kappa_{ra} = 1$; b) $\kappa_{ra} = 1000$.

Throughout this chapter, instability affecting all conductivity ratios has been observed. Once the computations approach steady-state, a numerical noise in volume fraction begins to propagate and may eventually affect momentum and energy variables. This behaviour can be suppressed by time step reduction, which, however, raises the overall time requirements. The cost increases, especially for the lower conductivity ratios. Therefore, in order to avoid excessive computational times, the mesh with element size 25 mm has been chosen for further computations within this chapter. It is a reasonable trade-off considering accuracy and time requirements. The mesh still allows good quality results and CFL equal to 0.08 .

3.4 Results, validation and discussion

This section compares computed results with solutions by Gartling [74], Gresho et al. [75], Grigoriev et al. [76] and Ramšak [77]. Gartling [74] employed the finite element method within NACHOS II [101] and FIDAP [102]. Gresho et al. [75] verified the existence of a steady-state hydrodynamic solution for BFS at a given physical configuration using various formulations and numerical approaches. Grigoriev et al. [76] validated their in-house code based on the Boundary Element Method (BEM) using the BFS problem. Finally, Ramšak [77] utilised an in-house multidomain BEM code with stream function-vorticity formulation and CFX from ANSYS to study conjugate heat transfer for a BFS. Notice that all results produced by the author for

validation are labelled by OpenFOAM (OF).

To begin, the comparison of hydrodynamic variables is given in Table 3.3. It shows the recirculation region lengths x_1 , x_2 , x_3 , x_4 non-dimensionalised by using the inlet height b . The data are extracted using the mesh with element size 25.00 mm at 1500 s , although very similar values are observable by 500 s . The maximum error difference between these two time points is 0.01 %. In general, the agreement with the VR is good for all variables except the reattachment point of the bottom secondary vortex, which has 7.65 % error. If the computational mesh with element size 12.50 mm were used, the error would decrease to 0.59 %. Similarly, errors for the other variables would be reduced. It is also worth noticing that the hydrodynamic solution is independent of the regions' conductivity ratio [77], which is confirmed by the simulations performed along with this study.

	x_1/b (err [%])	x_2/b (err [%])	x_3/b (err [%])	x_4/h (err [%])	$\omega_{10s,max}$
Ramšak [77] - VR	0.17	12.18	9.70	20.98	
OF	0.175 (7.65)	11.947 (1.91)	9.464 (2.43)	20.641 (1.62)	5.351 10^{-6}
Ramšak [77] - BEM	0.173 (1.76)	12.201 (0.17)	9.720 (0.21)	20.959 (0.05)	
Ramšak [77] - CFX	0.17 (0.00)	12.10 (0.66)	9.63 (0.72)	20.96 (0.10)	
Gratling [74]		12.20 (0.16)	9.70 (0.00)	20.96 (0.10)	
Grigoriev [76]		12.18 (0.00)	9.70 (0.00)	20.94 (0.19)	
Gresho [75]		12.20 (0.16)	9.72 (0.21)	20.98 (0.00)	

Table 3.3: Comparison of backward-facing step vortices' detachment and reattachment points with Ramšak [77] using a computational mesh with element size 25.00 mm at 1500 s .

Further, the attention is turned to thermodynamics. Tables 3.4, 3.5, 3.6, 3.7 present the average Nusselt number (Eq. 3.5) and locations and values of minimum temperature and maximum Nusselt number at the regions' interface. All data are displayed for a mesh with element size 25.00 mm yet at various times. In the case of Tables 3.4 and 3.5,

the results at 2500 s and 2000 s are used, respectively. On the other hand, Tables 3.6 and 3.7 show data acquired at 1500 s . This difference is caused by the conductivity ratios (Fig. 3.9, 3.10, 3.11). The time residual decreases with its increase. Thus, as aforementioned, higher conductivity ratios converge quicker in time. For example, if data at 1500 s would be used in Table 3.4, instead of at 2500 s , the largest error and time residual would be 22.22 % and $1.784 \cdot 10^{-3}$, respectively. At the same time, the highest error and time residual for $\kappa_{ra} = 1000$ at 1500 s is 3.11% and $2.360 \cdot 10^{-5}$ (Table 3.7). Thus, Tables 3.4, 3.5, 3.6, 3.7 clearly show that cases with conductivity ratios 1 and 10 would benefit from even a longer time computed. That however, might be very time-demanding as the time step would need to decrease to keep numerical stability (Section 3.3).

Now, comparing the thermodynamical variables with the Ramšak results [77], it is concluded that the results are excellent for conductivity ratios 100 and 1000, with the highest error being 3.11 %, which appears for the location of the minimum temperature. In comparison, results acquired with conductivity ratios 1 and 10 have the most prominent errors, 13.58 % and 8.28 %, respectively. Both are calculated for the minimum temperature values. Based on the research that the author performed, the magnitudes of the thermodynamic variables are more sensitive to the convergence time compared to the locations which are rather sensitive to mesh refinement. Thus, to decrease specific errors, different strategies can be chosen. That being said, each has its limitations.

	\overline{Nu} (err)	Φ_{min} (err)	x/b (err)	Nu_{max} (err)	x/b (err)	$\omega_{10s,max}$
Ramšak [77] - VR	0.425	0.081	12.76	0.465	12.88	
OF	0.427 (0.47)	0.092 (13.58)	12.425 (2.63)	0.470 (1.08)	11.525 (10.52)	$3.038 \cdot 10^{-4}$
Ramšak [77] - CFX	0.425 (0.00)	0.082 (1.23)	12.710 (0.39)	0.470 (1.08)	12.800 (0.62)	

Table 3.4: Comparison of interface thermodynamical variables with Ramšak [77] for $\kappa_{ra} = 1$ and mesh with element size 25.00 mm at 2500 s .

	\overline{Nu} (err)	Φ_{min} (err)	x/b (err)	Nu_{max} (err)	x/b (err)	$\omega_{10s,max}$
Ramšak [77] - VR	1.793	0.459	12.750	3.050	12.26	
OF	1.878 (4.74)	0.497 (8.28)	12.475 (2.16)	3.262 (6.95)	11.975 (2.32)	$7.096 \cdot 10^{-4}$
Ramšak [77] - CFX	1.792 (0.06)	0.458 (0.22)	12.670 (0.63)	3.081 (1.02)	12.200 (0.49)	

Table 3.5: Comparison of interface thermodynamical variables with Ramšak [77] for $\kappa_{ra} = 10$ and mesh with element size 25.00 mm at 2000 s.

	\overline{Nu} (err)	Φ_{min} (err)	x/b (err)	Nu_{max} (err)	x/b (err)	$\omega_{10s,max}$
Ramšak [77] - VR	2.602	0.894	12.720	6.581	12.360	
OF	2.590 (0.46)	0.919 (2.80)	12.325 (3.11)	6.759 (2.70)	12.125 (1.90)	$2.201 \cdot 10^{-4}$
Ramšak [77] - CFX	2.601 (0.04)	0.894 (0.00)	12.650 (0.55)	6.668 (1.32)	12.270 (0.73)	

Table 3.6: Comparison of interface thermodynamical variables with Ramšak [77] for $\kappa_{ra} = 100$ and mesh with element size 25.00 mm at 1500 s.

	\overline{Nu} (err)	Φ_{min} (err)	x/b (err)	Nu_{max} (err)	x/b (err)	$\omega_{10s,max}$
Ramšak [77] - VR	2.722	0.988	12.720	7.381	12.380	
OF	2.672 (1.84)	0.991 (0.30)	12.325 (3.11)	7.390 (0.12)	12.125 (2.06)	$2.360 \cdot 10^{-5}$
Ramšak [77] - CFX	2.721 (0.04)	0.988 (0.00)	12.620 (0.79)	7.485 (1.41)	12.270 (0.89)	

Table 3.7: Comparison of interface thermodynamical variables with Ramšak [77] for $\kappa_{ra} = 1000$ and mesh with element size 25.00 mm at 1500 s.

In the following, Nusselt number and non-dimensional temperature along the regions' interface are compared with the VR (Fig. 3.12, 3.13, 3.14, 3.15). The data are acquired at the exact times and meshes as Tables 3.4, 3.5, 3.6, 3.7. The interface temperature is in very good agreement with the VR for all conductivity ratios but with increasing temperature error downstream the channel. The Nusselt number results fit excellently to the VR.

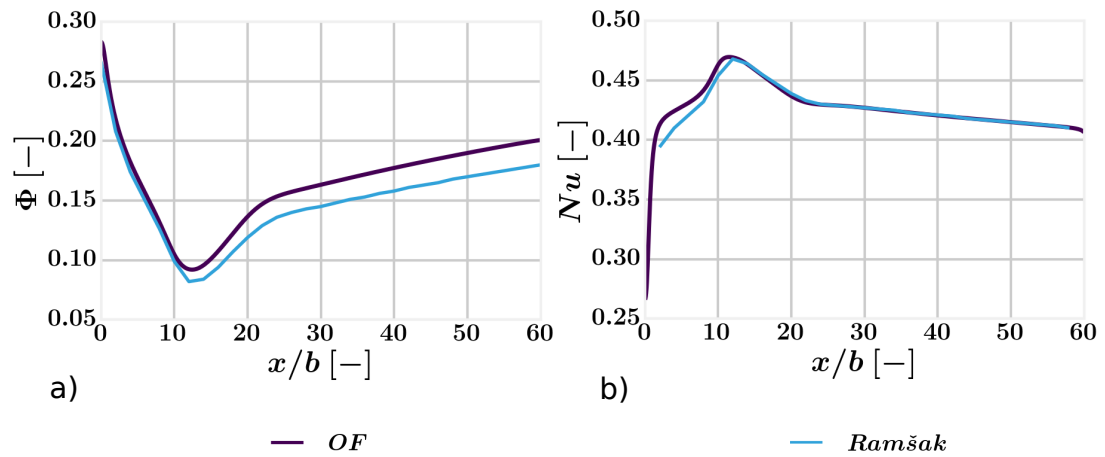


Figure 3.12: Comparison of non-dimensional temperature and Nusselt number profiles at the regions' interface with Ramšak VR [77] for $\kappa_{ra} = 1$ at 2500 s using a computational mesh with element size 25.00 mm. a) Non-dimensionalised temperature; b) Nusselt number

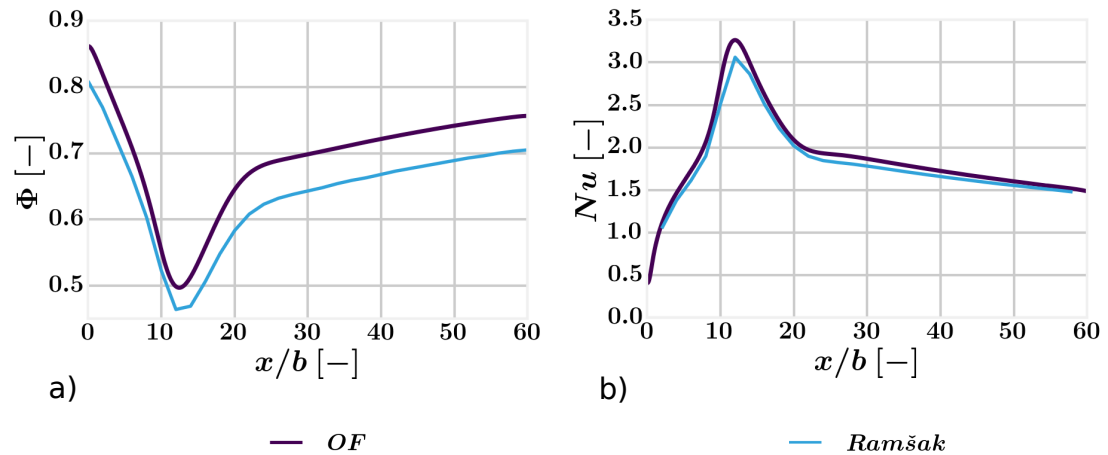


Figure 3.13: Comparison of non-dimensional temperature and Nusselt number profiles at the regions' interface with Ramšak VR [77] for $\kappa_{ra} = 10$ at 2000 s using a computational mesh with element size 25.00 mm. a) Non-dimensionalised temperature; b) Nusselt number

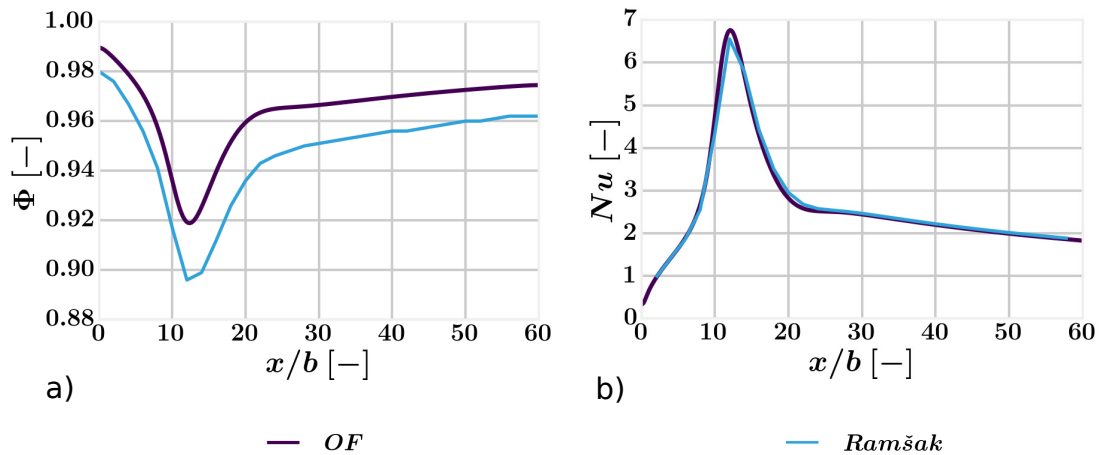


Figure 3.14: Comparison of non-dimensional temperature and Nusselt number profiles at the regions' interface with Ramšak VR [77] for $\kappa_{ra} = 100$ at 1500 s using a computational mesh with element size 25.00 mm. a) Non-dimensionalised temperature; b) Nusselt number

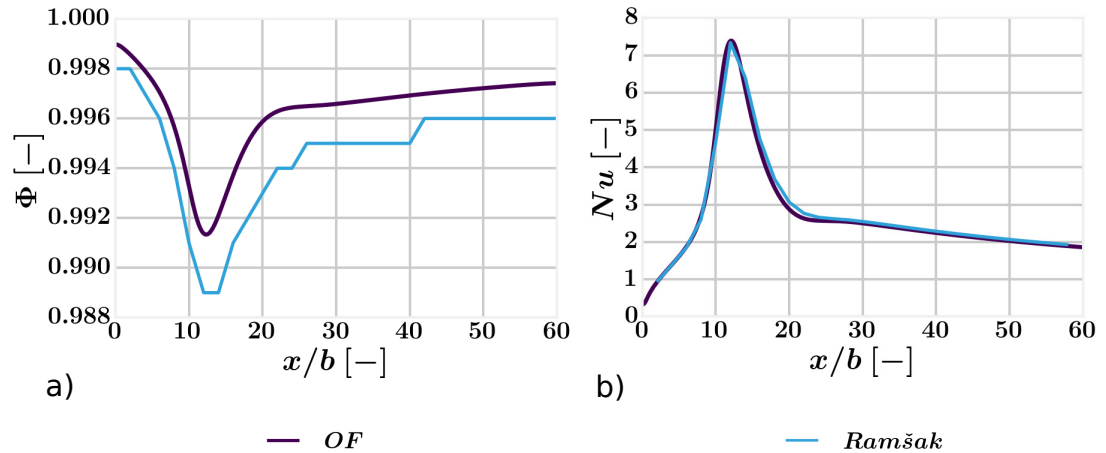


Figure 3.15: Comparison of non-dimensional temperature and Nusselt number profiles at the regions' interface with Ramšak VR [77] for $\kappa_{ra} = 1000$ at 1500 s using a computational mesh with element size 25.00 mm. a) Non-dimensionalised temperature; b) Nusselt number

Focusing on physics, correct behaviour is apparent. The temperature at the interface rises with the conductivity ratio as the temperature gradient within the solid decreases due to smaller thermal resistance. That leads to more uniform interface temperature and higher Nusselt number values, hence temperature gradient within the fluid. The same conclusion can be reached comparing various conductivity ratios in Fig. 3.16. Isotherms within the solid region ($y/b \in < -5, -1 >$) become more uniform as the conductivity ratio rises. Additionally, the fluid always has the highest temperature right behind the step where recirculation takes place, and the largest tem-

perature gradient is around the primary bottom vortex reattachment point. Beyond this location, the thermal boundary layer develops. Finally, it is obvious that the solid initial temperature field is almost identical to the steady-state results with a growing conductivity ratio. In contrast, lowering the ratio leads to more significant discrepancies and, therefore, longer convergence time. Following the description in Section 3.2, the solid thermal diffusivity is not altered with the change in the conductivity ratio.

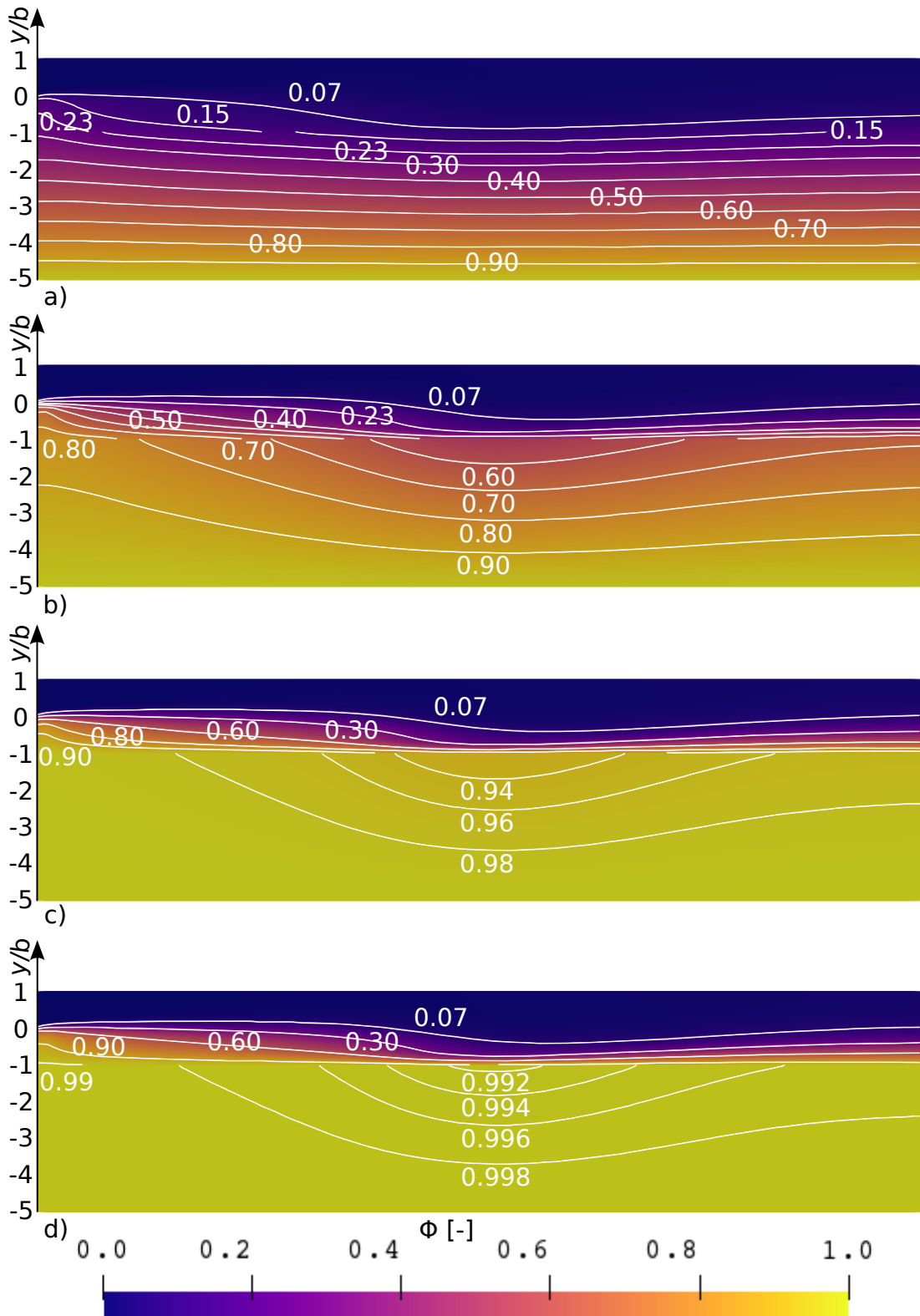


Figure 3.16: Non-dimensional temperature contours for various conductivity ratios and times, acquired using the mesh with element size 25.00 mm. a) $\kappa_{ra} = 1$ at 2500 s; b) $\kappa_{ra} = 10$ at 2000 s; c) $\kappa_{ra} = 100$ at 1500 s; d) $\kappa_{ra} = 1000$ at 1500 s.

Finally, information concerning the computational cost for this type of problem is discussed. For the configuration, $\kappa_{ra} = 1000$ and mesh with 25 mm element size, four Intel Xeon Gold 6138 (Skylake) processors @2.0 GHz on a single node with 40 cores were used. One node has access to 192 GB RAM, hence 4.8 GB per core. The elapsed cores time to reach 1500 s with maximum $CFL = 0.08$ was 131,531 s. Notice that two regions' coupling, one fluid solution, one fluid energy, one pressure corrector and one solid solution loops were used (Fig. 2.4).

3.5 Summary

This numerical study was a necessary step toward immersion quenching and had two aims. Firstly, to address the validation of the computational methodology, including the conjugated heat transfer approach mentioned in Section 2.4, and secondly, to prove that VR problems intended for single-phase flows could be applied to validate two-phase solvers. Fulfilling the goals, it has been shown that the code is capable of predicting laminar fluid flow at a backward-facing step with excellent accuracy (maximum error 0.59 %). Besides, it has also been validated for several thermodynamic variables gaining importance due to conjugate heat transfer. Acquired results and their precision depends on the conductivity ratio. The maximum errors are 13.58 %, 8.28 %, 3.11 % and 3.11 %, for $\kappa_{ra} = 1, 10, 100$ and 1000, respectively. Despite high errors for low conductivity ratios, clear mesh and time convergence, and good qualitative agreement with validation data have been confirmed. Therefore the current chapter work is crucial for Chapters 4, 5 as it helps to isolate potential issues to the boiling boundary condition in conjunction with the mesh rather than to methodology validated in this chapter. The results could be improved by prolonging the computational time, yet the convergence to a steady-state using transient governing equations is nontrivial. The reason is stability which requires lowering the time step resulting in high computational demand. Further, it seems that the magnitudes of interface thermodynamic variables are more sensitive to time convergence while their locations to mesh refinement.

Future work should focus on understanding the problem of numerical stability. Alternatively, there would be an option to run a test case where two fluid phases are used, yet one is very dominant. Finally, more such simple problems should be found

to provide further information about the methodology behaviour, avoiding potential issues in more complex cases.

Chapter 4

Plate quenching

After validating single-phase conjugate heat transfer (Chapter 3), attention is drawn to boiling conjugate heat transfer. Computational results are acquired using the approach described in Chapter 2. In addition, the previously derived fluid temperature and Biot number (Section 2.4) are employed here in order to judge the computational results, develop setup guidance and highlight any procedural drawbacks. Finally, the computational approach is validated against published experimental and numerical results of a thin plate at 880 °C horizontally submerged in water at high subcooling [36], where the dominant HTR is film boiling. This work is an intermediate step towards immersion quenching of more complex geometries and has been published in [103].

4.1 Experiment description and analysis

The experiment introduced by Khalloufi et al. [36] aims for water immersion quenching of thin horizontally oriented plate, of which properties resemble Inconel 718 (Table 4.1). Nonetheless, the material name is not provided. The quenched specimen's initial temperature is 880 °C and the coolant is at 25 °C and not agitated. Moreover, the provided data do not exhibit the effect of immersion. The plate dimensions are $75 \times 75 \times 1.5 \text{ mm}^3$ (Fig. 4.1).

A thermocouple measuring temperature used for validation in the Section 4.3 is placed in the specimen centre. That is assumed to reflect the solid-fluid interface temperature due to the plate's small thickness of 1.5 mm. The experimental as well

as numerical results are depicted in Fig. 4.1 [36]. It is apparent that the temperature rate does not vary substantially throughout the experiment; hence the HTR does not change either, and the film boiling has the prevailing effect. Nonetheless, seeing the computational results from this doctoral research project, corners and edges of the plate experience a whole range of HTRs. The numerical results, provided by Khalloufi et al. [36] (Fig. 4.1), fit the experiment quite well with a notable difference from about 15 s onwards.

These provided data and relative simplicity of the problem due to the dominant impact of only film boiling HTR makes an excellent problem to analyse the solver's behaviour and serve as an important validation step towards more complicated simulations.

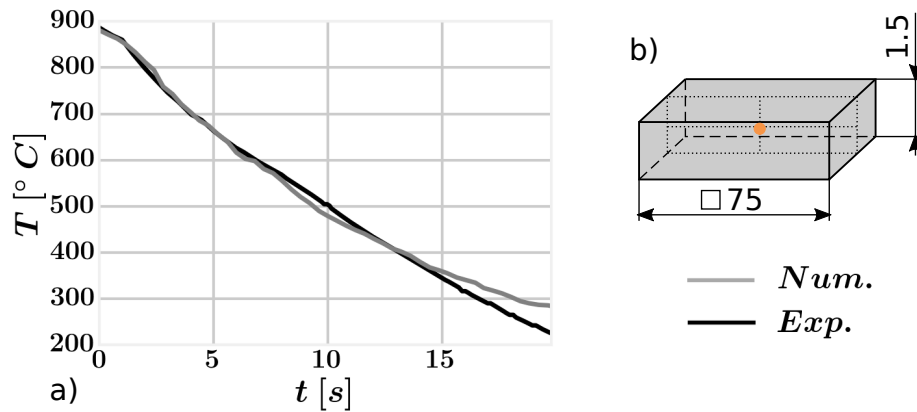


Figure 4.1: a) Numerical and experimental cooling curves obtained at the flat plate centre provided by [36]. b) Quenched specimen dimensions and thermocouple location (orange dot).

4.2 Geometry, mesh and boundary conditions

The computational domain consists of a tank filled with water up to three-quarters of its height (Fig. 4.2). Vapour (air) occupies the volume above the water surface, and both fluid phases are initially still. Agitation is not used, so any fluid movements are driven only via density differences and the interactions between the various phases. The heated sample is located in the centre of the computational domain.

The physical properties of all three phases used for simulations follow Khalloufi et al. [36] except for the vapour density, which is subject to the ideal gas law instead of being a constant value as in the original work [36]. The properties summary is provided

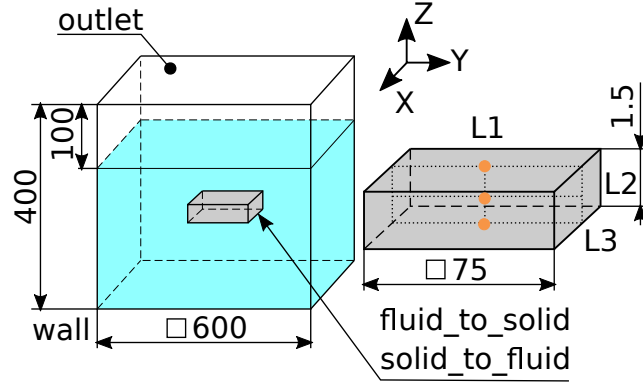


Figure 4.2: Computational domain with dimensions, boundary conditions names and investigated locations on the sample marked using orange dots. L1 - Above the plate centre at the solid-fluid interface; L2 - Plate centre; L3 - Beneath the plate centre at the solid-fluid interface.

in Table 4.1.

	κ [$W/(mK)$]	c_p [$J/(kgK)$]	ρ [kg/m^3]	μ [$Pa\ s$]
solid	11.4	435	8000	-
liquid	0.6	4,185	1000	0.001
vapour	0.025	2010	$\rho(p, T)$	0.000012

Table 4.1: Physical properties of water, vapour and the plate specimen.

Fig. 4.2 visualises all four boundary conditions and their names. The quenching tank bounding the computational domain represents a *wall*, and at the top is an *outlet*. The solid-fluid interface encloses the sample. That can either be the solid region *solid_to_fluid* or the fluid region *fluid_to_solid* boundary condition.

Table 4.2 defines some of the necessary variables boundary conditions. The temperature boundary conditions at both sides of the solid-fluid interface follow the description in Section 2.4. A simplification emerges assuming $T_L^I = T_V^I$, which allows estimating only one of the two and then setting the other at an equivalent value.

For the outlet patch, the velocity treatment depends on the flow direction. A zero gradient boundary condition is applied when the flow is positive, meaning the vapour/liquid leaves the domain. On the other hand, when an inflow is experienced, the velocity boundary condition is calculated from the boundary condition face normal

component of boundary cell mass flux. However, water cannot enter the domain as its volume fraction for inflow is set to zero. Thus, only vapour (air) can enter. Finally, the description of the boundary condition for thermal turbulence diffusivity (wall boiling) at the solid-fluid interface matches the description in Section 2.3.

	$\mathbf{u}_j [\frac{m}{s}]$	$T_L [^\circ C]$	$T_V [^\circ C]$	$T_S [^\circ C]$
wall	noSlip	25	25	-
outlet $\phi_{mf,n,j} > 0$	$\nabla_{\hat{\mathbf{n}}} \mathbf{u}_j = 0$	$\nabla_{\hat{\mathbf{n}}} T_L = 0$	$\nabla_{\hat{\mathbf{n}}} T_V = 0$	-
outlet $\phi_{mf,n,j} \leq 0$	$\frac{\phi_{mf,j}}{\rho_j A_B} \hat{\mathbf{n}}$	25	25	-
fluid_to_solid	noSlip	T_V^I	Section 2.4	-
solid_to_fluid	-	-	-	Section 2.4

Table 4.2: Horizontal plate boundary conditions. $\phi_{mf,n,j}$ stands for mass flux through a boundary cell face.

The computational grid is hexahedral and block-structured with a locus on the plate's horizontal surfaces. Several meshes, with varying refinement and labelled with the variable x_n [mm], which represents the boundary cell size in the normal direction to the solid-fluid interface, are used. The goal is, alongside the methodology validation, to study the significance of this type of refinement due to its impact on the wall mass source terms via Eqs. (2.50, 2.59, 2.66) and consequently on the whole computation. Results (Section 4.3) are displayed only for x_n related to the fluid region. The solid region grid refinement causes no significant behaviour anomaly and converges with four cells across the plate thickness. A summary of the mesh characteristics is given in Table 4.3. The regions' meshes are always conformal at the top and bottom surface to avoid interpolation errors. Exceptions are plate sides where only one fluid cell is used. The interpolation procedure follows the Arbitrary Mesh Interface (AMI) approach [104]. During the mesh generation, an advantage of the growth ratio is frequently taken. Its value is always around 1.1, never exceeding it.

	No el.	x_n [mm]
Fluid	27,950	20.0
	40,842	15.0
	57,094	10.0
	123,800	5.0
	219,475	3.1
	278,625	1.5
	367,350	0.375
	422,275	0.1875
Solid	900	0.375

Table 4.3: Fluid and solid regions' meshes characteristics, mentioning the total number of elements, and boundary cells interface perpendicular dimension x_n identical at the specimen top and bottom.

4.3 Results and discussion

This section aims to discuss validation results, indicate best practices for obtaining good quality results, and highlight solver weaknesses to motivate further development. A wide range of data acquired at three locations, including those shown in Fig. 4.2, is presented. Nevertheless, only experimental temperature measurements and numerical results at the specimen centre are available for validation. Therefore, the other two locations are used solely for analysis without comparison to the literature. Simulations always run for 19.8 s, which is the duration of the experiment used for validation [36]. Markers are often used to distinguish curves in figures. Notice, however, that these do not display all available data points.

To begin, a comparison of various fluid meshes, without IPC, as assumed previously in the literature [22, 24–26, 29–35] is given. Fig. 4.3a depicts cooling curves at location $L2$ (Fig. 4.2). This first observation reveals that results converge for mesh configurations with $x_n \geq 3.1$ mm. These are also in excellent consensus with the numerical results by Khalloufi et al. [36]. However, as the mesh is further refined, a considerably lower cooling rate emerge for meshes with $x_n \leq 0.375$ mm. At the same time,

$x_n = 0.1875 \text{ mm}$ causes faster cooling than $x_n = 0.375 \text{ mm}$. When a time range of 17-19.8 s (Fig. 4.3b) is brought into focus, more moderate cooling at about 18.2 s is witnessed for the mesh $x_n = 1.5 \text{ mm}$, which potentially leads to a significant shift of T_{LEID} in time and misprediction of the cooling behaviour. Thus, mesh $x_n = 1.5 \text{ mm}$ seems to be a limiting one between the converged meshes and the rest. The reasons for the change in cooling rate and strategy for avoiding it are given in the following paragraphs.

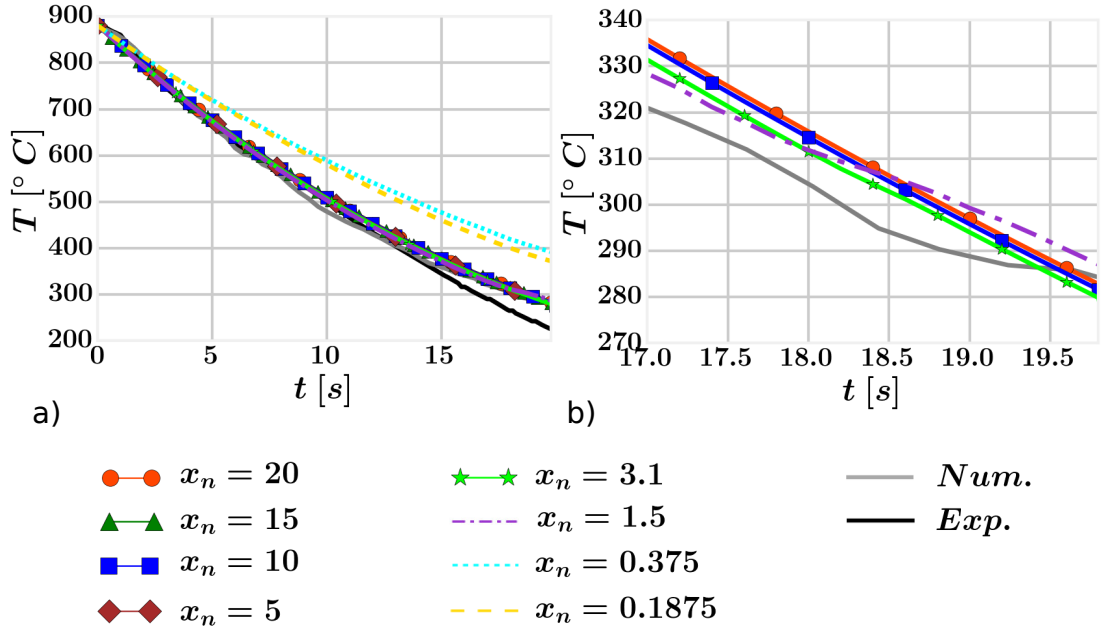


Figure 4.3: Cooling curves acquired at the location $L2$ in the solid region using various fluid meshes. The interfacial phase change is not activated. Numerical and experimental validation data are taken from Khalloufi et al. [36]. a) Global view with validation data; b) Focused view to a time range 17-19.8 s omitting results for $x_n = 15$; 5; 0.375; 0.1875, and the experimental results.

Investigation into the vapour volume fraction at $L1$ Fig. 4.4a and $L3$ Fig. 4.4b (the nearest locations to $L2$, where this data can be acquired) can provide some clues. Regardless of the location, the vapour volume fraction grows with the mesh refinement. The trend is even more visible at the bottom side of the plate, where vapour is more restricted from movement than at the top surface. While the vapour volume fraction reaches the maximum for meshes with $x_n \leq 0.375 \text{ mm}$ at $L3$, a considerable jump appears between the two and the other meshes at $L1$. That results from vapour isolation and heat diversion from the bottom to the top surface. Recalling the temperature re-

sults in Fig. 4.3a, it is evident that the cooling curves for meshes with $x_n \geq 3.1 \text{ mm}$ do not change even though the volume fraction does. That can only be when the total heat flux from a particular location does not change. Indeed, meshes with $x_n \leq 1.5 \text{ mm}$ experience significant drops in the heat flux from the solid-fluid interface into the fluid at the location $L3$ and a substantial increase at location $L1$. Nevertheless, the increased heat transfer does not compensate for the reduction at the bottom plate surface, and the solid region temperature decrease becomes more moderate.

The step increase in the vapour volume fraction, starting from about 17 s, appears due to the HTRs change. It has a limited effect on the measured cooling curve at $L2$, yet a crucial impact on the surrounding and influences the volume fraction at $L1$ and $L3$. It is also vital for the temperature gradient throughout the solid domain, but no experimental data are available.

The volume fraction is not necessarily mesh independent because the wall boiling mass source is applied within boundary cells only. That leads to increased vapour volume fraction with decreased boundary cell volume if the source term is constant. Nonetheless, the mass source is a function of volume fraction, making it also mesh dependent. Physically, the vapour layer at the wall is refined with decreased boundary cell wall orthogonal dimension.

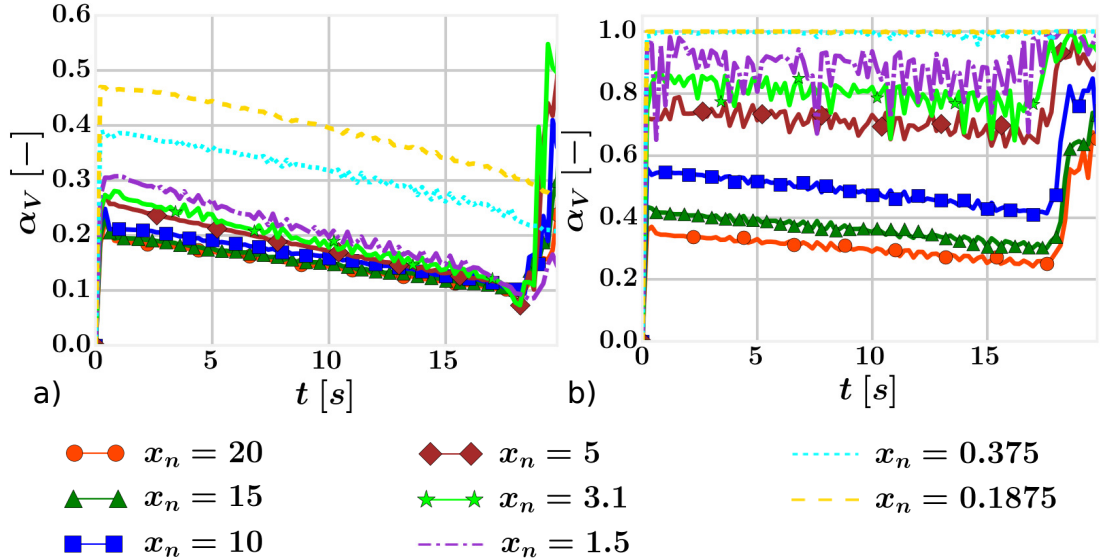


Figure 4.4: Vapour volume fraction using various fluid meshes. The interfacial phase change is not activated. a) Location $L1$; b) Location $L3$

The vapour volume fraction and local HTRs at the plate bottom surface are depicted for the mesh with $x_n = 3.1 \text{ mm}$ (see Fig. 4.5) at 18.2 s. A wetting front is observable where the film boiling faces are adjacent to transition and nucleate boiling HTRs. The phenomenon concentrates at corners and edges, thus locations that undergo the quickest cooling. It is also noticeable where the vapour is being developed and trapped. Fig. 4.4 showed that more vapour tends to be produced during the transition and nucleate boiling. Thus, mainly along the wetting front. The reason is higher thermal turbulent diffusivity (Section 2.3). It is physically correct to experience an increased heat transfer coefficient during the transition and nucleate boiling as well as increased vapour generation, yet it is incorrect to experience higher vapour volume fraction at the wall during these HTRs in comparison with film boiling. This disparity is caused by an inadequate fluid dynamics (bubble dynamics, interfacial terms and boiling models) solution, which is not, at the current setup, able to reproduce the film vapour layer. Thus low heat transfer coefficient during film boiling is not primarily due to the presence of vapour but due to usage of the Bromley correlation (Eq. 2.49).

Throughout these simulations, we should highlight two problematic phenomena that require to be replicated. First, already mentioned, high vapour volume fraction at the wall simultaneously with low heat transfer coefficient during film boiling. Second, increasing heat transfer coefficient concurrently with decreasing wall temperature during partially developed film boiling. Similarly to the first, the second is dealt with by employing a model prescribing the heat transfer coefficient compared to reality where the contact area between liquid and heated wall enlarges, which leads to a higher boiling rate. Replication of these two phenomena is very challenging and remain an open question to solve. Nonetheless, their somewhat questionable description within the code does not necessarily mean an incorrect temperature field solution but makes the setup complex, knowledge demanding and problem-dependent due to the usage of various models and correlations.

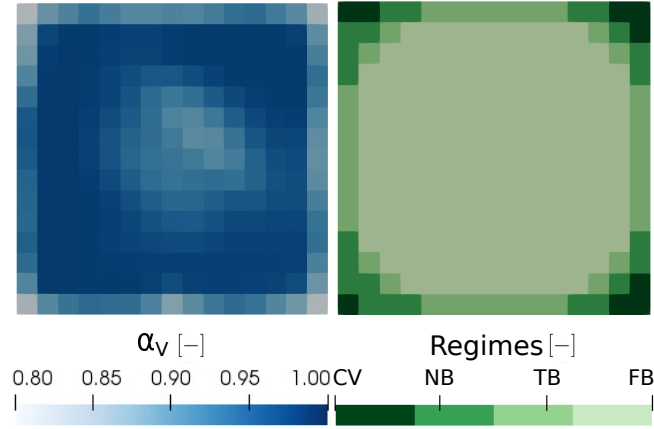


Figure 4.5: Vapour volume fraction and HTRs at the plate bottom for mesh $x_n = 3.1 \text{ mm}$ at 18.2s. The interfacial phase change is not activated.

Here it is discussed why further mesh refinement, meshes with $x_n \leq 1.5 \text{ mm}$, does not lead to mesh independent temperature results. Fluid Biot number Bi_F Eq. (2.86), accounting for the interaction of all three phases at the solid-fluid interface, their properties, volume fractions and mesh, is displayed in Fig. 4.6. Meshes with $x_n \geq 5 \text{ mm}$ demonstrate convergence at both locations $L1$, $L3$. Only a slight increase going hand in hand with refinement is notable. Significant jumps, however, appear for meshes with $x_n \leq 0.375 \text{ mm}$ at $L1$, and a severe problem emerges at the location $L3$. Looking at Eq. (2.86), it is deduced that this might happen when the solid temperature gradient is significantly greater than the fluid region temperature gradient. Meshes with $x_n \leq 0.375 \text{ mm}$ cause the vapour volume fraction at $L3$ to approach unity, preventing heat transfer into liquid. That leads to liquid Biot number equal to zero, so fluid temperature is dictated solely by vapour temperature according to Eq. (2.85). It would not be an issue unless heat is still directed into the vapour from the solid at a high rate causing the temperature gradient between vapour and the solid-fluid interface to become marginal. An absent temperature gradient between a wall and the free stream flow can lead to singularities in the heat transfer coefficient, as previously discussed by Schlichting and Gersten [105]. The non-converging behaviour mentioned earlier in this section can be explained by a similar singularity that arises when the liquid in the near-wall cell boils completely, leading to an abrupt change of the thermal boundary layer.

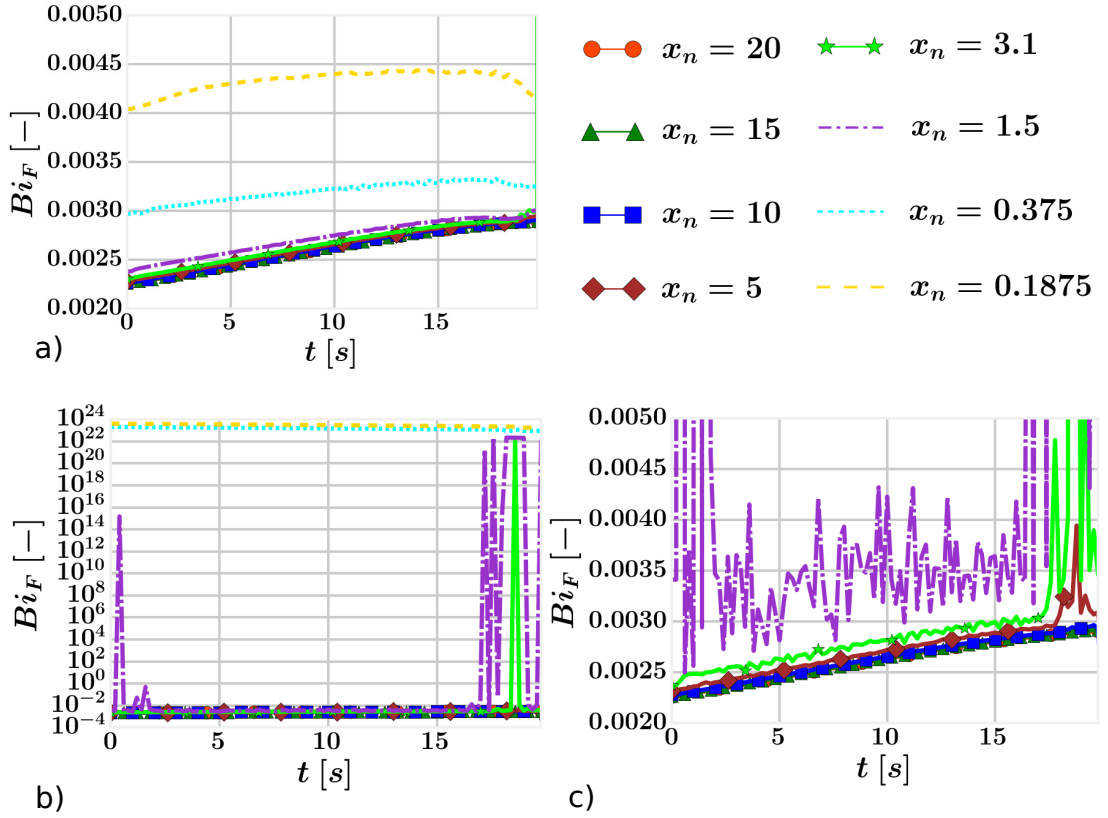


Figure 4.6: Fluid Biot number according to Eq. (2.86) using various fluid meshes. The interfacial phase change is not activated. a) Location $L1$; b) Location $L3$; c) Location $L3$ focused on $x_n \geq 1.5$ mm.

Fluid temperature T_F , following Eq. (2.85), in the boundary cell centre at the location $L3$, is visualised in Fig. 4.7a. Indeed, it is apparent that the fluid temperature approaches the solid-fluid interface temperature for $x_n \leq 0.375$ mm, and occasionally for $x_n = 1.5$ mm. Although the marginal temperature gradient also looms for $x_n = 3.1$ mm, the impact can be disregarded because such conditions arise only for a very brief moment. Meshes with $x_n \leq 1.5$ mm retain these circumstances for a substantially more extended period. Also, it is perceived that problems occur only once the fluid temperature exceeds water saturation temperature.

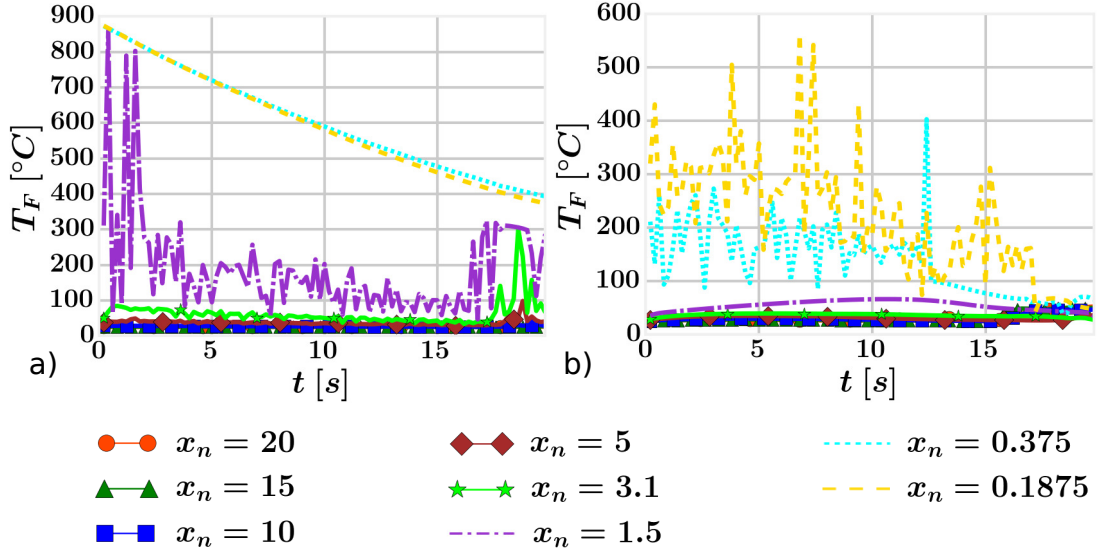


Figure 4.7: Fluid temperature in the boundary cell according to Eq. (2.85) at the location $L3$ using various fluid meshes. a) IPC is not activated; b) IPC is activated.

In the second part of the investigation, the effect of IPC is examined. Fig. 4.8 is directly comparable with Fig. 4.3, the only difference is the IPC being activated. It is understood that meshes with $x_n \geq 3.1 \text{ mm}$ behave equivalently. Even more, meshes with $x_n = 1.5 \text{ mm}$ does not exhibit any severe anomaly. Nevertheless, meshes with $x_n \leq 0.375 \text{ mm}$ manifest considerable distinction. They reveal an effect of other HTRs due to more rapid cooling and quicker reaching of the Leidenfrost point.

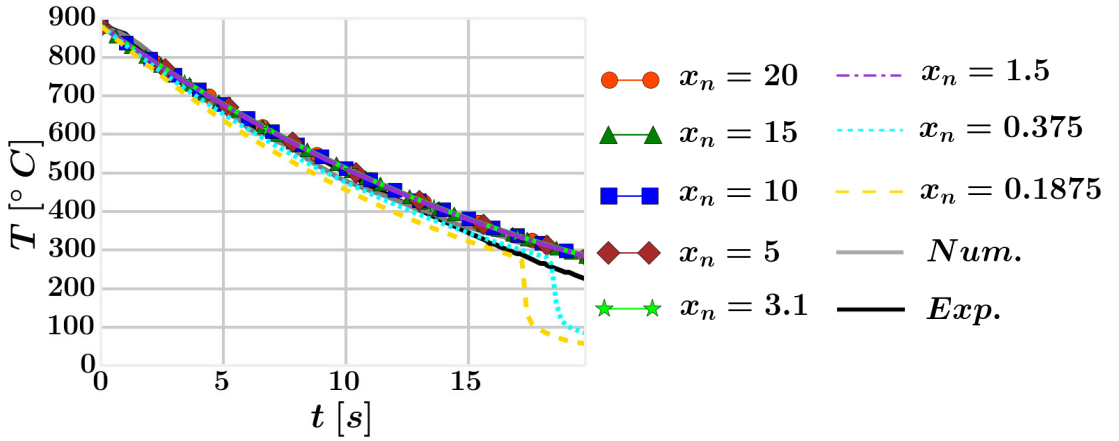


Figure 4.8: Cooling curves acquired at the location $L2$ using various fluid meshes. The interfacial phase change is allowed. Numerical and experimental validation data are taken from Khalloufi et al. [36].

Examining the fluid Biot number Bi_F (Fig. 4.9) and fluid temperature (Fig. 4.7b),

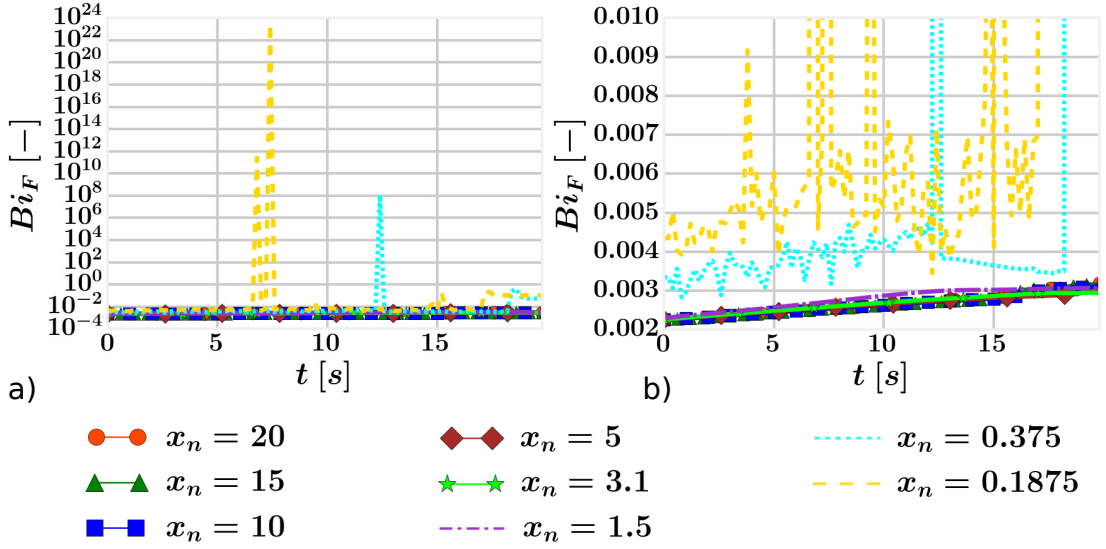


Figure 4.9: Fluid Biot number according to Eq. (2.86) at the location $L3$ using various fluid meshes. The interfacial phase change is allowed. a) Global view b) Focused view on $x_n \geq 1.5 \text{ mm}$.

a considerable improvement for $x_n = 3.1 \text{ mm}$ and $x_n = 1.5 \text{ mm}$ is recognised compared to the problem without IPC. Moreover, mesh configurations with $x_n \leq 0.375 \text{ mm}$ no longer exhibit singular Bi_F values for prolonged periods. These are rather replaced by sporadic spikes accompanied by T_F reaching the solid-fluid interface temperature. That being said, fluid Biot number no longer indicates a major issue yet might imply limiting configuration or probably numerical instability. The critical observation is the fluid temperature fluctuation and the presence of interfacial boiling due to overstepping the saturation temperature. That is not the case for meshes with $x_n \geq 1.5 \text{ mm}$, where interfacial condensation occurs exclusively.

Another profound distinction against the cases without IPC is the liquid-vapour interfacial temperature T_f defined according to Eq. (2.5). As discussed in Section 2.2.3, IPC assumes the interfacial temperature to be equal to the saturation temperature. In contrast, when the IPC is not activated, the liquid-vapour interfacial temperature can vary significantly. A maximum of the liquid-vapour interfacial temperature from boundary cells' centres is visualised for both cases without IPC (Fig. 4.10a) and with IPC (Fig. 4.10b). The former shows a clear and substantial increase in temperature for meshes with $x_n \leq 1.5 \text{ mm}$ compared to the rest of the meshes, which stay at lower magnitudes with minor fluctuation. Furthermore, similarly to the fluid temperature,

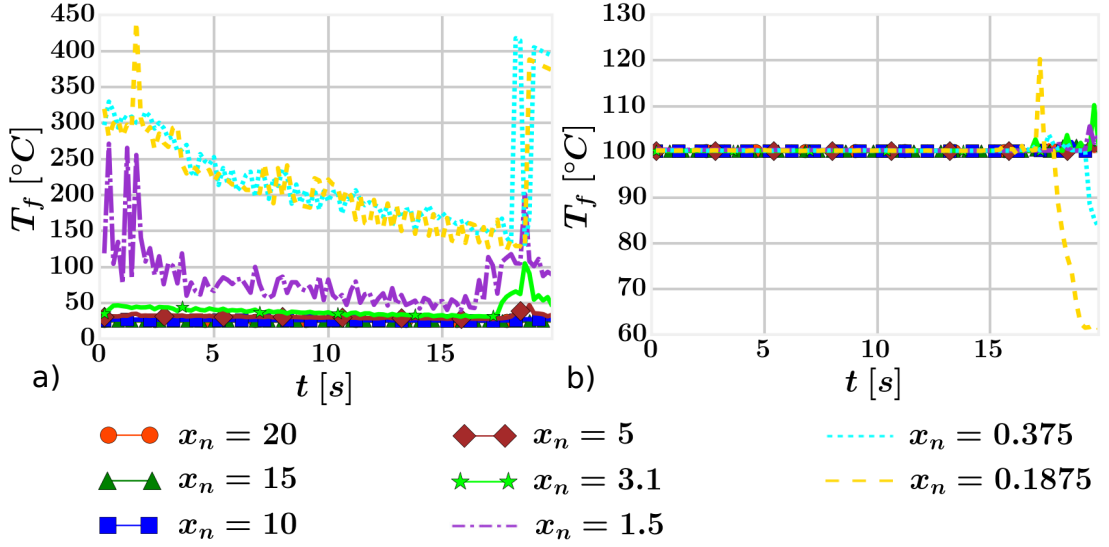


Figure 4.10: Maximum of liquid-vapour interfacial temperature according to Eq. (2.5) from boundary cells centres using various fluid meshes. a) IPC is not activated; b) IPC is activated.

the problematic meshes cause the liquid-vapour interfacial temperature to rise over T_{SAT} . The latter displays the enforced assumption of $T_f = T_{SAT}$. It starts to deviate once a change of HTRs takes place. It is not clear whether the transition complicates the compliance with the assumption. The above is a subject of future research.

The final discussion is reserved for the visual investigation of vapour, total velocity and the solid region temperature with deactivated IPC, which are retrieved at the computational domain centre cross-section. Fig. 4.11 depicts vapour volume fraction and the solid temperature at various times during the simulation. The cooling process begins with the development of vapour surrounding the quenched object. It travels upwards but does not yet reach the upper edge of the visualisation. The second picture shows a fully established vapour mist column and substantially decreased plate temperature. Similar behaviour is observed regarding the vapour volume fraction at 14.0 s, but the solid temperature further drops. Moreover, the vapour blanket apparent beneath the plate gets thinner. That indicates heat transfer regime change, which is even more prominent along the plate edges where increased vapour amount detaches at later time steps. Finally, noticeable vapour crowds are observed rising from the plate edges at 19.0 s.

The total velocity following Eq. 2.15 with the solid region temperature are visualised in Fig. 4.12. Streamlines initially show an undeveloped velocity profile accompanied by

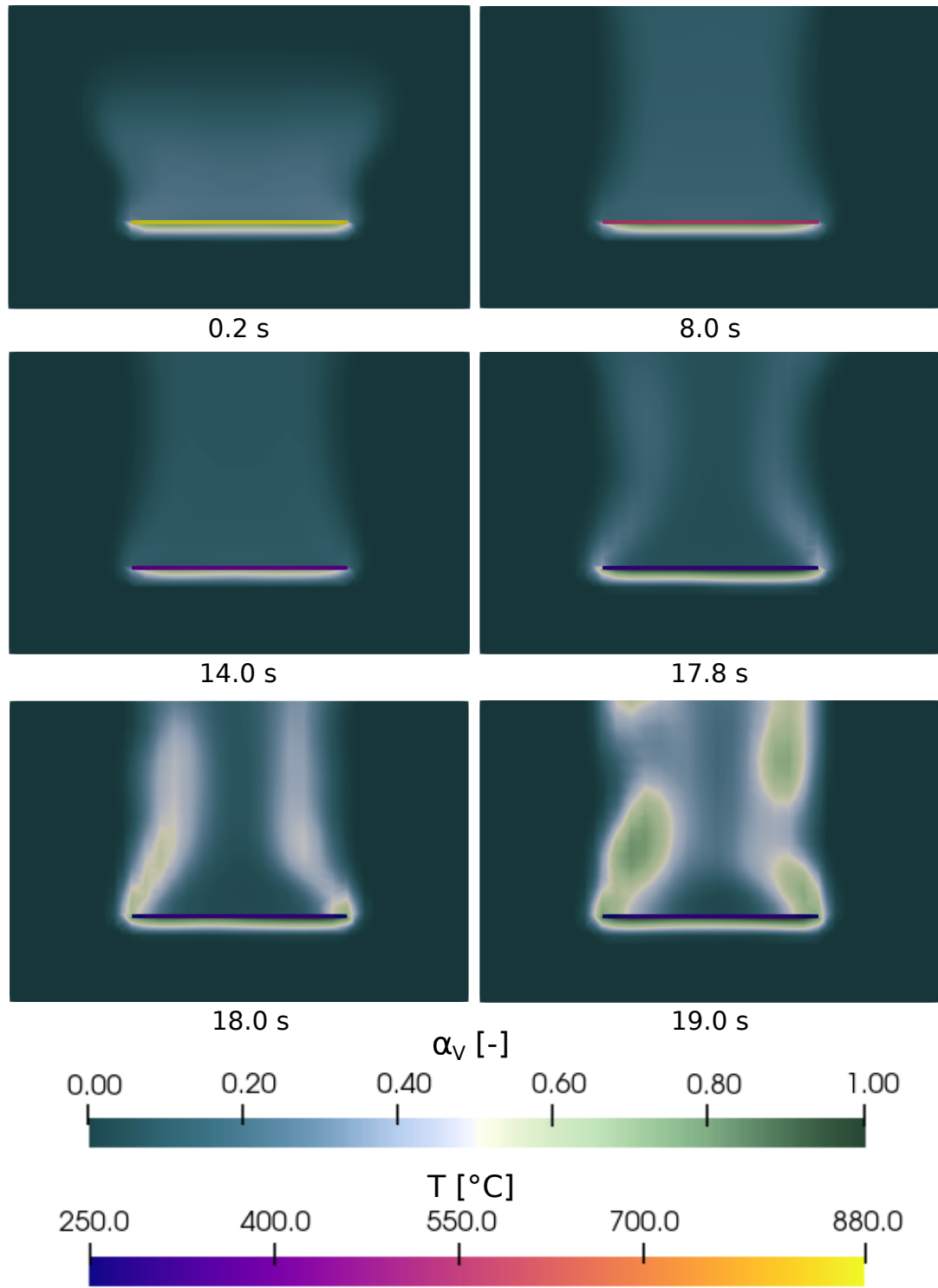


Figure 4.11: Spatial and time distribution of vapour volume fraction and solid temperature fields during the horizontally oriented plate quenching.

two vortices at the interface of the moving and stationary fluid. These travel upwards until the flow is developed as being observed at 14 *s*. A further change to the velocity patterns occurs once more vapour from beneath the plate is released at 17.8 *s*. That leads to increased fluid velocity magnitude at higher vapour volume fraction locations and the development of two asymmetric vortices at the plate top. Their dimensions decrease over time because of the heat transfer regime change at the plate top, starting from the edges and moving inwards to the plate centre. The vapour developed at the top of the plate can detach freely and does not have to go through expansion comparing the vapour flowing from beneath the plate. Finally, the vortices are not visible at 19.0 *s*, and the total velocity magnitude is greatly increased, resulting from the large vapour crowds.

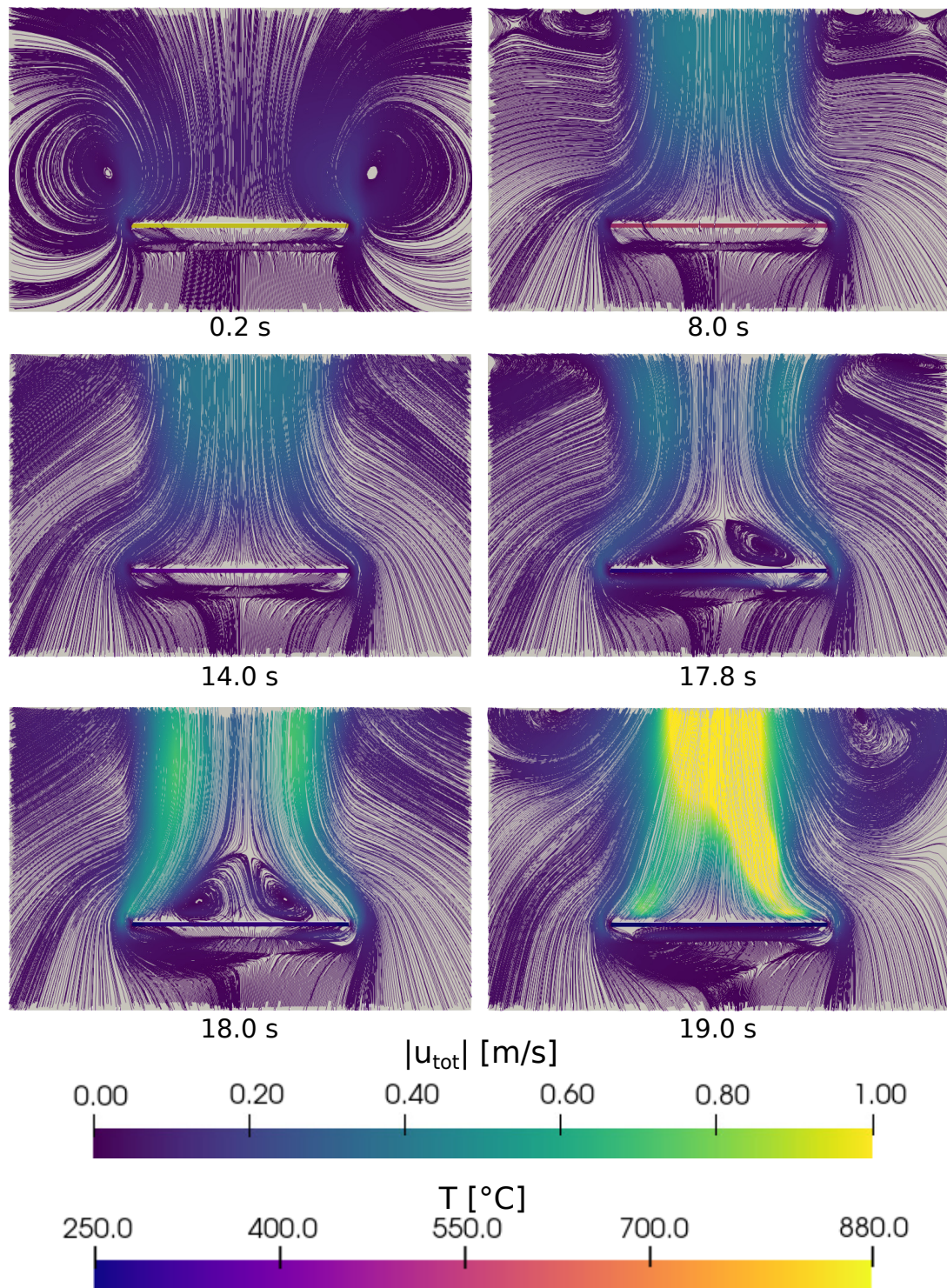


Figure 4.12: Spatial and time distribution of total velocity u_{tot} (Eq. 2.15) streamlines coloured by its magnitude and horizontally oriented plate temperature fields.

To sum up, cooling curves, which are the most important for the problem in ques-

tion, are acceptable for $x_n \geq 3.1 \text{ mm}$ without IPC and $x_n \geq 1.5 \text{ mm}$ with IPC. Also, they agree well with numerical validation data and are slightly lacking behind experimental results. The IPC usage improves the cooling curves of all meshes, but predominantly for the mesh with $x_n = 1.5 \text{ mm}$, which is otherwise not usable. Fluid Biot number and fluid temperature in boundary cell centres give acceptable values for $x_n \geq 5 \text{ mm}$ without IPC and for all grids with IPC if occasional spikes are disregarded, which might indicate numerical stability and accuracy issues. All problematic cases exhibit the fluid temperature above the saturation temperature and nonphysical fluid Biot numbers caused by the absence of fluid temperature gradient in the vicinity of the solid-fluid interface. Furthermore, when IPC is enabled, configurations experiencing interfacial boiling exhibit distinct behaviour compared to those with only interfacial condensation. The present study has validated the solution methodology and clearly shown that either fluid Biot number or fluid temperature in boundary cells should be monitored and used to evaluate computational results. Based on the presented analysis, it is proposed to avoid singular values of fluid Biot number for accuracy reasons.

Finally, information concerning the code compute times for this type of problem is discussed. For the configuration, without *IPC* and mesh with $x_n = 3.1 \text{ mm}$, eight Intel Xeon Gold 6138 (Skylake) processors @2.0 GHz on a two nodes with 40 cores per node were used. One node has access to 192 GB RAM, hence 4.8 GB per core. The elapsed cores time to reach 25 s with maximum $CFL = 0.5$ and maximum time step 0.001 s was 79,194 s. Notice that two regions' coupling, two fluid solution, two fluid energy, two pressure corrector and two solid solution loops were used (Fig. 2.4).

4.4 Summary

The computational methodology developed for boiling conjugate heat transfer using the open-source toolbox OpenFOAM has been validated throughout this chapter. The validation focused on film boiling using an immersion quenching experiment with a high-temperature horizontal plate characterized by distinct heat transfer behaviour per surface. The bottom surface restricted vapour movement, while the top surface allowed the vapour to detach freely. Moreover, the role of other heat transfer regimes was discussed and qualitatively assessed.

The presented results heavily relied on the previously derived fluid Biot number Eq. (2.86) and temperature Eq. (2.85). It has been shown that fluid Biot number can reach singular values for certain mesh configurations due to abrupt change in the thermal boundary layer and non-existing temperature gradient in the wall vicinity. Thus, they proved to be invaluable means of analysis that should be monitored throughout boiling conjugate heat transfer simulations.

In the next step, the impact of interfacial phase change in addition to wall boiling was investigated. It was found to improve cooling curves results but can lead to distinct behaviour when interfacial boiling occurs, resulting in more rapid cooling.

Finally, shortcomings of the solution methodology were indicated. That includes discussion on vapour volume fraction near the heated wall, heat transfer coefficient and liquid-vapour interfacial temperature. More about these and general methodology behaviour is discussed in Chapter 6.

Chapter 5

Cylinder quenching

This chapter discusses cylinder quenching in a vertical orientation, including analysis of an experiment, computational preparation and simulation results. Apart from focusing on methodology and computational behaviour, physics is also examined. The problem studied here is the most complex of all investigated within this research work. Various HTRs are present, and the impact of immersion is considered. The cylinder is quenched from about $959.65\text{ }^{\circ}\text{C}$ in water at $20\text{ }^{\circ}\text{C}$. Experimental data in the form of cooling curves at various locations are provided by the Advanced Forming Research Centre (AFRC) ¹.

5.1 Experiment description and analysis

Before the numerical simulation is performed, the experiment needs to be described and its results analysed. The quenched cylindrical specimen is made of Inconel 718, and its diameter, as well as height, is 200 mm . Two collars/holders used for its transport, from the furnace to the quenching vessel, are mounted at the top (Fig. 5.1a). The transport is ensured by forklift. Cooling water is at $20\text{ }^{\circ}\text{C}$, while the average initial specimen temperature measured using thermocouples placed in the cylinder is $981.92\text{ }^{\circ}\text{C}$. Ideally, the heating process would result in a uniform temperature throughout the cylinder. However, the initial temperature range is $11.76\text{ }^{\circ}\text{C}$.

¹ Advanced Forming Research Centre
Contacts: Dr Salaheddin Rahimi and Dr Ioannis Violatos
Link: <https://www.strath.ac.uk/research/advancedformingresearchcentre/>

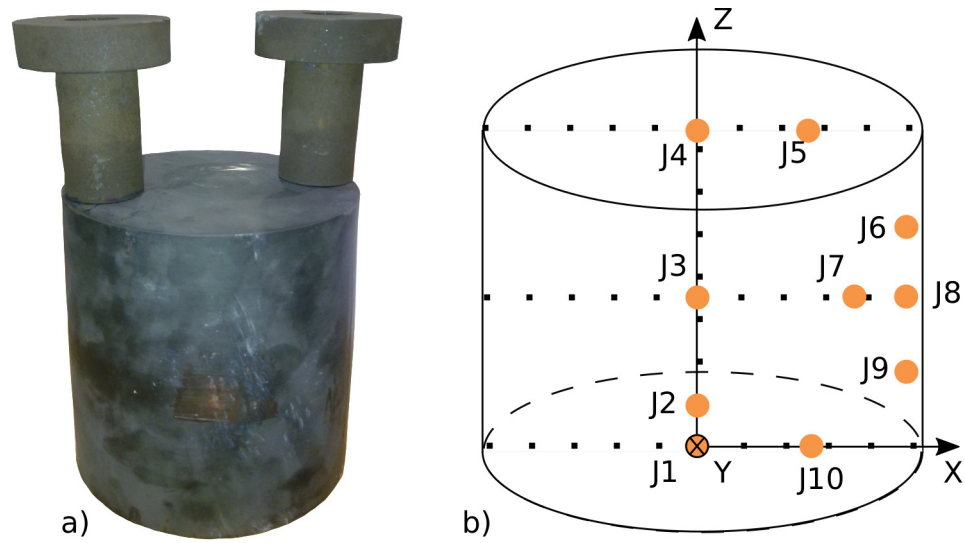


Figure 5.1: Photo of the quenched cylinder with two holders and thermocouples locations used for validation and data collection.

The experimental data are provided in the form of temperature measurements at various locations in the cylinder. These are visualised in Fig. 5.1b (orange dots) and tabulated in Table 5.1. All thermocouples are positioned within the solid specimen by at least 2.5 mm , which leads to a mismatch between the values at the cylinder's surface and measurements taken from them. Thus, it may result in misjudgement of the HTR if measurements are used for that purpose.

	x [mm]	y [mm]	z [mm]
J1	2.0	0.0	2.5
J2	2.0	0.0	6.0
J3	1.0	0.0	100.0
J4	1.0	0.0	197.0
J5	51.0	0.0	197.0
J6	97.0	0.0	152.5
J7	93.0	0.0	105.0
J8	96.5	0.0	105.0
J9	97.5	0.0	49.0
J10	49.0	0.0	3.0

Table 5.1: Thermocouples locations used for validation and data collection.

Analysing the experimental results is a crucial step in providing a comprehensive text and explaining the computational setup to a reader. Prior to the measurements, photos taken during the quenching process are discussed (Fig. 5.2). In Fig. 5.2a, the cylindrical specimen is located in the heating furnace, its doors are opened, and a fork-lift uses a lifting collar mounted to the cylinder top to transport it into the quenching vessel. Once the hot specimen is submerged in water (Fig. 5.2b), wetting fronts appear at the cylinder's bottom edge, where the first contact with coolant took place. Additionally, increased cooling is seen above the thermocouple wires. They seem to disturb the thermal boundary layer and cause the vapour film to detach. The likely accompanying effect is turbulence increase or further fluid mixing. Video footage also reveals that the location cools and heats repeatedly (A). Thus, the vapour film is most likely reintroduced. Nonetheless, this phenomenon is not apparent from thermocouple measurements, most likely due to its short period (measurement data are acquired every 0.2 s) or thermocouple locations. In the third figure (Fig. 5.2c), the wetting front emerges at the top of the vertical cylinder surface and Fig. 5.2d displays enlarged colder patches just above the thermocouples wires. The wetting fronts eventually meet, and the cylinder does not emit thermal energy in the visible spectrum anymore (Fig. 5.2e). This cooling stage is characterised by a new phenomenon of large bubbles being chaotically released from the cylinder bottom. These bubbles do not seem to travel to the water surface or liquify. Instead, they break into smaller ones, which is accompanied by loud burst noise clearly audible in the recorded experiment (A). The last figure further depicts the same phenomenon, yet the released bubble is enormous, the size of the cylinder diameter. To clarify, the wetting front is usually defined by a sudden appearance of liquid at a specimen surface once the vapour blanket is disrupted due to its instability. Unfortunately, this event cannot be precisely detected using the current experimental setup. Therefore describing the aforementioned figures, the wetting front term was used more vaguely as a situation when the visible thermal radiation halts.

The experimental data are displayed in Fig. 5.3. The whole specimen cools for more than 2500 s because it stores an extensive amount of energy relative to its surface area. Nonetheless, the research will concentrate on only a limited time range. The crucial and most challenging period to predict is the initial 25 s within the coolant,

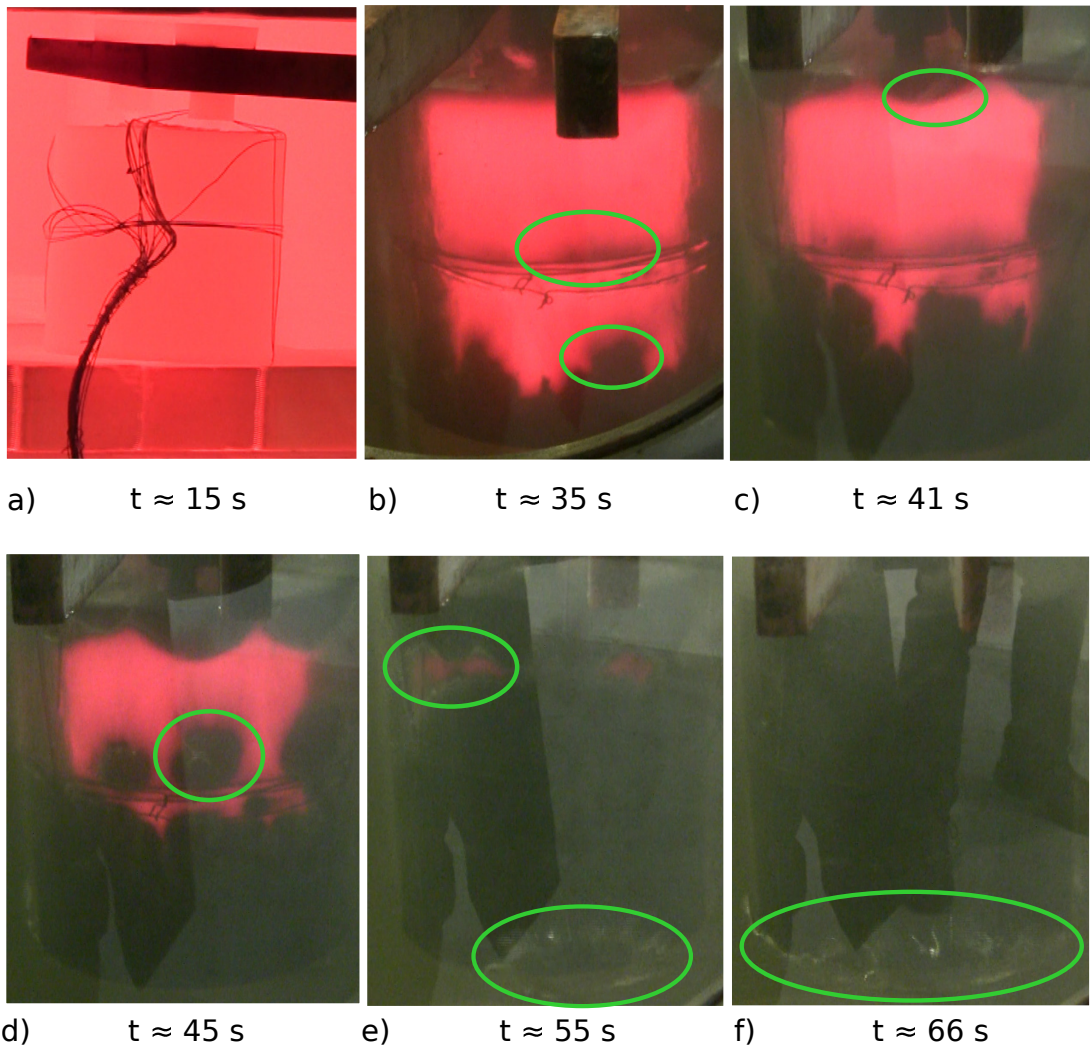


Figure 5.2: Photos from the cylinder quenching experiment with approximate time related to the thermocouples measurements (Fig. 5.3).

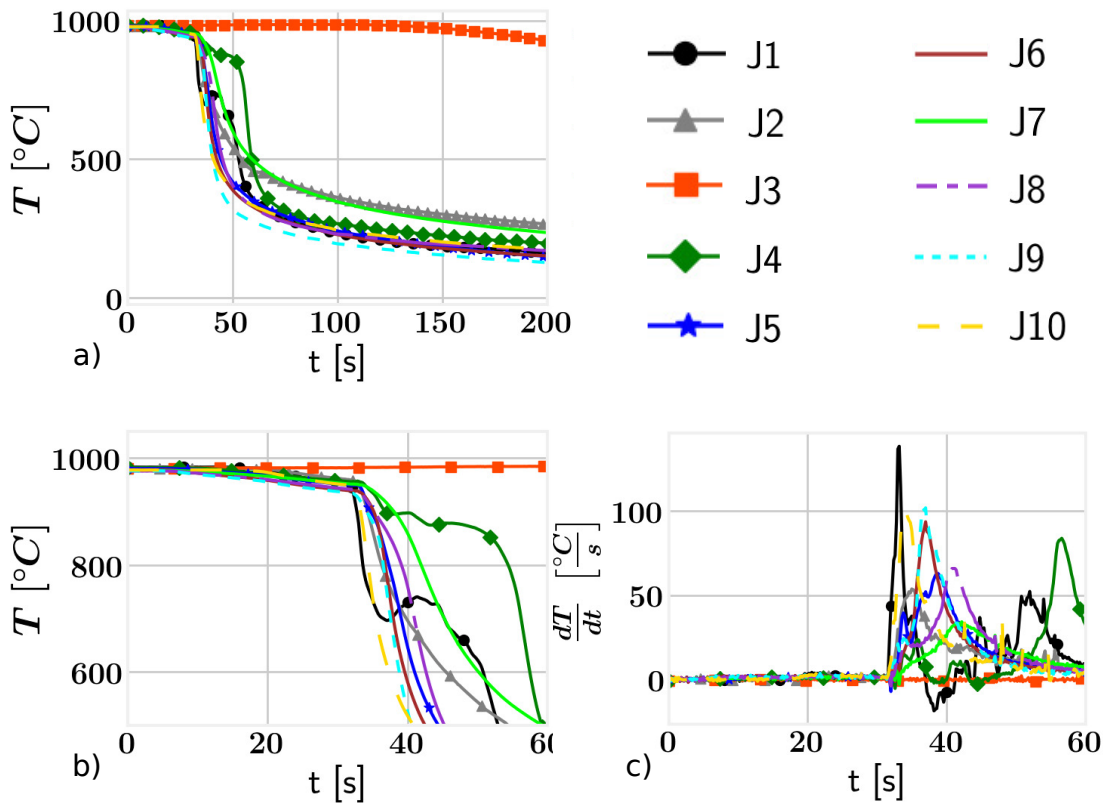


Figure 5.3: Experimental data acquired at various locations within the quenched cylindrical specimen (Table 5.1). a) Cooling curves up to 200 s; b) Cooling curves up to 60 s; c) Cooling rates up to 60 s.

when film, transition and nucleate boiling are dominant. This period corresponds to the time range from 31 to 56 s in Fig. 5.3. Although the simulation of the rest of the experiment is a matter of additional computational time and should not pose any significant challenge, some results of longer simulations (200 s within the water) will be presented and analysed in this chapter. Fig. 5.3a, b show the provided cooling data followed by computed cooling rates, calculated as the time derivative of the temperature measurements (Fig. 5.3c).

Thermocouples $J5$, $J6$, $J9$ and $J10$ have all a similar behaviour exhibiting a rather quick cooling as they are close to the cylinder's surface, not obstructed by vapour and experience relatively high convection. However, other thermocouples such as $J2$ and $J7$ present a slower cooling rate resulting from their positioning deeper within the cylinder.

A unique case is thermocouple $J3$, which exhibits barely any temperature decrease until about 150 s because it is placed in the cylinder's core. On the other hand, thermo-

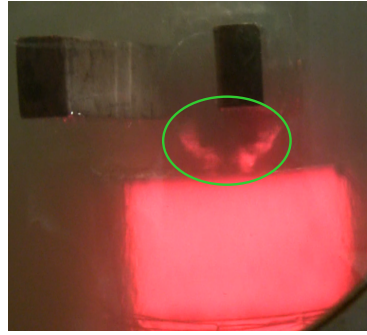


Figure 5.4: Vapour developed at the top of the cylinder after immersion.

couples $J1$ and $J4$ manifest a rapid temperature drop initially, followed by stagnation or eventually even temperature rise. $J1$ is centrally located at the bottom of the cylinder, thus the location where vapour build-up is expected. $J4$ is centrally positioned at the cylinder's top surface, where vapour should detach more freely. Nevertheless, following the temperature readings, it does not seem so. The presence of lifting collars most likely plays its role, as the quenched item is not a standard cylinder but has two additional lifting collars attached to its top surface. Fig. 5.4 demonstrates a relatively high amount of vapour existing at the cylinder top, which can potentially restrict the heat transfer. On top of that, lifting fork holds the cylinder, which certainly curbs the fluid movement.

The next couple of lines are the author's thoughts after spending considerable time studying this problem, and although they have not been tested, they could potentially help design a better test rig. A closer look at the holders' geometry mounted to the cylinder reveals a gap between the holder and screw (Fig. 5.5). The video footage then indicates that the holder can move longitudinally until it touches the screw head (A). The gap between the screw and holder gets enclosed from the top, resulting in vapour release downwards toward the cylinder. Moreover, air may be trapped initially in the gap during the immersion. Obviously, thermocouple $J4$ is in the centre of the top surface, hence between the holders, making it difficult to conclude that this is the definite reason for temperature stagnation. Yet, it is clear that only vapour or air can have such an isolating consequence.

A considerable difficulty in analysing the problem poses the fact that the relative position of the thermocouples to the holders is unknown. Further on, the cylindrical

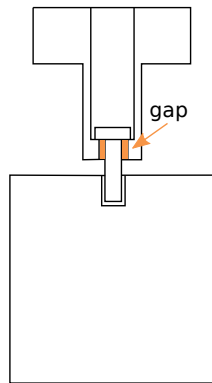


Figure 5.5: Schematic cylinder cross-section after the lift.

specimen is assumed axisymmetric. Thus the holders and forklift effects are neglected, although it is discussed later as a possible cause of discrepancies during the validation.

The quenching numerical simulation also considers the submersion effect, but the provided data already starts in the furnace. Therefore a thorough analysis of the initial 100 s is necessary. Fig. 5.6 displays two typical thermocouple measurements, $J1$ and $J8$. A careful look reveals four different events (Fig. 5.6c, d). Initially, the specimen is in the closed heating furnace ($Fr.$), a period until about 7 s, where the temperature does not change. After that point, the furnace door opens ($Op.$) and remains like that for another 11 s. Only the temperature at $J8$ changes during this time, while $J1$ remains constant. $J8$ is on the cylinder side compared to $J1$, which is on the bottom and isolated by the furnace material. At 18 s, the specimen is taken out of the furnace and transported ($Tr.$) to the quenching vessel (18 – 31 s). Finally, the process continues by immersion for another 2 or 3 s ($Im.$). Thus to conclude, it is decided to skip the initial 31 s and compare the computational results only to the actual immersion quenching process data.

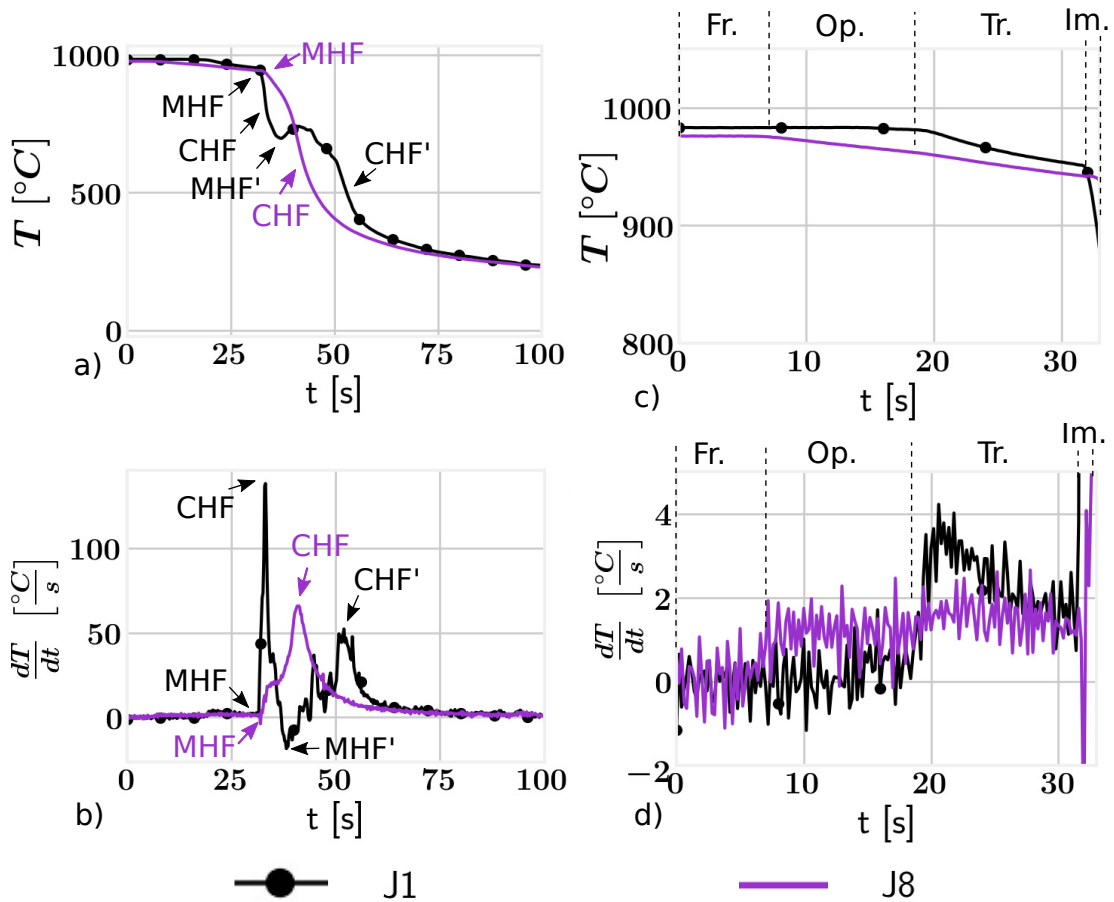


Figure 5.6: Analysis of heat transfer experimental results acquired at locations *J1* and *J8*. a) Cooling curves at the period 0 to 100 s; b) Cooling rates at the period 0 to 100 s; c) Cooling curves at the period 0 to 33 s; d) Cooling rates at the period 0 to 33 s. *Fr.* - Furnace; *Op.* - Furnace opening and forklift positioning; *Tr.* - Specimen transport; *Im.* - Specimen immersion; *CHF* - Critical Heat Flux; *MHF* - Minimum Heat Flux.

After determining the events at the beginning of the measurements, the analysis proceeds to the HTRs characteristics identification. The cooling curves (Fig. 5.6a) show a trend shift near the rapid temperature drop at the point of immersion. This phenomenon is the Minimum Heat Flux (*MHF*), hence the Leidenfrost point (*LEID*). It appears slightly sooner for *J1* since it is immersed before the *J8*. Further on, inflexion points are notable. These correspond to the peaks of cooling rates (Fig. 5.6b) and represent the Critical Heat Flux (*CHF*), hence, the Departure from Nucleate Boiling (*DNB*). Again this phenomenon happens earlier for *J1* because of the same reason as before. Soon after this point, the cooling behaviour becomes very distinctive. On one side, the vapour is not allowed to detach freely from the bottom surface resulting

in vapour film creation and temperature increase ($J1$ at about 37 s). The cooling rate curve exposes this behaviour by showing negative values with another minimum and critical heat fluxes (MHF' , CHF'). On the other side, the cooling trend at $J8$ is simpler to follow and does not present any unusual behaviour. Nucleate boiling and convective heat transfer are encountered, and temperature declines towards the surrounding quenchant's value.

What can be drawn based on this analysis? Firstly, the cooling behaviour at different locations might vary substantially, which complicates the thermal turbulence diffusivity replication. Secondly, multiple heat flux peaks (CHF s) and dips (MHF s) can occur during one quenching procedure. Moreover, they can take place at very different temperatures and heat fluxes. Thirdly, the cooling does not have to begin with film boiling. It can be omitted, $J8$, or appear later due to the vapour build-up, $J1$. Thus, nature does not necessarily obey the simplified example shown by Fig. 1.2. That might seemingly result in problems with the computational methodology when only one model is often used for each particular thermal turbulent diffusivity BC characteristic (Section 2.3). However, due to the different definitions for each fluid phase (Table 2.2) and vapour volume fraction change in the vicinity to the specimen, the behaviour can potentially be replicated accurately. Finally, various components of the experimental rig (thermocouples wiring, holders and forklift parts) might lead to specimen thermal gradient alternation.

5.2 Geometry, mesh, initial and boundary conditions

The computational domain is described using Fig. 5.7. In general, it is very similar to the previous computational problem of the horizontal plate (Chapter 4). An important difference is the cylindrical geometry and the fact that an advantage of symmetry is taken. Hence, only a quarter of the actual domain is modelled. The symmetry assumption is only applicable if the forklift, top holders and thermocouple wiring effects are neglected. This decision was made due to the unknown relative position of the thermocouples to the holding structure and for better mesh control so its impact could be studied precisely. The domain is bounded by a *wall* and at the top is an *outlet*. The regions' interface BCs are labelled *fluid_to_solid* or *solid_to_fluid*, depending on the

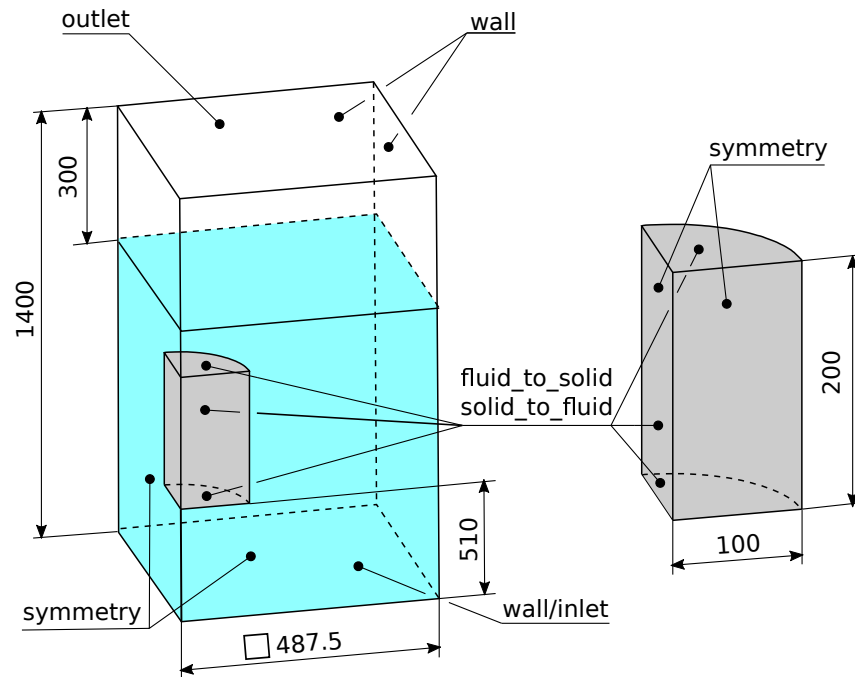


Figure 5.7: Computational domain with dimensions and boundary conditions names.

region of interest. Further, air (vapour) is above the water, which reaches 1100 mm . The gaseous phases, vapour and air, are again considered identical (Section 2.1). The cylinder submerging effect is replicated using the bottom *wall* as an *inlet* where only liquid enters at constant velocity until it reaches the required height. Subsequently, the inlet BC is switched back to the *wall*.

Unfortunately, the exact lowering speed is not known. It ranges between two and three seconds, which results in submerging speed between 0.367 m/s and 0.550 m/s . During the research, the author opts for a water inlet velocity of 0.440 m/s . The water and specimen initial temperatures are uniform at $20\text{ }^\circ\text{C}$ and $959.65\text{ }^\circ\text{C}$, respectively. In reality, the solid region's initial temperature field is more complex. A temperature difference of up to $48.85\text{ }^\circ\text{C}$ between thermocouple readings can be observed when point *J9* has the lowest temperature. To apply such an initial condition, the temperature field would need to be determined, solving the so-called Inverse Heat Conduction Problem (IHCP) [106–108]. That is, in essence, a reconstruction of unknown heat fluxes and temperatures from known temperature measurements.

Table 5.2 provides an overview of the BCs definitions. *Walls* are specified using no-slip BC for both momentum equations, and constant temperature at $20\text{ }^\circ\text{C}$. The

outlet BC behaviour depends on the flow direction. When an outflow occurs, mass flux is positive, zero gradient BC is employed for all momentum and energy equations. While, if the mass flux is negative, inflow velocity is calculated. In such a case, only air at 20 °C enters. The interface BC for fluid resembles a wall for momentum, and liquid temperature is just a copy of vapour temperature calculated according to Section 2.4. The very same definition is also used for the interface temperature by the solid region. The heat transfer coefficient and so impact of boiling is estimated using the procedure from Section 2.3, thus via the computation of the thermal turbulent diffusivity. Finally, symmetry is used for both regions to avoid excessive computational power needs. The simplification does not affect the results.

	$\mathbf{u}_j [\frac{m}{s}]$	$T_L [^\circ C]$	$T_V [^\circ C]$	$T_S [^\circ C]$
wall	noSlip	20	20	-
outlet $\phi_{mf,n,j} > 0$	$\nabla_{\hat{\mathbf{n}}}\mathbf{u}_j = 0$	$\nabla_{\hat{\mathbf{n}}}T_L = 0$	$\nabla_{\hat{\mathbf{n}}}T_V = 0$	-
outlet $\phi_{mf,n,j} \leq 0$	$\frac{\phi_{mf,j}}{\rho_j A_B} \hat{\mathbf{n}}$	20	20	-
fluid_to_solid	noSlip	T_V	Section 2.4	-
solid_to_fluid	-	-	-	Section 2.4
symmetry	$\nabla_{\hat{\mathbf{n}}}\mathbf{u}_j = 0$	$\nabla_{\hat{\mathbf{n}}}T_L = 0$	$\nabla_{\hat{\mathbf{n}}}T_V = 0$	$\nabla_{\hat{\mathbf{n}}}T_S = 0$

Table 5.2: Cylinder boundary conditions. $\phi_{mf,n,j}$ stands for mass flux through a boundary cell face.

The physical properties of all three phases are shown in Table 5.3. All characteristics are assumed constant except the vapour density, which follows the ideal gas law. Liquid density can be defined as constant because the impact of fluid phases density difference is considered to be far more significant. The cylinder material is Inconel 718 and all relevant properties are given in the same table.

Meshes for both regions are purely hexahedral, block-structured, and growth ratios are frequently exploited (Fig. 5.8). The solid region is often more refined than fluid, and the AMI interpolation procedure is used to cope with regions' non-conformity.

	κ [$W/(mK)$]	c_p [$J/(kgK)$]	ρ [kg/m^3]	μ [$Pa\ s$]
solid	11.4	435	8022	-
liquid	0.6	4,185	1000	0.001
vapour	0.025	2010	$\rho(p, T)$	0.000012

Table 5.3: Physical properties of water, vapour and the cylindrical specimen.

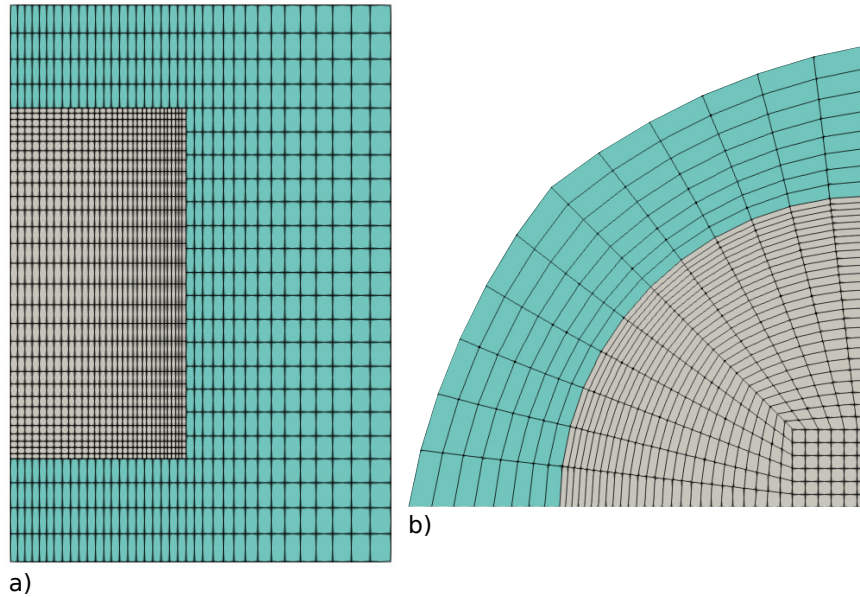


Figure 5.8: Visualisation of the cylinder computational domain combining meshes with 31,140 fluid and 10,440 solid elements. Pictures are truncated and not in scale. a) Side view b) Top view.

Multiple meshes are used to converge each region (Table 5.4). The focus is given to the boundary cells perpendicular dimensions, yet the mesh is refined in all directions. Fig. 5.8 shows an example of regions' computational meshes. The particular mesh combination has 31,140 fluid and 10,440 solid elements. The fluid is visualised using light blue colour while solid is grey. Fig. 5.8a and b show side and top views, respectively. Notice that if any region is refined along the circumference, the number of elements in the radial direction must change to satisfy the block-structured mesh requirement. Also, the growth ratio is not applied alongside any cylinder sides but only above, beneath and radially beyond the cylinder in the fluid region. In contrast, the solid region is discretised using growth ratios in all directions. During the discretisation, the mesh smoothness, especial alongside the interface, was emphasised to cope with high gradients in multiple variables.

Table 5.4 shows the number of elements and perpendicular dimensions of boundary cells for both regions. Throughout the chapter, various meshes combinations are labelled using the total number of elements in each region.

	No el.	Top size [mm]	Side size [mm]	Bottom size [mm]
Fluid	7,335	19.79	8.87	21.28
	31,140	13.49	4.83	13.30
	59,008	10.39	3.46	9.75
	136,720	5.44	2.32	4.91
Solid	3,420	13.33	4.69	13.33
	10,440	3.15	1.92	3.15
	58,800	0.88	0.82	0.88
	182,400	0.48	0.45	0.48
	451,500	0.27	0.28	0.27

Table 5.4: Fluid and solid regions' meshes characteristics, mentioning the total number of elements, and boundary cells interface perpendicular dimensions at the cylinder top, bottom, and side.

5.3 Mesh sensitivity analysis

This section elaborates on the mesh sensitivity analysing data from three locations at the quenched cylinder. These are $J1$, $J4$ and $J8$, cylinder bottom, top and side, respectively. The first part of the section does not consider the IPC, while the second does. IPC at the particular problem configuration brings certain difficulties because the numerical stability becomes more delicate.

Beginning with the fluid refinement, Fig. 5.9 displays cooling curves and cooling rates using a solid mesh with 58,800 elements. It is evident that the sensitivity varies across the locations. Focusing on temperature, relatively small differences at the cylinder's top (Fig. 5.9b) and side (Fig. 5.9c) are recognised. However, very distinct behaviour is observed at the cylinder's bottom, where large discrepancies are manifested (Fig. 5.9a). The fluid region refinement causes an apparent increase in the temperature.

Fig. 5.9d, e and f indicate the cooling rates. Again, the top and side locations

(Fig. 5.9e and f) exhibit a rather good mesh independent behaviour. Perhaps only with the exception of the finest mesh at the side, where the maximum cooling rate is comparatively lower and split into two peak values. The cooling rate at the bottom location (Fig. 5.9d) is very dissimilar. The maximum cooling rate drops with refinement until it vanishes, utilising the most refined mesh, which also causes substantial fluctuation. On the other hand, using meshes with 31,140 and 59,008 elements, a second peak cooling rate at about 20 s is detected.

Based on the previous experience with the horizontal plate (Chapter 4), a rise of vapour volume fraction is the expected cause of the increasing temperature at location $J1$. Visualisation (Fig. 5.10a) indeed shows the build-up of vapour hand in hand with the mesh refinement (2 – 7 s). However, it does not give a definite answer because the fluid Biot number (Fig. 5.10d) declines with refinement, which contradicts the observation from Chapter 4. Perhaps the opposite behaviour is also more expected, looking at Eq. (2.86). The thermal gradient within the solid, so Bi_F , should rise with fluid refinement due to the decrease of δ_F and interface temperature. Unquestionably, that is observable when the cylinder is not yet submerged, approximately 2.5 seconds duration (Fig. 5.10d, e, f). However, a significant change appears at the cylinder bottom once boiling begins, so the reversed behaviour of Bi_F occurs. A plausible explanation is that the vapour isolation limits the regions' interface heat transfer to the extent that thermal energy conducted within solid smooths the solid thermal gradient. Thus, the critical difference against the horizontal plate (Chapter 4) is the heat stored further from the cooled surface.

Further analysing Fig. 5.10a, it is apparent that there is no noticeable difference in the vapour volume fraction between mesh configurations with 31,140 and 59,008 elements at the duration between 7 and 20 s . After that period, a sharp drop is observable. Nonetheless, the finest mesh still causes the vapour to reach its physical maximum. On the cylinder side and top, significant fluctuation with a relatively small impact on the cooling data occurs.

Continuing the mesh sensitivity analysis, the fluid mesh with 31,140 elements is employed and combined with various solid meshes. The cooling curves show convergence for all the locations, including the bottom this time (Fig. 5.11). The coarsest

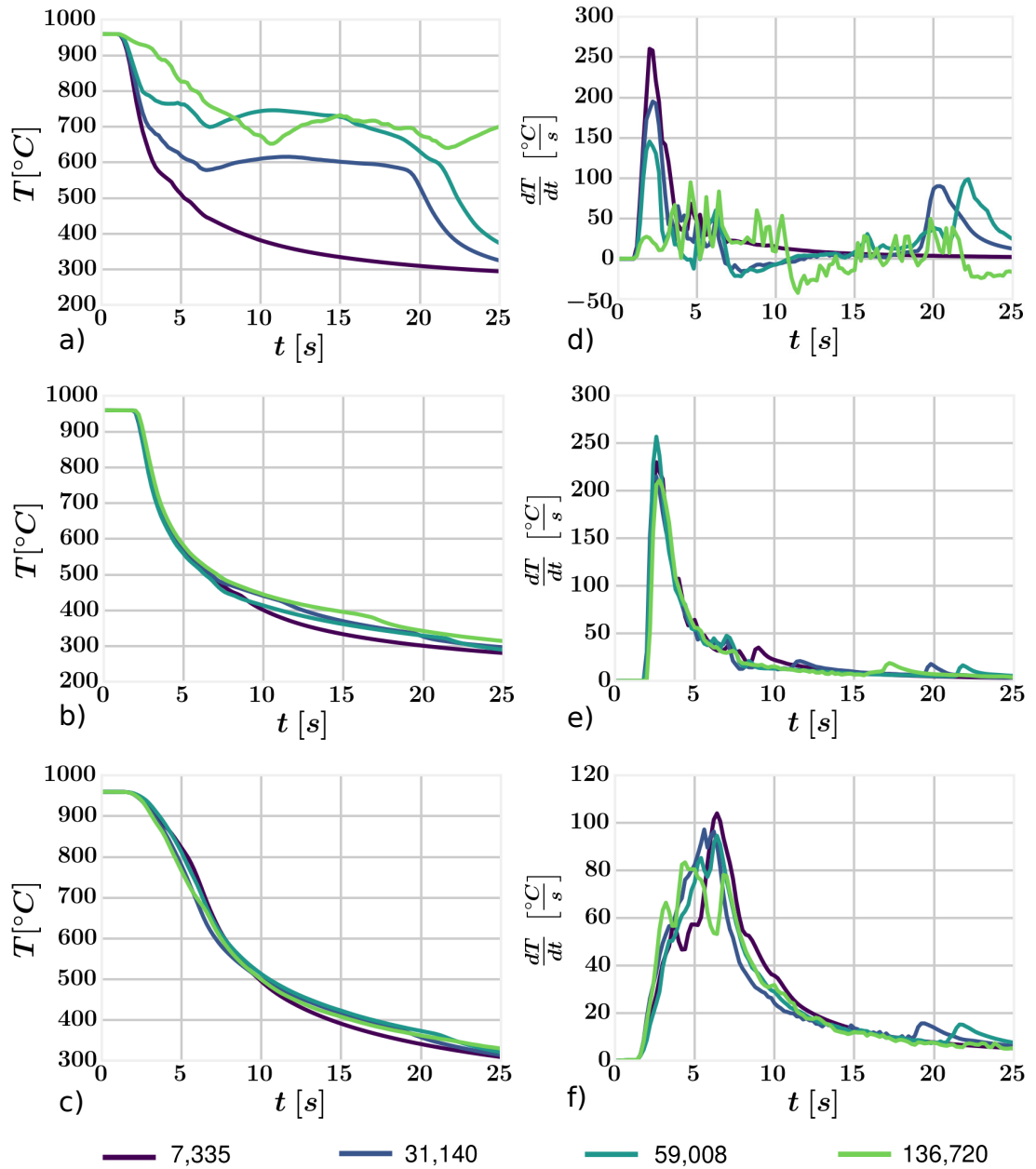


Figure 5.9: Fluid mesh sensitivity study at various locations using solid mesh with 58,800 elements. Visualisation of temperature at a) $J1$, b) $J4$, c) $J8$ and cooling rate at d) $J1$, e) $J4$, f) $J8$.

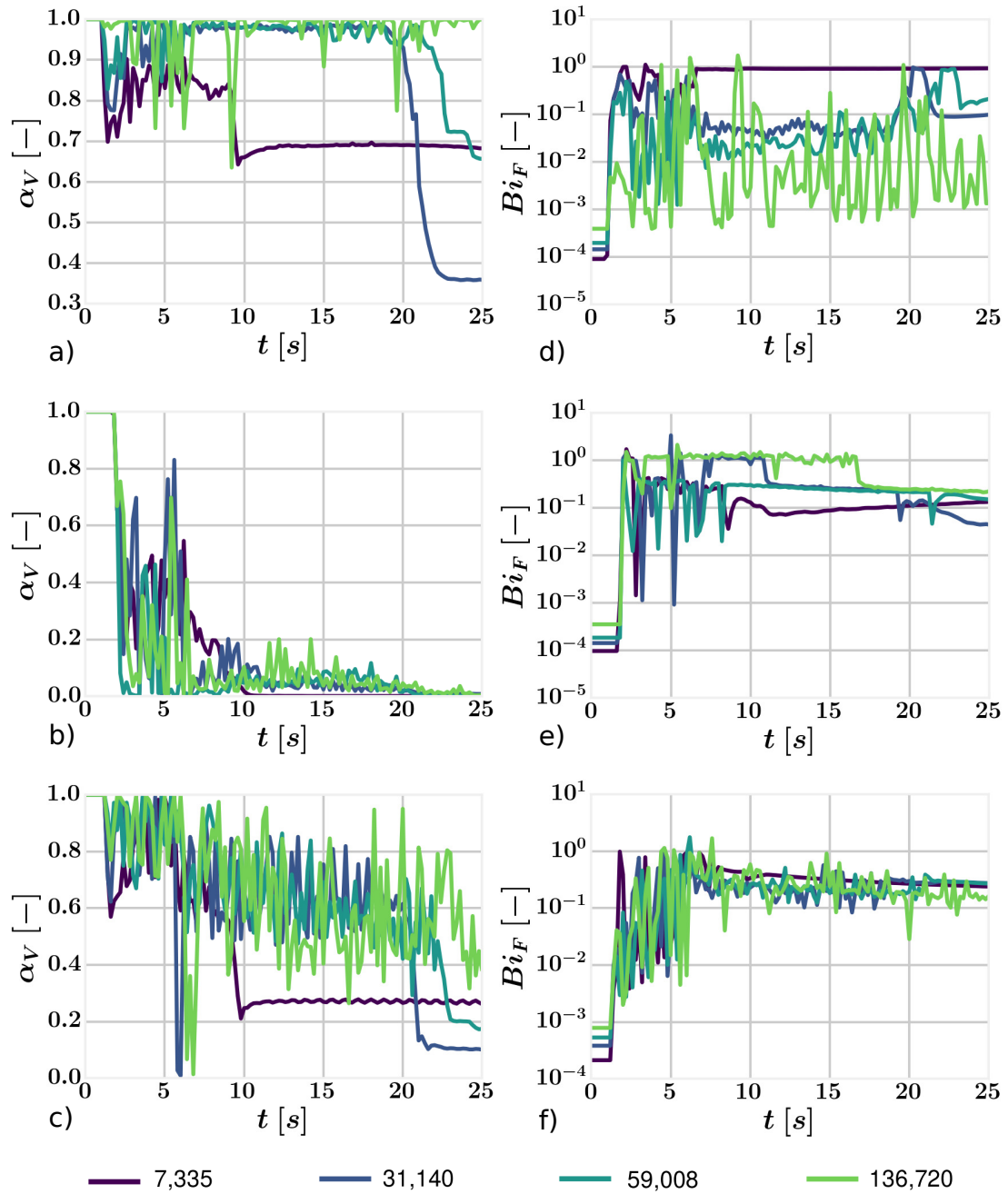


Figure 5.10: Fluid mesh sensitivity study at various locations using solid mesh with 58,800 elements. Visualisation of vapour volume fraction at a) $J1$, b) $J4$, c) $J8$ and fluid Biot number at d) $J1$, e) $J4$, f) $J8$.

mesh exhibits a distinctive cooling pattern as fluctuations appear at the cylinder top and bottom, and the side in smaller magnitude (Fig. 5.11a, b, c). That behaviour is even more apparent looking at the cooling rates, where enormous values are witnessed (Fig. 5.11d, e, f). The refinement improves the results. Cooling curves, as well as cooling rates, are smoothed. The top and side locations converge easily compared to the bottom. There the initial refinement causes temperature rise followed by a drop to the converged curve.

Moving to the vapour volume fraction (Fig. 5.12a, b, c), the values are very different depending on the mesh and location. The two coarsest meshes exhibit large fluctuations. In contrast, the subsequent meshes become more stabilised. At the bottom, the finer meshes approach close to 1, yet meshes with 182,400 and 451,500 cause a reduction after about 10 s . The other two locations still manifest considerable fluctuation but within a smaller range.

Analysis of the fluid Biot number (Fig. 5.12d, e, f) shows what is expected. It drops with the mesh refinement. Thus the temperature gradient importance within the solid region decreases. Also, it reflects the violent behaviour of the coarse meshes.

The analogous analysis is also performed for the solid mesh refinement using the fluid mesh with 59,008 elements (Fig. 5.13). However, this time, solid meshes with 3,420 and 10,440 elements are not used. The reason is the computation instability arising from the usage of finer fluid mesh. One can imagine similar variable fluctuations as shown in Fig. 5.11 and 5.12, yet more exaggerated, leading to instability. The cooling curves (Fig. 5.13a, b, c), as well as cooling rates (Fig. 5.13d, e, f), show very good behaviour for all locations and are largely mesh independent. The main discrepancy seems to be between 3 and 7 s , where the flow is very violent.

Finally, the effect of IPC is studied. However, due to poorer numerical stability, significantly fewer results were generated. Thus the following results investigate the impact of IPC rather than provide a thorough mesh sensitivity study. Stability can be improved by increasing the *nCellsInCoarsestLevel* parameter for pressure GAMG numerical solver and by relaxation of the mass source term at the internal mesh \dot{m}_i . Yet, it is not sufficient for specific mesh configurations. *nCellsInCoarsestLevel* parameter represents the number of cells used at the coarsest level during the mesh cells agglom-

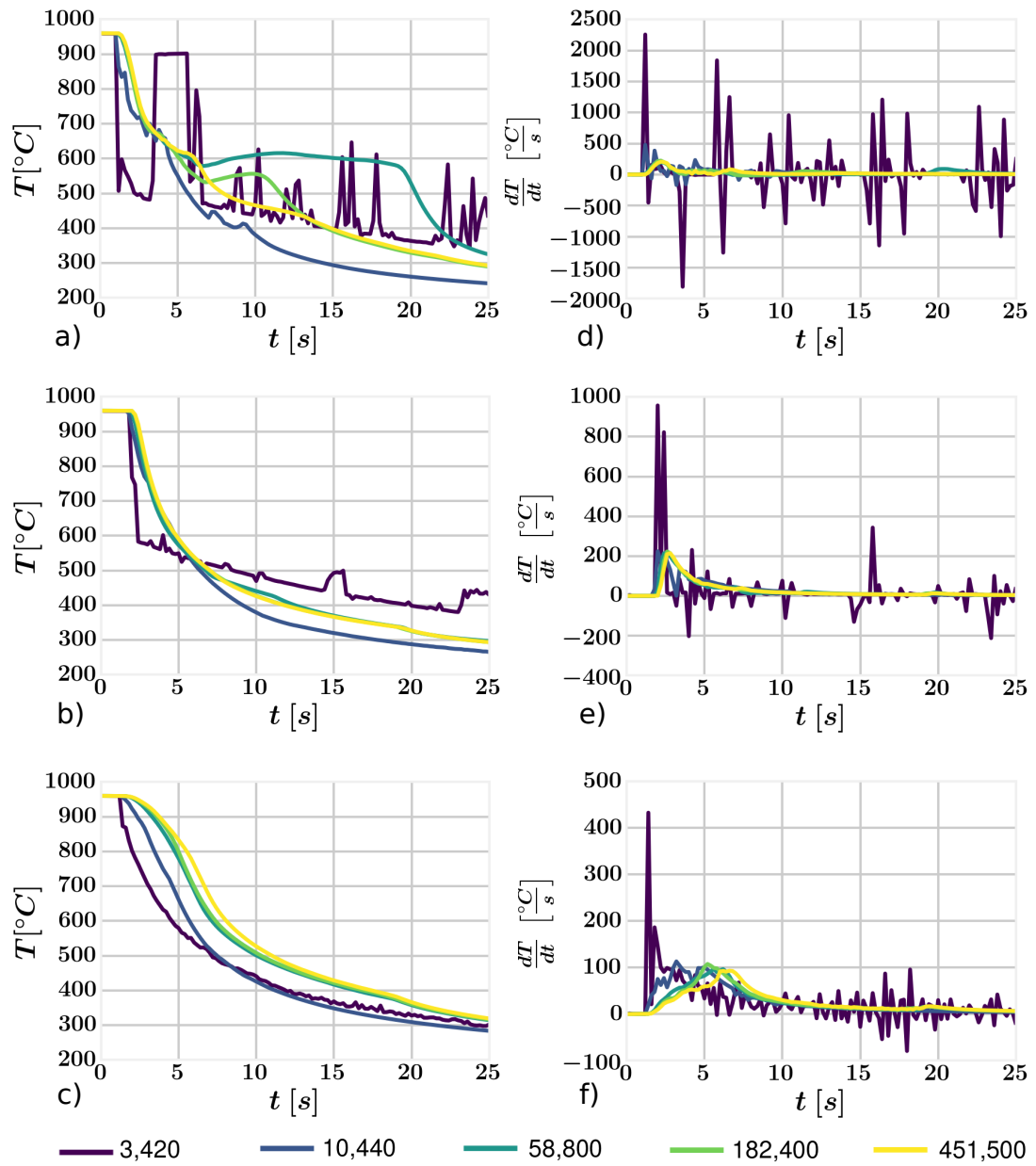


Figure 5.11: Solid mesh sensitivity study at various locations using fluid mesh with 31,140 elements. Visualisation of temperature at a) $J1$, b) $J4$, c) $J8$ and cooling rate at d) $J1$, e) $J4$, f) $J8$.

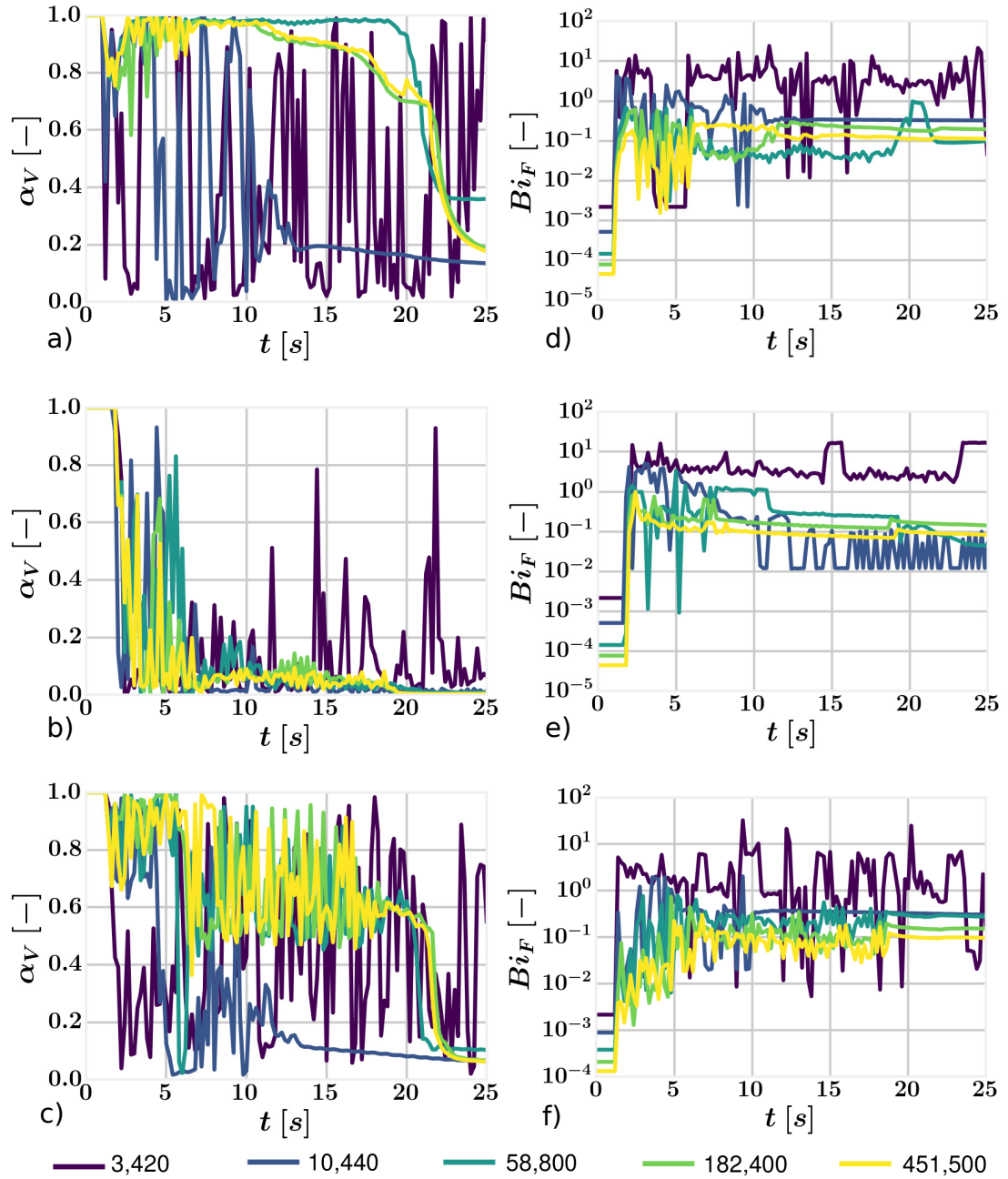


Figure 5.12: Solid mesh sensitivity study at various locations using fluid mesh with 31,140 elements. Visualisation of vapour volume fraction at a) *J1*, b) *J4*, c) *J8* and fluid Biot number at d) *J1*, e) *J4*, f) *J8*.

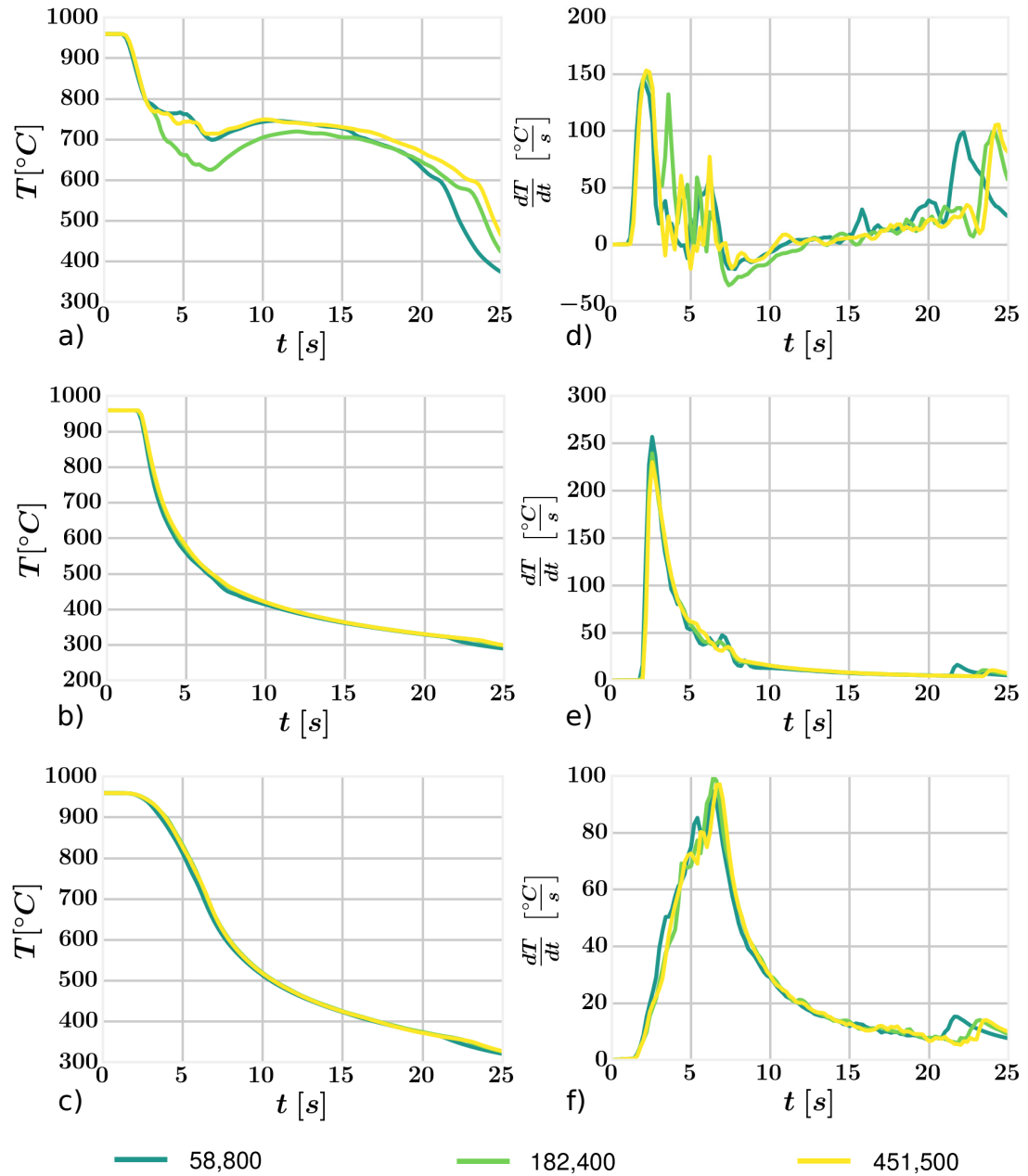


Figure 5.13: Solid mesh sensitivity study at various locations using fluid mesh with 59,008 elements. Visualisation of temperature at a) $J1$, b) $J4$, c) $J8$ and cooling rate at d) $J1$, e) $J4$, f) $J8$.

eration. The values adopted during the following computations with IPC are equal to 1000 and 0.8 for $nCellsInCoarsestLevel$ and the field relaxation, respectively.

The instability appears at certain regions' mesh combinations. Typically, when large temperature fluctuations within the solid region are witnessed. Thus, when the solid mesh is coarsened and fluid is left fine, or fluid is refined but not solid. A typical example would be Fig. 5.11 when the coarsest solid mesh is employed. In such circumstances, high fluctuations in temperature, cooling rate, vapour volume fraction, Biot number and HTRs occurs. Allowing the IPC then leads to instability and computation divergence.

Fig. 5.14 shows two mesh configurations results with activated and deactivated IPC. The finest solid mesh with 451,500 elements is combined with two fluid meshes of 31,140 and 59,008 elements. These two mesh arrangements correspond to the converged computations in Figs. 5.11 and 5.13. In Fig. 5.14a and c, hence at the cylinder bottom and side, the temperature drops as a consequence of increased cooling rate (Fig. 5.14d, f) using IPC. Similarly, the peak cooling rate moves to an earlier time at the side. In contrast, at the top of the cylinder, the coarser mesh with IPC causes a drop in cooling rate between 3 and 10 s (Fig. 5.14b, e). However, that behaviour is not followed by the finer mesh, which agrees well with results without IPC. Thus the coarser fluid mesh with IPC is not converged.

Generally, the temperature changes are well explained by investigating the vapour volume fraction and the fluid Biot number (Fig. 5.15). A substantial vapour volume fraction reduction activating IPC is apparent due to vapour condensation as the water is highly subcooled. The most insignificant effect is visible at the cylinder top (Fig. 5.15b), where vapour played a minor role even when IPC was not activated. The fluid Biot number rises using IPC. The reason is the absence of vapour resulting in the thermal turbulent diffusivity, thus solid thermal gradient rise.

Concluding the mesh sensitive analysis, it is stated that the behaviour is very much dependent on the surface orientation concerning gravitational acceleration, hence, on the extent of vapour movement restriction. The results are found mesh independent on various surfaces yet not at horizontal surfaces facing downwards. There only the solid mesh converges. Increasing the refinement within fluid leads to vapour volume fraction growth, hence to surface isolation. The matter improves by activating the IPC, which

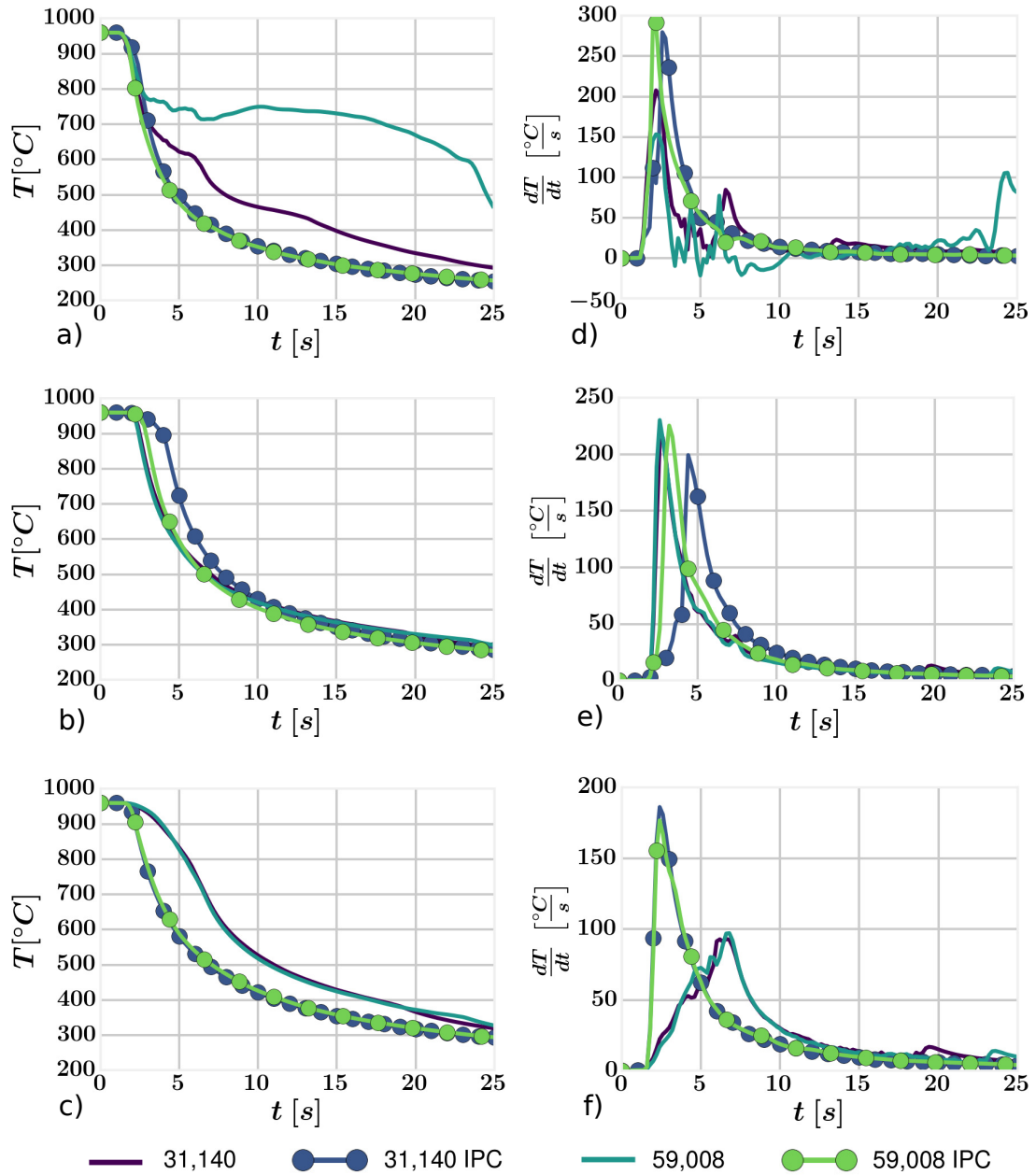


Figure 5.14: Investigation of IPC effect using the solid mesh with 451,500 elements combined with fluid meshes of 31,140 and 59,008 elements. Visualisation of temperature at a) $J1$, b) $J4$, c) $J8$ and cooling rate at d) $J1$, e) $J4$, f) $J8$.

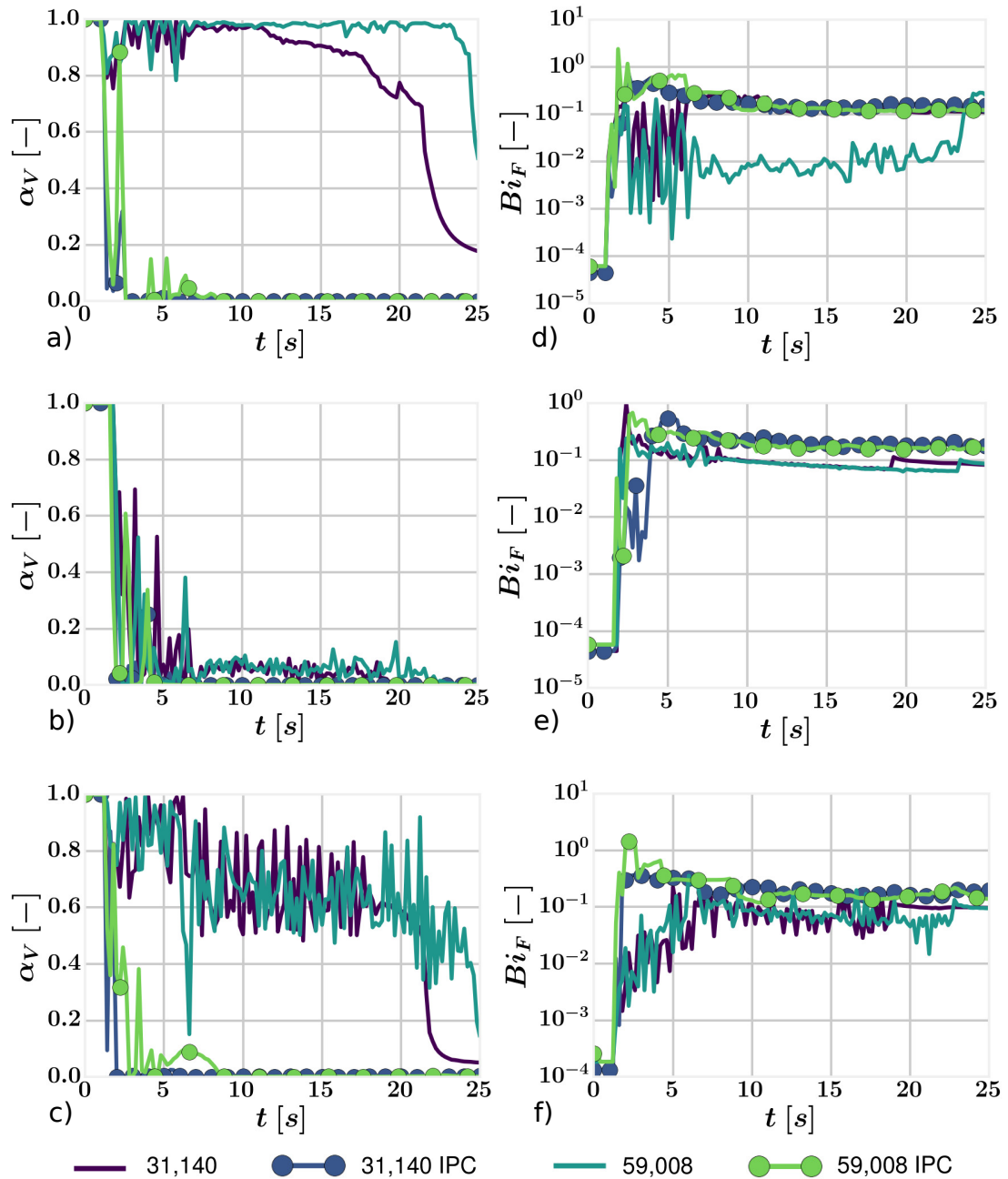


Figure 5.15: Investigation of IPC effect using the solid mesh with 451,500 elements combined with fluid meshes of 31,140 and 59,008 elements. Visualisation of vapour volume fraction at a) $J1$, b) $J4$, c) $J8$ and fluid Biot number at d) $J1$, e) $J4$, f) $J8$.

causes the vapour to condense, so the mesh independence is also reached for fluid. Nevertheless, doing so, the user limits the solver capabilities as vapour obstruction is often desirable. It is further presumed that the behaviour might be improved by accounting for bubble dynamics (break-up, coalescence, agglomeration and condensation). For the results Section 5.4, the meshes with 59,008 fluid and 451,500 solid elements are chosen. This mesh combination is independent of the solid mesh refinement and provides a realistic amount of vapour at the cylinder bottom. Lastly, it should be mentioned that the boiling models applied at the heated wall (nucleate boiling) and their implementation are predominantly used and validated for vertical and forced flows [54, 109–117]. The attempt made here to model the complete quenching process highlights the need for further development.

5.4 Results and discussion

The final section is devoted to the comparison of the numerical and experimental results, eventually physics analysis and discussion. The following series of figures will always investigate particular cylinder locations where experimental results are provided. The focus is given to temperature and cooling rates as a function of time and temperature. Also, each figure has a cylinder schematic with the highlighted location of interest to ease the navigation among the data. At the end of the section, vapour and solid temperature spatial and time distributions are discussed.

To initiate the study, cooling curves at locations *J1*, *J3*, *J4*, *J6*, *J8*, *J9* are visualised (Fig. 5.16). The data duration is limited to 200 *s* from the start of cylinder submergece, which avoids extensive computations. The agreement with experimental results at most locations is perfect, yet, one exception stands out. Fig. 5.16c visualises the results at the centre of the cylinder top surface, where the computed temperature drops substantially more rapidly. The probable cause has been already discussed in Section 5.1, yet to reiterate. It is believed that a substantial amount of vapour acting as isolation is present at the location, resulting from the specimen holder and forklift arms. Further discussion on this topic will be given later.

Apart from the top location, *J4*, it is worth turning the reader's attention to the location at the cylinder bottom, *J1*, where a considerable cooling delay during the

initial 30 *s* exists but is captured (Fig. 5.16a). The side locations, *J6*, *J8*, and *J9* (Fig. 5.16d, e, f), show a temperature development when the slowest cooling occurs at the cylinder mid-height. The most likely cause is vapour build up and detachment as it moves upwards. The last subfigure, Fig. 5.16b, presents temperature data at the cylinder centre. The numerical results catch up with the experiment and decrease at about 150 *s*. However, the cooling rate seems to be a bit lower. That might result from several matters, such as inaccuracy at other locations and neglect of liquid density change.

The rest of the section concentrates on the initial 25 *s*, where the most crucial cooling phenomena appear. This period is dominantly defined by transition and nucleate boiling, yet occasional film boiling and natural convection occur. For instance, the last emerges at the cylinder bottom edge at about 22 *s*. The following figures visualise the HTR changes at the nearest boundary face. However, notice that these changes are predefined by the wall boiling BC (Section 2.3). The HTR changes due to vapour behaviour will not be highlighted visually.

The cylinder bottom is one of the most complex locations for numerical predictions. The key is the vapour distribution and its dynamics. At specific locations, like the cylinder centre (Fig. 5.17a), the vapour volume fraction is so high that the temperature does not even drop for a moment. This behaviour can indeed be termed film boiling. The computational prediction does an excellent job demonstrating this response for an initial 15 *s*, after which the predicted temperature decrease lags behind the measured response. Quite distinct behaviour is observed 3.5 *mm* above the bottom surface (Fig. 5.17c), where the experimental temperature decreases considerably faster despite being further from the regions' interface. This phenomenon is likely caused by high cooling rates at more distant locations where the heat is redirected to. An example is *J10* (Fig. 5.17b), where similar cooling pattern is recognised. This location is about 47 *mm* radially from *J1*, closer to the cylinder bottom edge. The numerical results on both of the locations, *J2* and *J10*, pose a large temperature mismatch compared to the experiment. The author sees the vapour/bubble dynamics as the most reasonable ground to explain this. If any, a small impact can be given to the neglect liquid density change or the fact that water flows in the quenching tank rather than the cylinder being

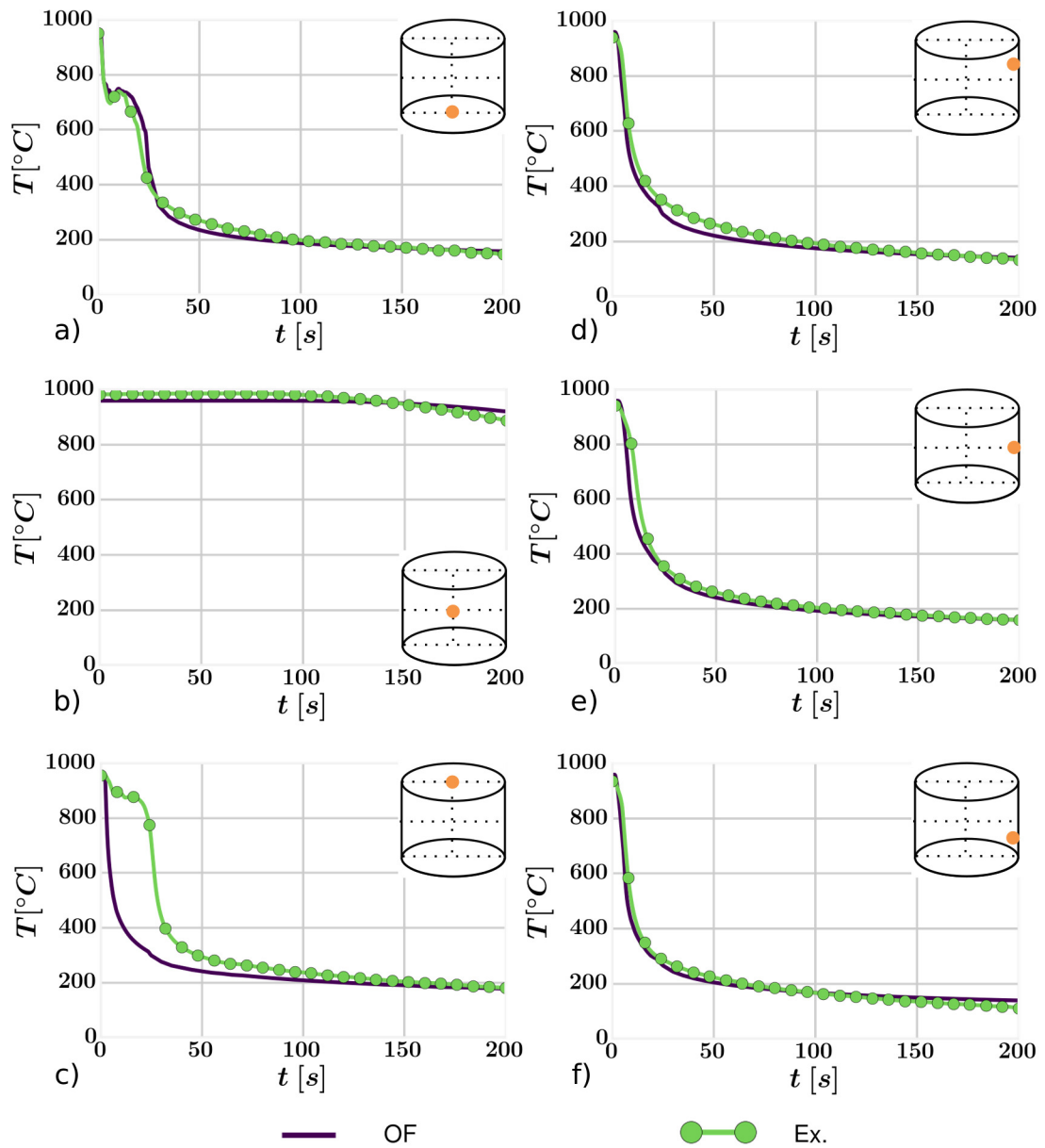


Figure 5.16: Comparison of experimental and numerical results acquired using meshes with 59,008 and 451,500 computational elements for fluid and solid, respectively. The cooling curves at the initial 200 s are visualised at locations a) J_1 , b) J_3 , c) J_4 , d) J_6 , e) J_8 , f) J_9 .

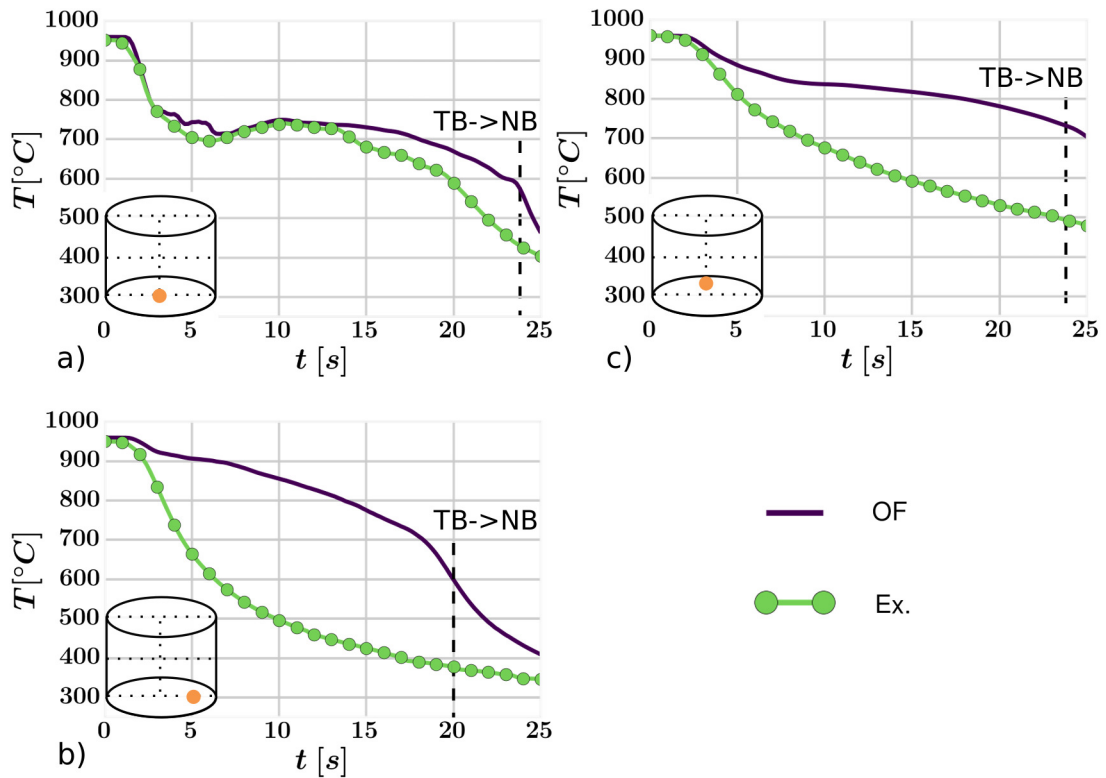


Figure 5.17: Comparison of experimental and numerical results acquired using meshes with 59,008 and 451,500 computational elements for fluid and solid, respectively. The cooling curves at the initial 25 s are visualised at locations a) $J1$, b) $J2$, c) $J10$.

submerged in it.

The cooling curve data are complemented with cooling rates, which are more sensitive to changes and can reveal previously unseen effects (Fig. 5.18). The bottom centre location results, Fig. 5.18a, show nearly perfect agreement with the experiment. From the beginning, the immersion initiates a very high cooling rate which, however, drops quickly to even negative values. The sign change effectively implies heat-up instead of cooling and is observed for both the numerical solution and the experiment. The following 15 s is then delineated by a steady cooling rate rise resembling film boiling until the CHF is reached at about 24 s. That is the only event not agreeing with the experiment.

The location $J2$, right above $J1$, initially shows a promising trend but underpredicts the cooling rate peak followed by cooling rate increase instead of decrease (Fig. 5.18b). Additionally, the second cooling rate peak arrives later because the information takes time to propagate. Moving radially closer to the cylinder edge (Fig. 5.18c) reveals a

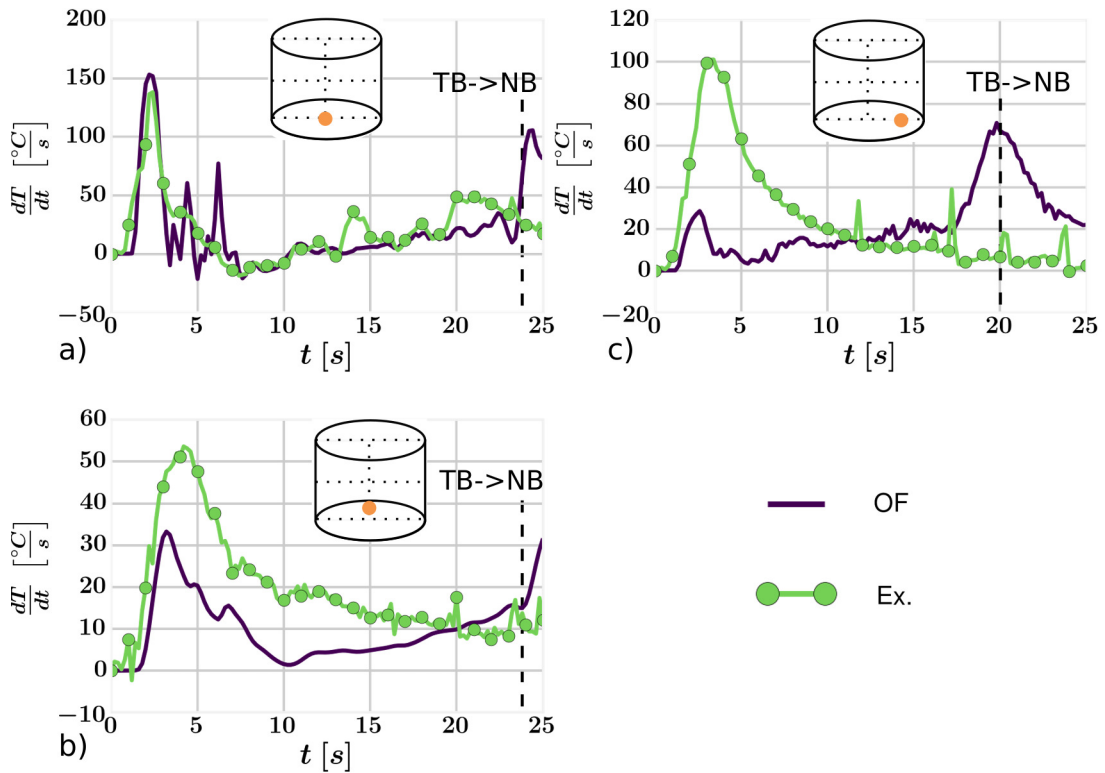


Figure 5.18: Comparison of experimental and numerical results acquired using meshes with 59,008 and 451,500 computational elements for fluid and solid, respectively. The cooling rates at the initial 25 s are visualised at locations a) $J1$, b) $J2$, c) $J10$.

substantially lower cooling rate with a major peak later as modelled by the wall boiling BC.

The last data to discuss concerning the cylinder bottom surface are cooling rates as a function of temperature (Fig. 5.19). Notice that these represent more than the first 25 s of quenching to cover a larger temperature window. It is beneficial that these data are directly comparable to Fig. 2.2 yet, are considerably more involved. Neither experimental nor numerical results manifest initial film boiling at the centre location $J1$, while both exhibit two peaks with film boiling like behaviour between them (Fig. 5.19a). Also, a loop in data appears for both at about 720°C , representing the heat-up as mentioned earlier. Directing the focus to the location deeper in the cylinder, $J2$ (Fig. 5.19b), only one prominent peak is visible during the experiment compared to the numerical solution, which predicts two. Lastly, the numerical solution for $J10$ (Fig. 5.19c) indicates the maximum cooling rate at a significantly lower temperature since it follows an initial period of minimal cooling rate.

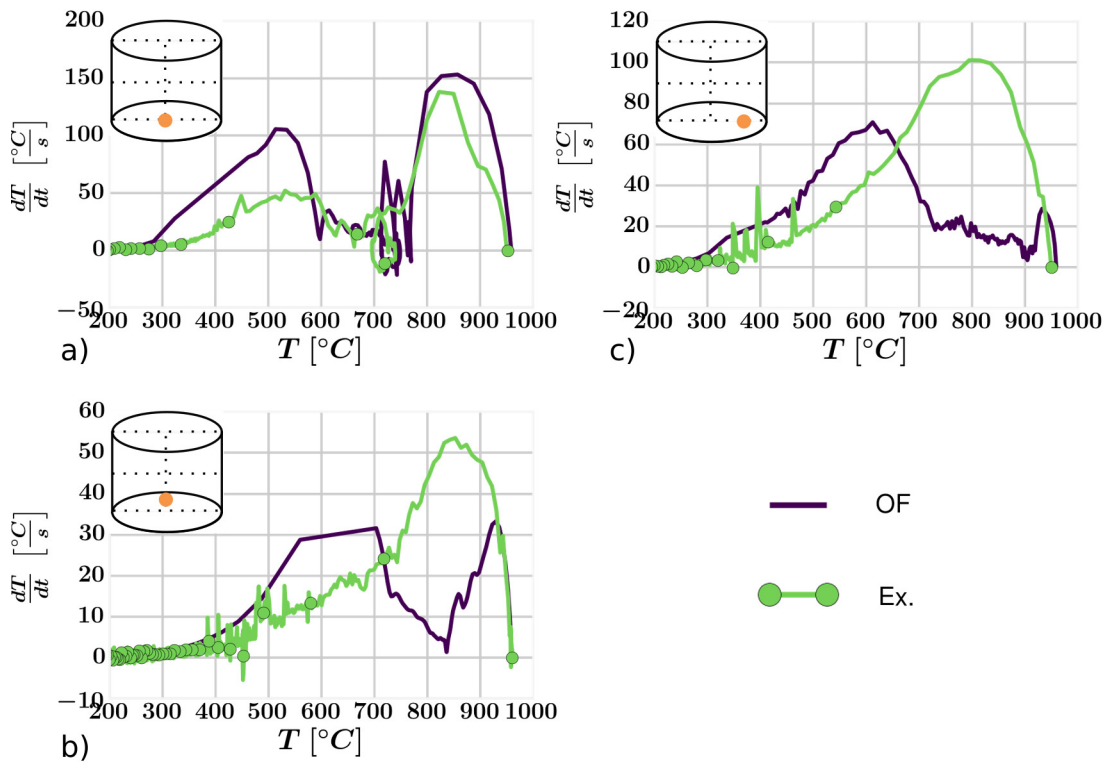


Figure 5.19: Comparison of experimental and numerical results acquired using meshes with 59,008 and 451,500 computational elements for fluid and solid, respectively. The cooling rates as a function of temperature are visualised at locations a) $J1$, b) $J2$, c) $J10$.

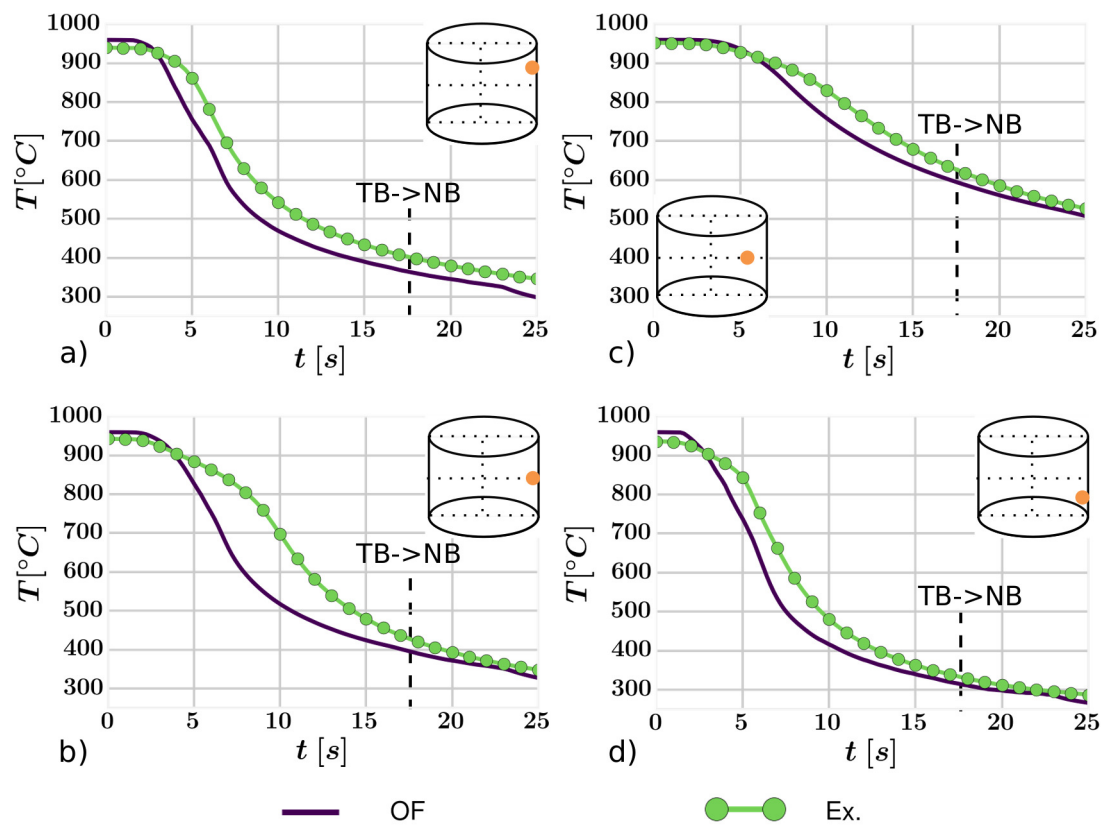


Figure 5.20: Comparison of experimental and numerical results acquired using meshes with 59,008 and 451,500 computational elements for fluid and solid, respectively. The cooling curves at the initial 25 s are visualised at locations a) $J6$, b) $J8$, c) $J7$, d) $J9$.

Now, attention is turned to the cylinder vertical surface. Here, better agreement with the experiment is expected because it resembles usual flow conditions applied in the problems solved in the literature to validate parts of the used methodology. The numerical results are compared to the experiment at four locations, $J6$, $J7$, $J8$ and $J9$, where one of them is deeper in the cylinder (Fig. 5.20). It is concluded that very good agreement is reached for the temperature trends, yet the numerical results generally underpredict the temperature. The most significant discrepancy is found mid-way up the cylinder height, which might be either misprediction of the vapour detachment point or an impact of thermocouples wires (Fig. 5.20b).

The cooling rates plotted against time (Fig. 5.21) provide additional information. Perhaps the first thing to notice is the duration of high cooling rates, where the predicted levels usually last for several seconds compared to the experiment, which are more narrow. Similarly, the initial cooling rates increase earlier. An example is $J8$

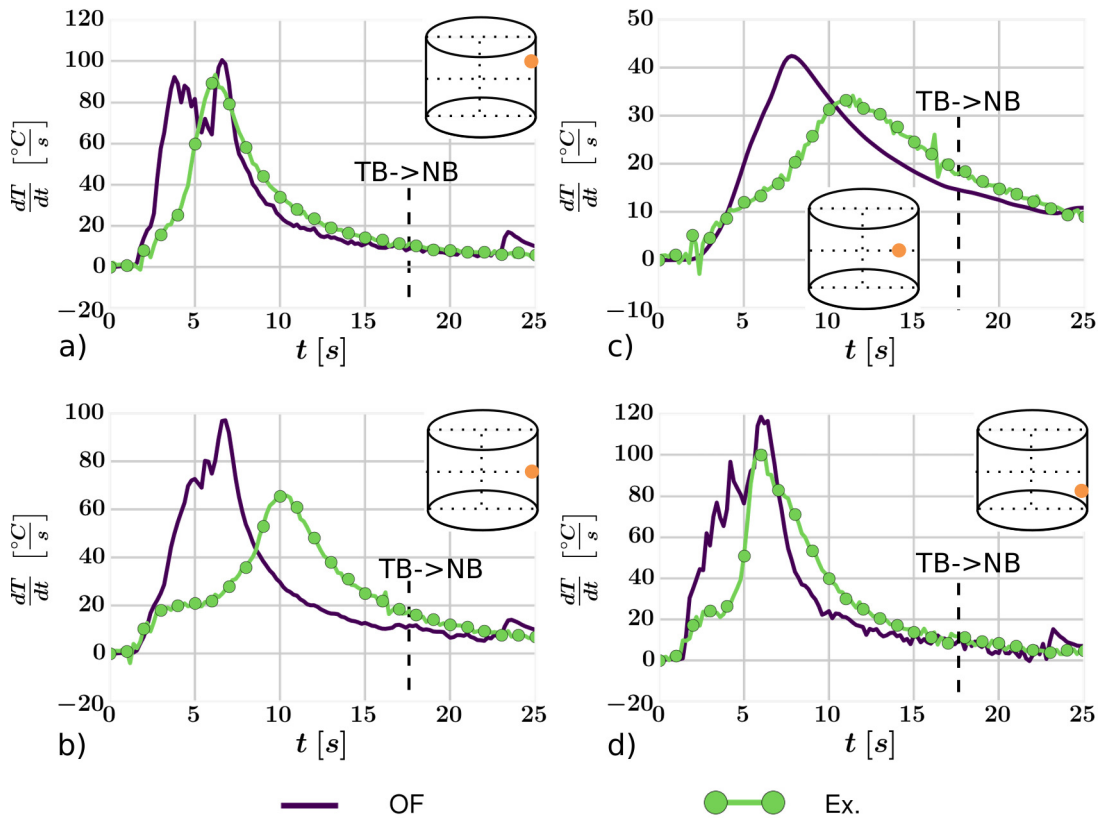


Figure 5.21: Comparison of experimental and numerical results acquired using meshes with 59,008 and 451,500 computational elements for fluid and solid, respectively. The cooling rates as a function of time at the initial 25 s are visualised at locations a) $J6$, b) $J8$, c) $J7$, d) $J9$.

(Fig. 5.21b), exhibiting a significant shift. The difference, as discussed before, may be caused either by thermocouple wires or misprediction of vapour detachment. However, the agreement with the experiment is generally pretty good, especially for $J6$ and $J9$ (Fig. 5.21a, d).

An additional observation is the behaviour of the wall boiling HTR. The change from transition to nucleate boiling appears for all locations within 0.2 s, the sampling period. Thus almost the whole cylinder vertical surface changes HTR nearly at once. Moreover, the change does not invoke any significant cooling rate unevenness. The small peak at about 24 s is provoked by HTR alternation at the cylinder bottom, leading to a drop of the vapour volume fraction.

A decent agreement with the experiment is also visible, observing the cooling rate graphs with temperature (Fig. 5.22). A better curve similarity is apparent compared to Fig. 2.2, which simplifies the cooling prediction. The estimated curves do not seem

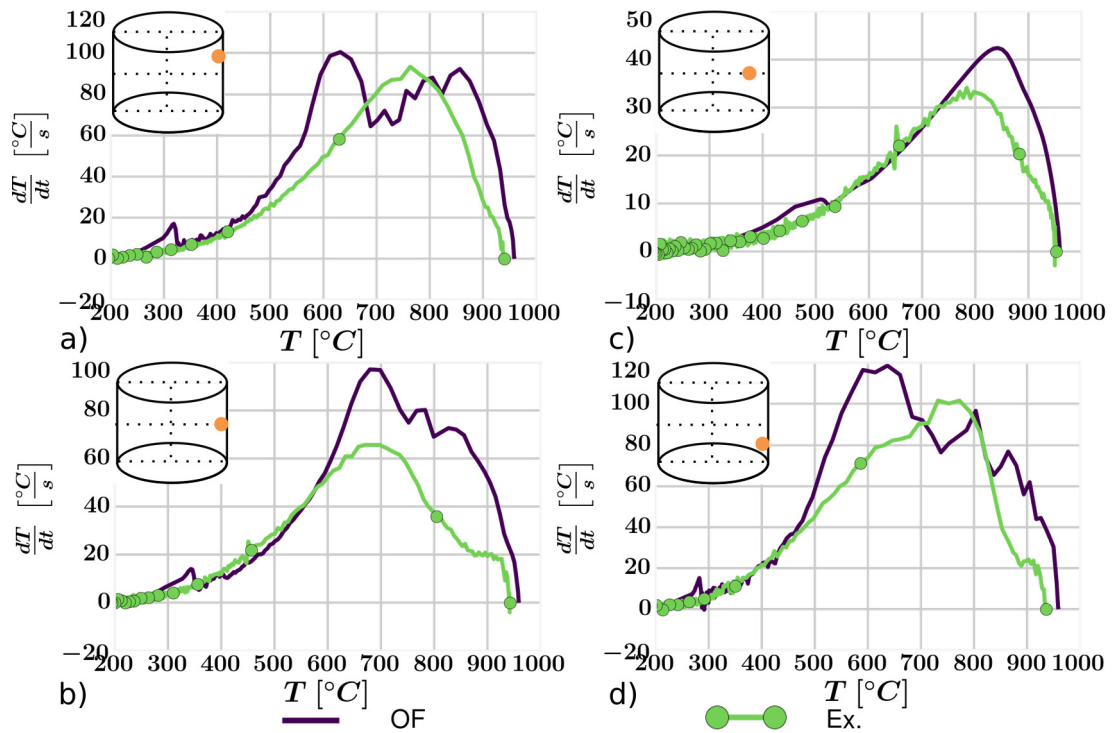


Figure 5.22: Comparison of experimental and numerical results acquired using meshes with 59,008 and 451,500 computational elements for fluid and solid, respectively. The cooling rates as a function of temperature are visualised at locations a) $J6$, b) $J8$, c) $J7$, d) $J9$.

to be shifted in any direction, and the values at the descent from the maximum cooling rates fit nicely. Also, it is noticeable that better agreement is reached deeper in the cylinder (Fig. 5.22c).

The final cooling data concern the top of the cylinder, thus locations $J4$ and $J5$. The assessment is started again with cooling curves (Fig. 5.23). A substantial difference is detected at the central thermocouple, $J4$ (Fig. 5.23a). The experiment demonstrates film boiling like behaviour due to vapour isolation. In contrast, the numerical solution indicates much faster cooling. The immediate reasoning points to the holder structure, present and discussed in Section 5.1. It is hypothesised that the structure generates extra vapour and obstruct its movements. An upward-facing horizontal surface unimpeded by obstacles would allow free vapour detachment.

The second thermocouple, $J5$, placed radially from the centre (Fig. 5.23b), provides substantially better numerical prediction. A reason for the existing discrepancy may have much in common with the neighbouring location. If that was isolated, heat would be conducted to $J5$, and the temperature would be higher. Notice, however, that

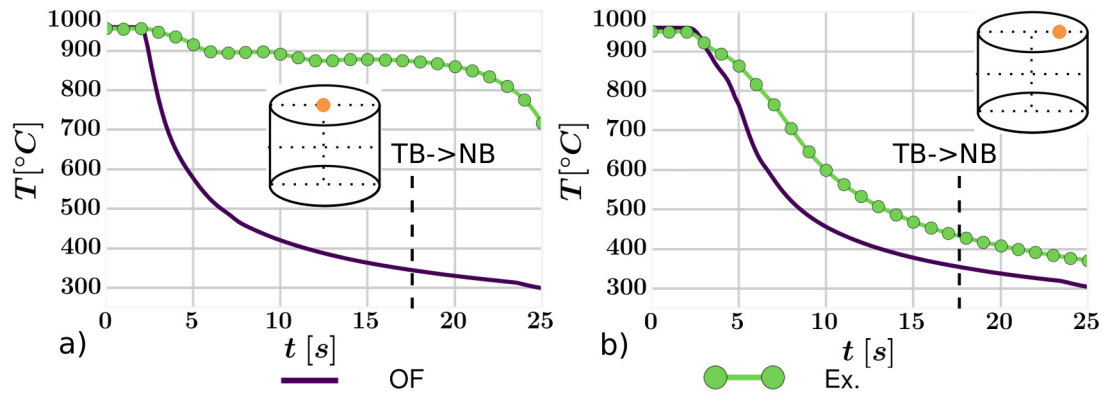


Figure 5.23: Comparison of experimental and numerical results acquired using meshes with 59,008 and 451,500 computational elements for fluid and solid, respectively. The cooling curves at the initial 25 s are visualised at locations a) $J4$, b) $J5$.

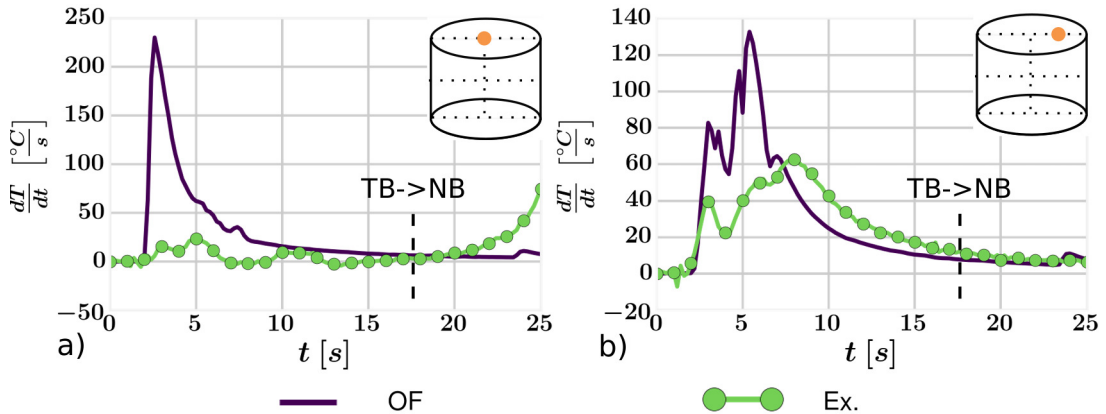


Figure 5.24: Comparison of experimental and numerical results acquired using meshes with 59,008 and 451,500 computational elements for fluid and solid, respectively. The cooling rates as a function of time at the initial 25 s are visualised at locations a) $J4$, b) $J5$.

comparing the numerical results with $J4$, $J5$ manifest significantly slower cooling, which results from the amount of vapour as will be seen later (Fig. 5.26).

The cooling rates results show the very same information (Fig. 5.24). Also, it confirms that the highest computed cooling rates from the whole cylinder are present at the top surface centre (Fig. 5.24a). The value of about $225 \text{ }^\circ\text{C}/\text{s}$ is far above any other investigated location. For example, at location $J5$, the maximum predicted cooling rate is almost half (Fig. 5.24b).

The last data used for experimental comparison are displayed in Fig. 5.25. The cooling rates as a function of temperature show again overprediction of the cooling rates. Besides that, however, it captures a phenomenon of the reduced cooling rate at about $900 \text{ }^\circ\text{C}$ followed by an immediate increase. The event is predicted at a slightly

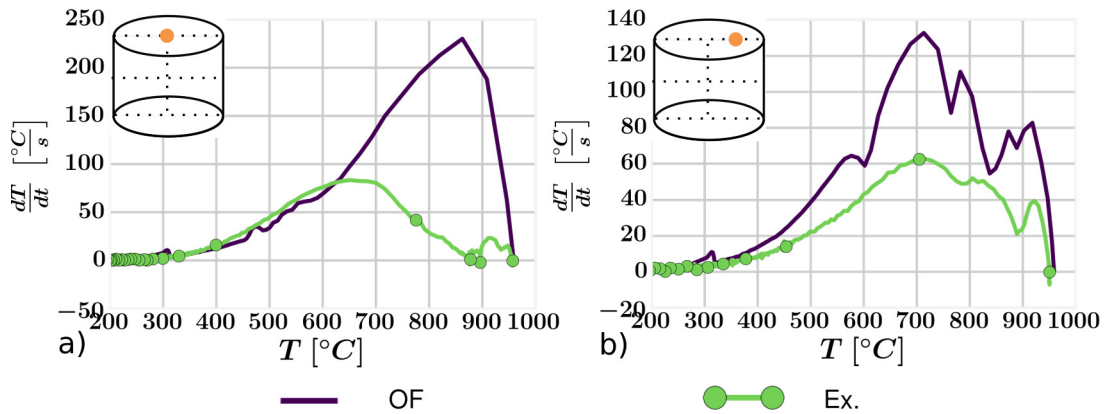


Figure 5.25: Comparison of experimental and numerical results acquired using meshes with 59,008 and 451,500 computational elements for fluid and solid, respectively. The cooling rates as a function of temperature are visualised at locations a) $J4$, b) $J5$.

lower temperature but qualitatively very well. Similarly, it is detectable in Fig. 5.24b, which shows perfect time-wise agreement.

The final part is devoted to a visual investigation of vapour, total velocity and solid temperature's spatial and time distributions. Fig. 5.26 depicts the vapour volume fraction field near the hot cylinder at various times along the cooling process. It begins with submerging when liquid advances up the cylinder. The fluid phases move violently, the air is partially trapped under the cylinder, and vigorous boiling appears. At about 2 s, the cylinder is already fully immersed, yet large bubble crowds and vapour columns are being developed and released from its surroundings repeatedly. After a couple of seconds, a different flow pattern emerges. At about 8.6 s, only smaller bubble crowds are released. Later on, at 22 s, vapour keeps developing and flowing alongside the cylinder, however, no patches of high vapour volume fraction are visible. The only exception is the cylinder bottom, where the surface still seems to be covered by the vapour layer. Finally, at about 55 s, the vapour generation is relatively tiny, but nucleate boiling is still dominant HTR. Concerning the misprediction at the cylinder top surface, a liquid phase is always visible at the centre location. The vapour is not capable of disturbing the central liquid column nor trapping the liquid, so it evaporates entirely.

Fig. 5.27 shows the same view at the computational domain as Fig. 5.26, yet the vapour volume fraction is swapped for streamlines of total velocity (Eq. 2.15). Prior to the cylinder immersion, at 1.2 s, the flow pattern is dominated by vapour which

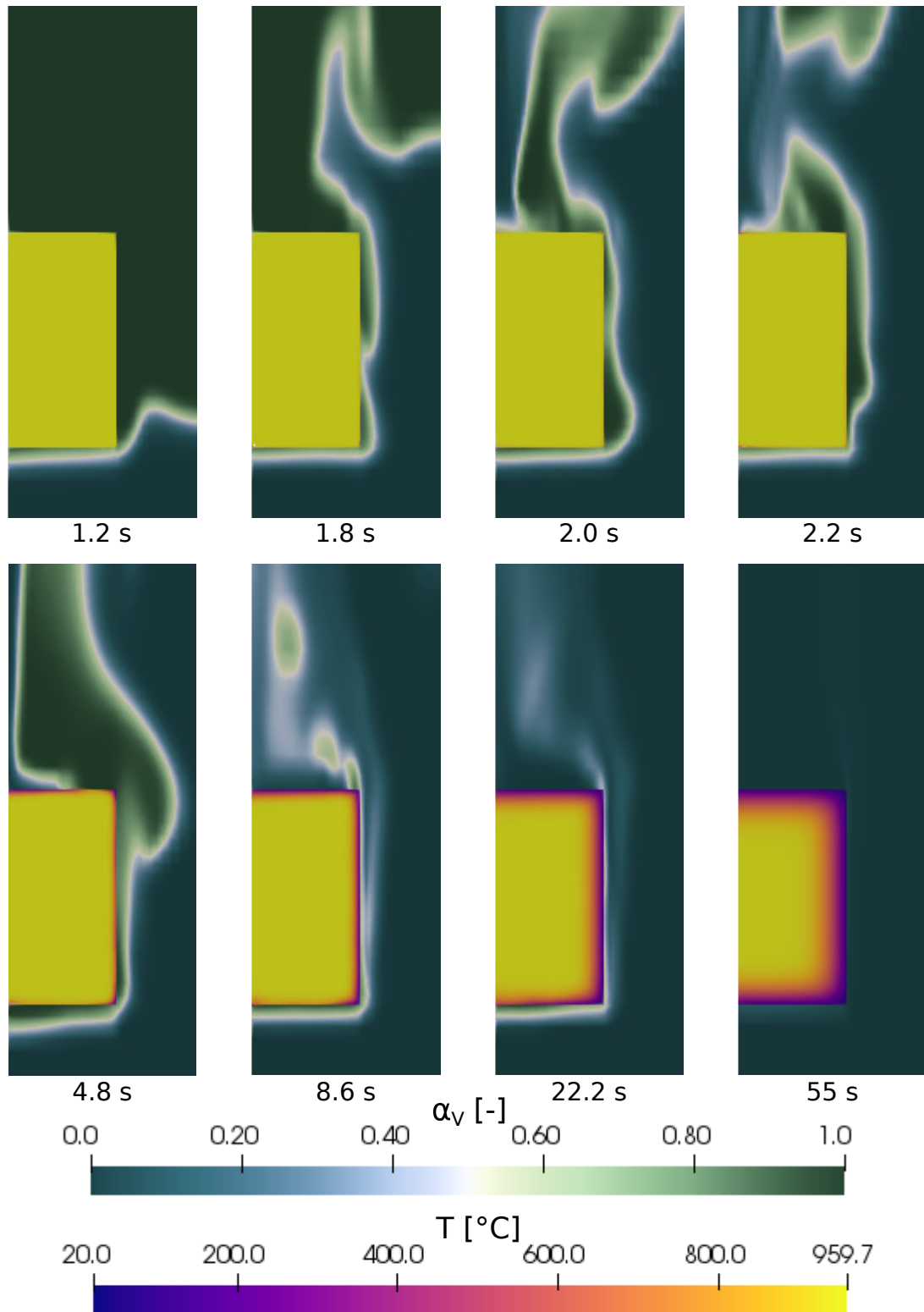


Figure 5.26: Spatial and time distribution of vapour volume fraction and solid temperature acquired using meshes with 59,008 and 451,500 computational elements for fluid and solid, respectively. The figures represent only a segment of the computational domain.

rises alongside the cylinder and creates a vortex above it. Then the rising liquid convects the specimen's heat, leading to a higher heat transfer coefficient resulting from an increased Reynolds number. Therefore, it can effectively be spoken about forced convection. Later, hand in hand with liquid surrounding the cylinder surface, the vapour is restricted in channels and columns with diverging and converging cross-sections resulting in velocity variations. Its magnitude occasionally gets even beyond 5.00 m/s . Due to the development of the vapour columns, the flow patterns change frequently, and a large variety of vortices appear, but most often, a vortex above the cylinder is notable. Finally, the flow calms down because less and less vapour is generated, leading to smaller velocity gradients and the disappearance of vortices.

Theoretically, the surrounding quenching vessel might also affect the cooling process by restricting the bulk fluid from movement bouncing any fluid disturbances back to the specimen. Nonetheless, this does not seem to play a significant role here. The vessel has a sufficient size to avoid these undesirable effects that would not be controllable. The bulk fluid instead serves only as a reservoir of fresh coolant, replenishing the specimen walls by a fluid at a more or less constant temperature.

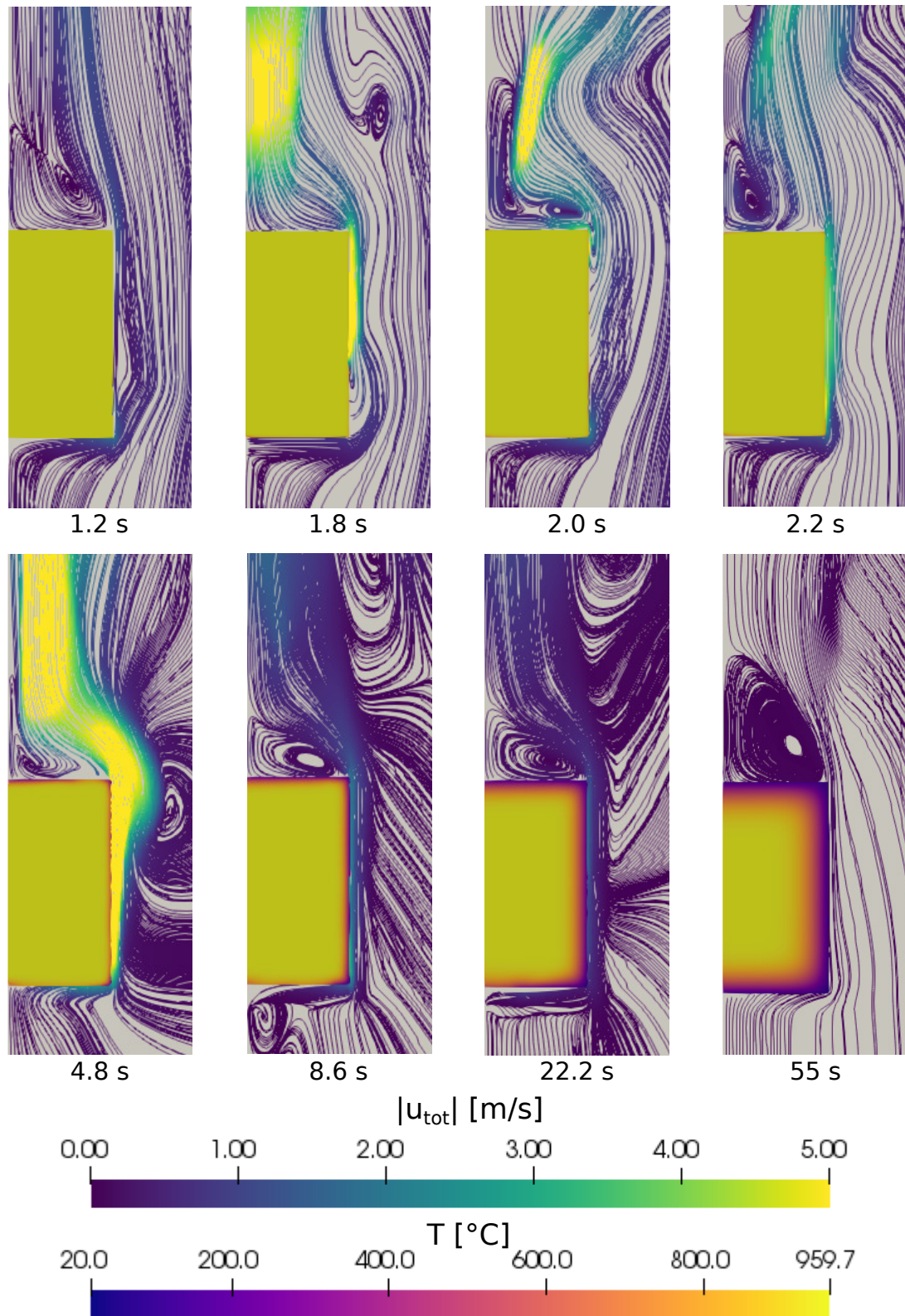


Figure 5.27: Spatial and time distribution of total velocity u_{tot} (Eq. 2.15) streamlines, coloured by its magnitude, and cylinder temperature acquired using meshes with 59,008 and 451,500 computational elements for fluid and solid, respectively. The figures represent only a segment of the computational domain.

Finally, information concerning the code compute time for this type of problem is mentioned. For the configuration, without *IPC* and meshes with 59,008 and 451,500 elements for fluid and solid, ten Intel Xeon Gold 6138 (Skylake) processors @2.0 GHz on a single node with 40 cores were used. One node has access to 192 GB RAM, hence 4.8 GB per core. The elapsed cores time to reach 25 s with maximum $CFL = 0.5$ and maximum time step 0.001 s was 78,894 s. Notice that six regions' coupling, one fluid solution, two fluid energy, two pressure corrector and two solid solution loops were used (Fig. 2.4).

5.5 Summary

This chapter has been devoted to cylinder quenching, the project's most complex problem studied. It has served as another validation case that concluded well because it has shown the methodology potential yet also revealed its drawbacks. Besides the validation, the work consisted of experimental analysis, mesh sensitivity study and physics discussion.

The experimental analysis demonstrated that the thermodynamics complexity heavily depends on the hot surface orientation in relation to the gravitational direction. The solid temperature in the vicinity of the interface may develop a distinct cooling pattern when vapour is present and not allowed to flow freely. Additionally, it has been shown that the testing facility design may greatly affect the cooling. Even seemingly minor geometrical changes can change the thermal gradients. The cylinder holder structure and thermocouple wiring act as an example.

The mesh sensitivity study confirmed mesh independence to solid refinement, yet also difficulty to converge the fluid mesh. The fluid mesh becomes independent of the mesh only at the surfaces, where sufficient mixing appears, hence at the top and vertical cylinder surfaces. The difficulty arises at the bottom, where the vapour movement is restricted, and its volume fraction reaches considerable values approaching its maximum. The mesh independence can be gained if *IPC* is activated. Due to high subcooling, most vapour liquefies and does not obstruct the hot surface. However, blindly exercising such an approach might lead to unphysical results as vapour presence is often desirable. Moreover, *IPC* activation might lead to numerical instability.

Another outcome of the mesh sensitivity study is that the solid must often be more refined than the fluid to accommodate the thermal gradient and ensure stability. If the solid mesh is too coarse, its temperature tends to overreact to fluid dynamics, and instability eventually occurs.

Lastly, the code has been validated against the experiment. A good agreement was reached at the cylinder vertical surface. An eventual improvement could be most likely made by the wall boiling boundary condition setup. Also, at the bottom, the numerical results agreed well with the experiment, yet only at the cylinder axis close to the surface. Closer to the cylinder bottom edge, rather large differences were observed. The last cylinder surface, the top, showed exactly opposite behaviour, relatively satisfying cooling results close to the cylinder edge but large discrepancy at its axis.

Finally, two main items come to mind: wall boiling mass source and bubble dynamics (break-up, crowding, coalescence). The computational methodology utilised within the research has dominantly been used for forced and vertical flows. However, the circumstances are very different in the immersion quenching without agitation. That, in the author's opinion, leads to an even higher importance of bubble dynamics than at the previously mentioned conditions. Appropriate bubble dynamics implementation would result in better prediction of interfacial terms and ideally in improvements at the cylinder bottom surface or even better fluid mesh behaviour. Nevertheless, the wall boiling mass source term directly related to the boundary cell size always seems somewhat an issue and is one of the main points for future work.

Chapter 6

Conclusions

This chapter concludes the study by addressing the research questions and aims, and summarises the work. Besides that, it also emphasises the study contribution to the state of the art, discusses the methodology and research limitations, and provides recommendations for future work.

The research has aimed to deliver a validated computational tool for immersion quenching, neglecting phase transformation within the specimen. The results indicate that the chosen methodology has the capability to predict specimen cooling behaviour under various fluid conditions, solid shapes and temperature differences. Nonetheless, the approach has its limitations, and further development is necessary.

The computational tool was validated using three different problems with increasing complexity. The Backwards-facing step (BFS) belongs among well-researched topics throughout the history of fluid dynamics, yet the investigated variation with conjugate heat transfer is part of the renewed interest. Despite using a two-phase methodology for a one-phase flow problem, the results demonstrated excellent agreement with the available literature.

The second computational problem the methodology was applied to, coped with immersion quenching of a flat plate in horizontal orientation. Indeed, the added complexity compared to the BFS is primarily due to the appearance of boiling and inherently two-phase flow. The acquired data then provided a basis for simple setup tips necessary for future simulations. Moreover, the whole process leading to the final results, including preprocessing, mesh generation, and computation, ended with a

perfect agreement compared to the experiment, and also helped to identify potential bottlenecks that could induce issues in more complex problems.

A cylinder quenching in vertical orientation was the last experiment that served for the code validation and its behaviour investigation. The bar was raised again, this time due to the full range of heat transfer regimes and consideration of the specimen immersion. Previously, the horizontal plate was placed in the coolant, not submerged. In the cylinder related chapter, an experiment analysis was performed, demonstrating cooling behaviour dependence on the hot surface orientation, and discussing the impact of the experimental facility design. The computational results showed variable agreement concerning different locations in the cylinder. They agreed well at the vertical surface while having a mismatch at the bottom. Additionally, the results indicated the problematic nature of the wall boiling boundary condition implementation, initially developed and tested only for nucleate boiling and vertical or at least forced flow. A simple expansion of such a boundary condition to transition and film boiling may lead to fluid mesh sensitivity, especially if stagnant fluid with a hot surface facing downwards is of interest.

6.1 Contributions

The research has contributed to the present level of understanding in theory as well as practice. The first to mention is the peer-reviewed paper [103] and the best student paper award received at an international conference devoted to heat transfer [73] (16th UK Heat Transfer Conference, Nottingham). This success clearly illustrates an excellent research knowledge gap identification, the interest in the field and the need for advancement.

A significant addition is the derivation of numerical Biot number applicable for two-phase flows with or without boiling. Throughout the study, the number was utilised to understand the physics and assess the numerical computations but can also be employed for stability determination.

Further, the performed validation of the complete computational tool as well as various code segments is essential. An example is the regions' interface boundary condition, one of the newly developed features. Previously, two separate mathematical

model solvers for boiling fluid and solid had existed and were used. However, these two individual solvers were made to communicate using the boundary condition only when this research project began. The BFS then served as a validation problem. Although it was initially intended for one fluid phase, the validation was still done using two phases.

Similarly, the original thermal turbulent diffusivity boundary condition had to be altered to enable the solution of film and transition boiling. Its role is crucial as it effectively calculates the conjugated heat and the emerging vapour mass. Again, the validation using the horizontal plate and vertical cylinder showed promising results.

It is also believed that the methodology description and the validation problems offer a potential user an invaluable overview that can increase the awareness of the crucial mathematical models. Moreover, the computational examples act as guidance to simulations. Otherwise, the first usage attempts may be daunting due to the methodology complexity and prerequisite knowledge and skills.

For a detailed list of key developments and improvements, follow Section 1.5.

6.2 Limitations

Despite the best intention and effort, every research is inherently subjected to limitations that may raise questions. Similarly, constructive criticism is an inseparable tool to improving a study. Formulating these, opportunities for future research can be suggested.

The consequences of the two-phase Eulerian approach are the first to mention. Because the fluid phases' interface is not resolved, the interfacial terms including mass, momentum and energy must be modelled. These heavily rely on the chosen phases' interfacial models and the area concentration, hence bubble Sauter mean diameter. Yet, the interfacial models' generality and accuracy may vary and would deserve broader discussion. The chosen models might not be the best available for specific conditions such as subcooling, high vapour volume fraction, and condensation, to name a few. Similarly, although, in reality, the Sauter mean diameter vary significantly depending on flow conditions and heat transfer regimes, it is defined constant at 3 *mm* for the simulations. The alternative would be to use Population Balance [54] or Area Transport

Equation [53]. In the current research, the bubble diameter was used instead as a solution parameter, similarly to literature (Section 1.4.4).

Other limitations emerge from the usage of the wall boiling modelling. Its function is based on many submodels: Leidenfrost temperature, minimum heat flux, the temperature of departure from nucleate boiling, critical heat flux, bubble detachment frequency, detachment diameter, nucleation density site and area fractions. All have alternatives and often lack generality, which is partially overcome by parameters k_{burn} , k_{MHF} and w_p . These parameters help reach the desired result yet require the user to find the proper values.

The following limitation is the mass source calculated within the wall boiling boundary condition and resulting in vapour volume fraction in the boundary cell. It was shown that the vapour volume fraction is mesh sensitive, where the fluid is stagnant, and no condensation is allowed. Although physically vapour volume fraction refinement increase might be assessed as better vapour layer resolution, it is problematic when impacting regions' interface heat transfer.

Further, it must be stated that some improvements might also be made regarding the usage of turbulence modelling. The matter has not been extensively researched within this study. There are alternatives to the mixture $k - \epsilon$ model. Nevertheless, likely phase inversion and equations interfacial interaction must be considered.

Additional limitation appears due to the consideration of constant material properties despite the significant temperature differences within the solid specimens. Only vapour density varies.

Lastly, although the research did not aim to develop new mathematical models for various phenomena, it would benefit from more experimental data. Indeed, solid temperature is easy to measure. Yet, information on the bubble dynamics, specimen immersion velocity and surface temperature, fluid velocities and impact of quenching apparatus (thermocouple wires, specimen holders) would provide valuable insides to understand where the most prominent error comes from and what needs to alter.

6.3 Future Work

The chapter concludes with a discussion of future work opportunities:

- The hot surface orientation affects bubbles dynamics, hence their size, which is a crucial parameter used to estimate interfacial terms in the fluid region. Therefore it is suggested to investigate the impact of Population Balance or Area Transport Equation approaches.
- The regions' interface temperature is a function of the heat transfer coefficient, thus thermal turbulent diffusivity. A usual approach is to iterate between boundary conditions of these two variables, which, however, does not guarantee convergence of vapour volume fraction. An alternative requires computing the phase transport equation, which can be done by looping over the fluid region. It is suggested to compare these two procedures to assess the stability, time requirements and convergence.
- Another opportunity for future research is to investigate the impact of variable material properties in both regions. As much it sounds trivial, the user might need coding experience. Current properties' models are not stable if used for liquid because the regions' interface temperature reaches very high values. Thus values at which liquid should not exist anymore. That leads to unrealistic results and often causes a floating-point exception.
- Although nucleate boiling is the most mechanistic boiling model currently implemented, it is proposed to code some of the more sophisticated models derived using forces acting on the bubbles present at the surface [118–120]. These models typically account for the surface orientation and include extra heat partition due to bubble slide.
- Future work should not avoid one of the main issues arising from wall boiling implementation. Hence the dependency of vapour volume fraction on the fluid mesh refinement, especially where the flow is stagnant.
- Future users would also benefit from a study on the effect of wall boiling parameters k_{burn} , k_{MHF} and w_p or, even better, from their replacement by a more general approach.

- Throughout the research, two different geometries for quenching were used to validate the solver. Nonetheless, additional validation using more complex geometry not allowing block-structured mesh would help to show the software usability for engineering problems. Eventually, the agitation could be employed.
- There is a number of coolants utilised in immersion quenching. To make the software a well-rounded computational tool, it should also be capable of predicting cooling behaviour for those. However, because the wall boiling is very empirical-based, it may not be a straightforward task.
- The film and transition boiling definition use a very simplistic approach. The same applies for the Leidenfrost temperature, minimum heat flux, critical heat flux and departure from nucleate boiling temperature. More sophisticated modelling is desirable because the values can vary extensively due to different reasons, such as surface orientation and hence flow conditions. A revision on this topic followed by implementation of the state of the art approach would be beneficial.

This final chapter has given a concise summary of the research, its contributions and limitations. The work then outlined the existing opportunities which can be taken to advance the field and build on the study.

References

- [1] Homer; and R. Fitzgerald. *The Odyssey*. New York: Vintage Books., 1990.
- [2] D. S. MacKenzie. History of quenching. *International Heat Treatment and Surface Engineering*, 2(2): 68–73, 2008.
- [3] Liscic B., Tensi H., Canale L. and Totten G. *Quenching Theory and Technology*. CRC Press, second edition, 2010.
- [4] F. A. Kulacki, V. K. Dhir, M. P. Mengüç, Y. Chudnovsky, S. Acharya, R. M. Cotta, R. Devireddy, J. Mostaghimi and K. Vafai. *Handbook of Thermal Science and Engineering*. Springer, 2018.
- [5] R. Hernandez, C. P. Folsom, N. E. Woolstenhulme, C. B. Jensen, J. D. Bess, J. P. Gorton and N. R. Brown. Review of pool boiling critical heat flux (CHF) and heater rod design for CHF experiments in TREAT. *Progress in Nuclear Energy*, 123, 2020.
- [6] L. S. Tong. An Evaluation of the Departure from Nucleate Boiling in Bundles of Reactor Fuel Rods. *Nuclear Science and Engineering*, 33(1): 7–15, 1968.
- [7] R. Kamenicky, P. K. Domalapally and X. Arnoult. Thermo-mechanical stress analysis of the water cooled DEMO First Wall mock-up components. *Fusion Engineering and Design*, 136: 1618–1623, 2018.
- [8] P. Domalapally, E. Rizzo, L. Savoldi Richard, F. Subba and R. Zanino. CFD analysis of flow boiling in the ITER first wall. *Fusion Engineering and Design*, volume 87, pages 556–560. 2012.
- [9] M. K. Sung and I. Mudawar. Single-Phase and two-phase hybrid cooling schemes for high-heat-flux thermal management of defense electronics. *Journal of Electronic Packaging, Transactions of the ASME*, 131(2): 0210131–02101310, 2009.

-
- [10] A. Kalani and S. G. Kandlikar. Enhanced pool boiling with ethanol at subatmospheric pressures for electronics cooling. *Journal of Heat Transfer*, 135(11): 1–7, 2013.
- [11] S. Nukiyama. The maximum and minimum values of the heat Q transmitted from metal to boiling water under atmospheric pressure. *International Journal of Heat and Mass Transfer*, 9(12): 1419–1433, 1966.
- [12] F. Krause, S. Schüttenberg and U. Fritsching. Modelling and simulation of flow boiling heat transfer. *International Journal of Numerical Methods for Heat and Fluid Flow*, 20(3): 312–331, 2010.
- [13] C. H. Gür and J. Pan. *Thermal Process Modeling of Steels*. CRC Press, 2009.
- [14] G. E. Totten, C. E. Bates and N. A. Clinton. *Handbook of Quenchants and Quenching Technologies*. ASM International, 1993.
- [15] L. d. C. F. Canale and G. E. Totten. Eliminate Quench Cracking with Uniform agitation. *Heat Treating Progress*, (August): 27–30, 2004.
- [16] P. Fernandes and K. N. Prabhu. Effect of section size and agitation on heat transfer during quenching of AISI 1040 steel. *Journal of Materials Processing Technology*, 183(1): 1–5, 2007.
- [17] M. Sedighi and C. A. McMahon. The influence of quenchant agitation on the heat transfer coefficient and residual stress development in the quenching of steels. *Proceedings of the Institution of Mechanical Engineers, Part B: Journal of Engineering Manufacture*, 214(7): 555–567, 2000.
- [18] H. Jouhara and B. P. Axcell. Film boiling heat transfer and vapour film collapse on spheres, cylinders and plane surfaces. *Nuclear Engineering and Design*, 239(10): 1885–1900, 2009.
- [19] L. de Campos Franceschini Canale and G. E. Totten. Quenching technology: A selected overview of the current state-of-the-art. *Materials Research*, 8(4): 461–467, 2005.
- [20] H. Ramezanzadeh, A. Ramiar and M. Yousefifard. Numerical investigation into coolant liquid velocity effect on forced convection quenching process. *Applied Thermal Engineering*, 122: 253–267, 2017.
- [21] R. T. von Bergen. The Effects of quenchant media selection and control on the distortion of engineered steel parts. *Materials Science Forum*, 163-6(pt 1): 139–150, 1994.

-
- [22] R. Kopun, L. Škerget, M. Hriberšek, D. Zhang, B. Stauder and D. Greif. Numerical simulation of immersion quenching process for cast aluminium part at different pool temperatures. *Applied Thermal Engineering*, 65(1-2): 74–84, 2014.
- [23] H. J. Vergara-Hernández and B. Hernández-Morales. A novel probe design to study wetting front kinematics during forced convective quenching. *Experimental Thermal and Fluid Science*, 33(5): 797–807, 2009.
- [24] D. Greif, Z. Kovacic, V. Srinivasan, D. Wang and M. Suffa. Coupled Numerical Analysis of Quenching Process of Internal Combustion Engine Cylinder Head. *BHM Berg- und Hüttenmännische Monatshefte*, 154(11): 509–517, 2009.
- [25] V. Srinivasan, K. M. Moon, D. Greif, D. M. Wang and M. hwan Kim. Numerical simulation of immersion quenching process of an engine cylinder head. *Applied Mathematical Modelling*, 34(8): 2111–2128, 2010.
- [26] E. S. Jan J, Prabhu E, Lasecki J, Weiss U, Kaynar A. Development and Validation of CFD Methodology to Simulate Water Quenching Process. *ASME conference: International Manufacturing Science and Engineering Conference*. 2014.
- [27] N. A. Hilder. *The Behaviour of Polymer Quenchants*. Ph.D. thesis, 1988.
- [28] G. Ramesh and K. Narayan Prabhu. Effect of Polymer Concentration on Wetting and Cooling Performance During Immersion Quenching. *Metallurgical and Materials Transactions B: Process Metallurgy and Materials Processing Science*, 47(2): 859–881, 2016.
- [29] D. M. Wang, A. Alajbegovic, X. Su and J. Jan. Numerical modeling of quench cooling using Eulerian two-fluid method. *ASME International Mechanical Engineering Congress and Exposition, Proceedings*, 3: 179–185, 2002.
- [30] D. M. Wang, A. Alajbegovic, X. Su and J. Jan. Numerical Simulation of Water Quenching Process of an Engine Cylinder Head. *Proceedings of ASME FEDSM'03 4TH ASME-JSME Joint Fluids Engineering Conference*, 1: 1571–1578, 2003.
- [31] V. Srinivasan, K. M. Moon, D. Greif, D. M. Wang and M. hwan Kim. Numerical simulation of immersion quench cooling process using an Eulerian multi-fluid approach. *Applied Thermal Engineering*, 30(5): 499–509, 2010.
- [32] R. Kopun, L. Škerget, M. Hriberšek, D. Zhang and W. Edelbauer. Numerical investigations of quenching cooling processes for different cast aluminum parts. *Strojniski Vestnik/Journal of Mechanical Engineering*, 60(9): 571–580, 2014.

-
- [33] D. S. Zhang, R. Kopun, N. Kosir and W. Edelbauer. Advances in the numerical investigation of the immersion quenching process. *IOP Conference Series: Materials Science and Engineering*, 164, 2017.
- [34] J. Jan and D. S. Mackenzie. On the characterization of heat transfer rate in various boiling regimes using quenchometers and its application for quenching process simulations. *Thermal Processing in Motion 2018 - Including the International Conference on Heat Treatment and Surface Engineering in Automotive Applications*, pages 112–123. 2018.
- [35] J. Jan and D. S. MacKenzie. On the Development of Parametrical Water Quenching Heat Transfer Model Using Cooling Curves by ASTM D6200 Quenchometer. *Journal of Materials Engineering and Performance*, 29(6): 3612–3625, 2020.
- [36] M. Khalloufi, R. Valette and E. Hachem. Adaptive Eulerian framework for boiling and evaporation. *Journal of Computational Physics*, (October), 2019.
- [37] T. Verstraete and S. Scholl. Stability analysis of partitioned methods for predicting conjugate heat transfer. *International Journal of Heat and Mass Transfer*, 101: 852–869, 2016.
- [38] J. Peltola and T. J. H. Pättikangas. Development and validation of a boiling model for OpenFOAM multiphase solver. CFD4NRS-4 Conference Proceedings. 2012.
- [39] C. L. V. Jayatilleke. *The Influence of Prandtl Number and Surface Roughness on the Resistance of the Laminar Sub-Layer to Momentum and Heat Transfer*. Ph.D. thesis, Imperial College of Science and Technology, 1966.
- [40] N. Kurul and M. Podowski. *Multidimensional Effects in Forced Convection Subcooled Boiling*. 1990.
- [41] L. A. Bromley. *Heat Transfer in Stable Film Boiling*. Technical report, University of California, 1949.
- [42] S. Scholl, B. Janssens and T. Verstraete. Stability of static conjugate heat transfer coupling approaches using Robin interface conditions. *Computers and Fluids*, 172: 209–225, 2018.
- [43] M. B. Giles. Stability analysis of numerical interface conditions in fluid-structure thermal analysis. *International Journal for Numerical Methods in Fluids*, 25(4): 421–436, 1997.
- [44] D. A. Drew and S. L. Passman. *Theory of Multicomponent Fluids*. Springer-Verlag New York, 1999.

-
- [45] C. T. C. Efstathios E. Michaelides and D. S. John. *Multiphase flow handbook*. CRC Press, 2017.
- [46] A. Behzadi, R. I. Issa and H. Rusche. Modelling of dispersed bubble and droplet flow at high phase fractions. *Chemical Engineering Science*, 59(4): 759–770, 2004.
- [47] R. T. Lahey. The simulation of multidimensional multiphase flows. *Nuclear Engineering and Design*, 235(10-12): 1043–1060, 2005.
- [48] B. E. Launder and D. B. Spalding. The numerical computation of turbulent flows. *Computer Methods in Applied Mechanics and Engineering*, 3(2): 269–289, 1974.
- [49] H. G. Weller. Derivation, modelling and solution of the conditionally averaged two-phase flow equations. Technical report, OpenCFD Limited, 2002.
- [50] H. Rusche. *Computational Fluid Dynamics of Dispersed Two-Phase Flows at High Phase Fractions*. Ph.D. thesis, Imperial College of Science, Technology and Medicine, 2002.
- [51] C. M. Rhie and W. L. Chow. Numerical study of the turbulent flow past an airfoil with trailing edge separation. *AIAA Journal*, 21(11): 1525–1532, 1983.
- [52] G. Y. J.Y. Tu. On numerical modelling of low-pressure subcooled boiling flow. 45: 1197–1209, 2002.
- [53] I. Mamoru, K. Seungjin and K. Joseph. Development of Interfacial Area Transport Equation, 2005.
- [54] G. H. Yeoh. *Computational techniques for multi-phase flows : basics and applications*. Butterworth-Heinemann, Oxford, 1st ed.. edition, 2010.
- [55] M. Ishii and N. Zuber. Drag coefficient and relative velocity in bubbly, droplet or particulate flows. *AIChE Journal*, 25(5): 843–855, 1979.
- [56] A. Tomiyama, H. Tamai, I. Zun and S. Hosokawa. Transverse migration of single bubbles in simple shear flows. *Chemical Engineering Science*, 57(11): 1849–1858, 2002.
- [57] S. P. Antal, R. T. Lahey and J. E. Flaherty. Analysis of phase distribution in fully developed laminar bubbly two-phase flow. *International Journal of Multiphase Flow*, 17(5): 635–652, 1991.
- [58] A. D. Burns, T. Frank, I. Hamill and J. M. Shi. The Favre averaged drag model for turbulent dispersion in Eulerian multi-phase flows. *5th International Conference on Multiphase Flow*, 392, pages 1–17. 2004.

-
- [59] M. Otromke. *Implementation and Comparison of Correlations for interfacial Forces in a Gas-Liquid System within an Euler-Euler Framework*. Ph.D. thesis, 2013.
- [60] W. E. Ranz and W. R. Marshall. Evaporation from Drops, Parts I and II. *Chem Eng Prog.*, 48: 141–146, 1952.
- [61] H. G. Weller, G. Tabor, H. Jasak and C. Fureby. A tensorial approach to computational continuum mechanics using object-oriented techniques. *Computers in Physics*, 12(6): 620, 1998.
- [62] B. Koncar, E. Krepper and Y. Egorov. Cfd Modeling of Subcooled Flow Boiling for Nuclear Engineering Applications. *International conference Nuclear Energy for New Europe*, pages 1–14. 2005.
- [63] J. Bredberg. On the Wall Boundary Condition for Turbulence Models. Technical report, Bredberg2000, 2000.
- [64] D. Schroeder-Richter and G. Bartsch. Analytical calculation of DNB-superheating by a postulated thermo-mechanical effect of nucleate boiling. *Int. J. Multiphase Flow*, 20(6): 1143–1167, 1994.
- [65] N. Zuber and M. Tribus. Further Remarks on the Stability of Boiling Heat Transfer. *United States Atomic Energy Commission*, Report 58-, 1958.
- [66] T. C. Hua and J. J. Xu. Quenching boiling in subcooled liquid nitrogen for solidification of aqueous materials. *Materials Science and Engineering: A*, 292(2): 169–172, 2000.
- [67] V. I. Tolubinsky and D. M. Kostanchuk. Vapour Bubbles Growth Rate and Heat Transfer Intensity at Subcooled Water Boiling. 1970.
- [68] M. Lemmert and J. M. Chawla. Influence of flow velocity on surface boiling heat transfer coefficient. *Heat Transfer in Boiling*, pages 237–247, 1977.
- [69] Y. Egorov and F. Menter. Experimental implementation of the RPI wall boiling model in CFX-5.6. Technical report, ANSYS Gmbh, 2004.
- [70] R. W. Bowring. Physical Model, Based on Bubble Detachment, and Calculation of Steam Yoidage in the Sub cooled Region of a Heated Channel. Technical report, Institut for Atomenergi, 1962.
- [71] R. Cole. Photographic Study of Pool Boiling in the Region of the Critical Heat Flux. *A.I.Ch.E. Journal*, 6(4): 533–538, 1960.

-
- [72] B. van Leer. Towards the ultimate conservative difference scheme. II. Monotonicity and conservation combined in a second-order scheme. *Journal of Computational Physics*, 14(4): 361–370, 1974.
- [73] R. Kamenicky, M. Frank, D. Drikakis and K. Ritos. A Study of Nucleate Boiling Conjugate Heat Transfer. C. Wen and Y. Yan (editors), *Advances in Heat Transfer and Thermal Engineering*, pages 203–206. Springer Singapore, Singapore, 2021.
- [74] D. K. Gartling. A test Problem for Outflow Boundary Conditions-flow over a Backward-facing Step. *International Journal for Numerical Methods in Fluids*, 11: 953–967, 1990.
- [75] P. M. Gresho, D. K. Gartling, J. R. Torczynski, K. A. Cliffe, K. H. Winters, T. J. Garratt, A. Spence and J. W. Goodrich. Is the steady viscous incompressible two-dimensional flow over a backward-facing step at $Re = 800$ stable? *International Journal for Numerical Methods in Fluids*, 17(6): 501–541, 1993.
- [76] M. M. Grigoriev and G. F. Dargush. A poly-region boundary element method for incompressible viscous fluid flows. *International Journal for Numerical Methods in Engineering*, 46(7): 1127–1158, 1999.
- [77] M. Ramšak. Conjugate heat transfer of backward-facing step flow: A benchmark problem revisited. *International Journal of Heat and Mass Transfer*, 84: 791–799, 2015.
- [78] L. Chen, K. Asai, T. Nonomura, G. Xi and T. Liu. A review of Backward-Facing Step (BFS) flow mechanisms, heat transfer and control. *Thermal Science and Engineering Progress*, 6: 194–216, 2018.
- [79] E. O. Macagno and T. K. Hung. Computational and experimental study of a captive annular eddy. *Journal of Fluid Mechanics*, 28(1): 43–64, 1967.
- [80] B. F. Armaly, F. Durst, J. C. F. Pereira and B. Schönung. Experimental and theoretical investigation of backward-facing step flow. *Journal of Fluid Mechanics*, 127: 473–496, 1983.
- [81] E. W. Adams and J. P. Johnston. Effects of the separating shear layer on the reattachment flow structure part 2: Reattachment length and wall shear stress. *Experiments in Fluids*, 6: 493–499, 1988.
- [82] S. Jovic and D. Driver. Reynolds number effect on the skin friction in separated flows behind a backward-facing step. *Experiments in Fluids*, 18(6): 464–467, 1995.

-
- [83] E. Erturk. Numerical solutions of 2-D steady incompressible flow over a backward-facing step, Part I: High Reynolds number solutions. *Computers and Fluids*, 37(6): 633–655, 2008.
- [84] K. F. Yu and E. W. Lee. Evaluation and modification of gas-particle covariance models by Large Eddy Simulation of a particle-laden turbulent flows over a backward-facing step. *International Journal of Heat and Mass Transfer*, 52(23-24): 5652–5656, 2009.
- [85] J. Tihon, V. Pěnkavová, J. Havlica and M. Šimčík. The transitional backward-facing step flow in a water channel with variable expansion geometry. *Experimental Thermal and Fluid Science*, 40: 112–125, 2012.
- [86] K. Sarker, M. Ali and Q. Islam. A numerical study on the physics of flow over a flat plate with backward facing step. *Procedia Engineering*, 90: 351–357, 2014.
- [87] A. Liakos and N. A. Malamataris. Topological study of steady state, three dimensional flow over a backward facing step. *Computers and Fluids*, 118: 1–18, 2015.
- [88] T. D. Nguyen and H. Souad. PIV measurements in a turbulent wall jet over a backward-facing step in a three-dimensional, non-confined channel. *Flow Measurement and Instrumentation*, 42: 26–39, 2015.
- [89] H. H. Choi, V. T. Nguyen and J. Nguyen. Numerical Investigation of Backward Facing Step Flow over Various Step Angles. *Procedia Engineering*, 154: 420–425, 2016.
- [90] Z. Y. Guo, D. Y. Li and X. G. Liang. Thermal effect on the recirculation zone in sudden-expansion gas flows. *International Journal of Heat and Mass Transfer*, 39(13): 2619–2624, 1996.
- [91] P. Rajesh Kanna and Manab Kumar Das. Conjugate heat transfer study of backward-facing step flow - A benchmark problem. *International Journal of Heat and Mass Transfer*, 49(21): 3929–3941, 2006.
- [92] K. Khanafer, B. Al-Azmi, A. Al-Shammari and I. Pop. Mixed convection analysis of laminar pulsating flow and heat transfer over a backward-facing step. *International Journal of Heat and Mass Transfer*, 51(25-26): 5785–5793, 2008.
- [93] H. Barrios-Pina, S. Viazzo and C. Rey. A numerical study of laminar and transitional mixed convection flow over a backward-facing step. *Computers and Fluids*, 56: 77–91, 2012.

-
- [94] F. E. Teruel and E. Fogliatto. Numerical Simulations of Flow, Heat Transfer, and Conjugate Heat Transfer in the Backward-Facing Step Geometry. *Mecánica Computacional*, XXXII: 3265–3278, 2013.
- [95] M. Seddiq, M. Maerefat and M. Mirzaei. Modeling of heat transfer at the fluid-solid interface by lattice Boltzmann method. *International Journal of Thermal Sciences*, 75: 28–35, 2014.
- [96] J. H. Xu, S. Zou, K. Inaoka and G. N. Xi. Influence du nombre de Reynolds sur l'écoulement et le transfert de chaleur dans la convection forcée incompressible en marche arrière 3D. *International Journal of Refrigeration*, 79: 164–175, 2017.
- [97] M. Frank, R. Kamenicky, D. Drikakis, L. Thomas, H. Ledin and T. Wood. Multiphase Flow Effects in a Horizontal Oil and Gas Separator. *Energies*, 12(11), 2019.
- [98] M. Ramšak, L. Škerget, M. Hriberšek and Z. Žunič. A multidomain boundary element method for unsteady laminar flow using stream function-vorticity equations. *Engineering Analysis with Boundary Elements*, 29(1): 1–14, 2005.
- [99] M. Ramšak and L. Škerget. A highly efficient multidomain BEM for multimillion subdomains. *Engineering Analysis with Boundary Elements*, 43: 76–85, 2014.
- [100] F. P. Incropera, D. P. Dewitt, T. L. Bergman and A. S. Lavine. *Fundamentals of Heat and Mass Transfer*. John Wiley & Sons, [303], 6th ed. edition, 2007.
- [101] D. K. Gartling. NACHOS II: A finite element computer program for incompressible flow problems: Part 2, User's manual. 1987.
- [102] F. D. International. *FIDAP Theoretical Manual*. Fluid Dynamics International, Evanston, version 4. edition, 1988.
- [103] R. Kamenicky, M. Frank, D. Drikakis and K. Ritos. Film boiling conjugate heat transfer during immersion quenching. *Energies*, 15(12), 2022.
- [104] P. E. Farrell and J. R. Maddison. Conservative interpolation between volume meshes by local Galerkin projection. *Computer Methods in Applied Mechanics and Engineering*, 200(1-4): 89–100, 2011.
- [105] G. k. Schlichting H. *Boundary-Layer Theory*. Springer, Berlin, Heidelberg, 9th ed. edition, 2017.

-
- [106] J. V. Beck. Nonlinear estimation applied to the nonlinear inverse heat conduction problem. *International Journal of Heat and Mass Transfer*, 13(4): 703–716, 1970.
- [107] S. Lu, Y. Heng and A. Mhamdi. A robust and fast algorithm for three-dimensional transient inverse heat conduction problems. *International Journal of Heat and Mass Transfer*, 55(25): 7865–7872, 2012.
- [108] G. Ramesh and K. Narayan Prabhu. Assessment of axial and radial heat transfer during immersion quenching of Inconel 600 probe. *Experimental Thermal and Fluid Science*, 54: 158–170, 2014.
- [109] T. H. Lee, G. C. Park and D. J. Lee. Local flow characteristics of subcooled boiling flow of water in a vertical concentric annulus. *International Journal of Multiphase Flow*, 28(8): 1351–1368, 2002.
- [110] C. Lifante, F. Reiterer, T. Frank and A. Burns. Coupling of wall boiling with discrete population balance model. *Journal of Computational Multiphase Flows*, 4(3): 287–298, 2012.
- [111] E. Krepper, R. Rzehak, C. Lifante and T. Frank. CFD for subcooled flow boiling: Coupling wall boiling and population balance models. *Nuclear Engineering and Design*, 255: 330–346, 2013.
- [112] S. M. Wang, J. Wen, Y. M. Li, S. H. Wang and Y. Z. Li. Population balance modelling for subcooled boiling flow of liquid nitrogen in a vertical tube. *International Journal of Heat and Mass Transfer*, 60: 632–645, 2013.
- [113] S. C. Cheung, S. Vahaji, G. H. Yeoh and J. Y. Tu. Modeling subcooled flow boiling in vertical channels at low pressures - Part 1: Assessment of empirical correlations. *International Journal of Heat and Mass Transfer*, 75: 736–753, 2014.
- [114] R. Zhang, T. Cong, W. Tian, S. Qiu and G. Su. CFD analysis on subcooled boiling phenomena in PWR coolant channel. *Progress in Nuclear Energy*, 81: 254–263, 2015.
- [115] M. Colombo and M. Fairweather. Accuracy of Eulerian–Eulerian, two-fluid CFD boiling models of subcooled boiling flows. *International Journal of Heat and Mass Transfer*, 103: 28–44, 2016.
- [116] H. Setoodeh, W. Ding, D. Lucas and U. Hampel. Modelling and simulation of flow boiling with an Eulerian-Eulerian approach and integrated models for bubble dynamics

- and temperature-dependent heat partitioning. *International Journal of Thermal Sciences*, 161: 106709, 2021.
- [117] G. Hu, Y. Ma and Q. Liu. Evaluation on Coupling of Wall Boiling and Population Balance Models for Vertical Gas-Liquid Subcooled Boiling Flow of First. *Energies*, 14(21), 2021.
- [118] R. Sugrue and J. Buongiorno. A modified force-balance model for prediction of bubble departure diameter in subcooled flow boiling. *Nuclear Engineering and Design*, 305: 717–722, 2016.
- [119] L. Gilman and E. Baglietto. A self-consistent, physics-based boiling heat transfer modeling framework for use in computational fluid dynamics. *International Journal of Multiphase Flow*, 95: 35–53, 2017.
- [120] E. Baglietto, E. Demarly, R. Kommajosyula, N. Lubchenko, B. Magolan and R. Sugrue. A Second Generation Multiphase-CFD Framework Toward Predictive Modeling of DNB. *Nuclear Technology*, 205(1-2): 1–22, 2019.

Appendix A

Video of cylinder quenching experiment

Advanced Forming Research Centre provided video footage of an experiment during which the cylinder is quenched in the vertical orientation. This video is available at <https://github.com/ZazaCro/phdAppendices/tree/main/video>. For more information, you can contact Dr Salaheddin Rahimi (salah.rahimi@strath.ac.uk) and Dr Ioannis Violatos (ioannis.violatos@strath.ac.uk).

Appendix B

Computational code and cases

On the following address <https://github.com/ZazaCro/phdAppendices>, the reader can find the computational code used throughout the research. Notice that the code adjustments were often made for private use, so they might not be well-annotated. Also, the coding time was a priority, so the changes might not reflect the best coding practice and efficiency. The link also provides simulations examples from Chapter 3, Chapter 4 and Chapter 5.